Final Report for Project:

Emissivity of Candidate Materials for VHTR Applications: Role of Oxidation and Surface Modification Treatments

U.S. DoE-NERI Grant No.: DE-FC07-07ID14820

Project Investigators: Dr. Kumar Sridharan, Dr. Todd Allen, Dr. Mark Anderson, Dr. Guoping Cao, and Dr. Gerald Kulcinski

University of Wisconsin, Madison

Project Contact: Kumar Sridharan (kumar@engr.wisc.edu)

Date: July 25th, 2011

This page intentionally left blank

Executive Summary

The cooling of the reactor pressure vessel (RPV) and internal components of the VHTR will occur partially by the thermal radiation of heat from their outer surface. Furthermore, in the event of an unexpected increase in temperature, thermal radiation becomes a significant mode of heat dissipation because of its fourth power temperature dependence according to the well-known Stefan-Boltzmann equation, $E= k.T^4$, where E is the emissive power, k is a constant and T is the temperature. The key material parameter that dictates the extent of heat radiated from the surface is emissivity, which is defined as the ratio of emissive power (power radiated per unit area) of the materials' surface to that of an ideal black body. Owing to the greater reliance of radiation heat transfer at the higher operating temperatures of VHTR and during off-normal scenarios, a knowledge of emissivities of specific code-certified candidate materials for potential use in future nuclear reactors is necessary. Since oxidation of materials will inevitably occur at these higher temperatures, it is clear that the knowledge of emissivity of materials is intricately related to the chemical, physical, and mechanical characteristics of the oxide layers that form on their surface. This includes the chemical composition of the oxide layer, its grain morphology, topography, and porosity. The growing field of surface modification technologies provides opportunities for controlling emissivity at high temperatures. These surface treatments could be used to induce modifications of the materials' surface such as changing its topography and chemical composition as well as for changing the nature of the oxide layers that form at high temperatures.

As a part of this project a state-of-the-art high temperature spectral emissvity measurement system was designed and constructed. The system is capable of *in sit*u high temperature spectral emissivity measurements of up to seven material samples in a single experiment and nearly instantaneous data collection, calculation and display of spectral emissivity. The system consists of four essential components, namely a silicon-carbide sample test chamber, multiple mirror optical system, a water-cooled system for holding the optical system, and a Fourier Transform Infrared (FTIR) spectrometer. The system was calibrated with inert ceramic materials, boron-nitride, alumina, and silicon-carbide by bench-marking the measured spectral emissivity values against values from reliable literature. DoE quality assurance protocols were adhered to for these calibrations, and indeed for all the measurements presented in this report.

Spectral emissivity measurements were performed at several high temperatures, but the focus was on testing at sample temperatures of 350^{o}C, 500^{o}C, and 700^{o}C. Several alloys of relevance to VHTR (and nuclear reactor systems in general) were tested, including SA508, T22, and T91 ferrtic steels, Incoloy 800H and Haynes 230 austenitic alloys, and 304 and 316 stainless steels. Limited measurements were also performed for nuclear grade graphite because of the relevance of this material for reflector and moderator components of the VHTR. Samples were evaluated with scanning electron microscopy (SEM), energy dispersive spectroscopy (EDS) and profilometry. The thickness of the oxide layer that formed on the materials' surface had a profound effect on spectral emissivity. The effect of materials' surface roughness was also investigated. Surface roughness had a small but noticeable effect on spectral emissivity with increasing surface roughness resulting in slightly higher spectral emissivity levels.

Since emissivity is a near-surface phenomenon, the effect of several types of surface treatments on spectral emissivity of candidate alloys was investigated. These surface treatments included chromium and hafnium thin film sputter deposition, CVD silicon-carbide coating, and shot peening. Additionally, two novel surface treatments were studied using the plasma

immersion ion implantation and deposition (PIIID) process. These included xenon ion bombardment to change the surface topography and composition of materials on a nanometers scale and deposition of diamond-like carbon films. In all cases there was an observable change in the materials spectral emissivity due to inherent changes in materials surface chemistry, topographical changes, and the modification of the growing thermal oxide layers. These studies have enhanced our fundamental understanding the role materials surface science on emissivity, while pointing to useful future directions where surface treatments could be effectively used to control emissivity in nuclear and other engineering systems. Because emissivity is related closely to development of the surface oxide layer, these surface treatment experiments have also provided useful insights on mitigating oxidation of alloys in high temperature reactor environments.

Although not a primary focus of this project, a numerical modeling effort was initiated to gain predictive capabilities of high temperature spectral emissivity. The numerical modeling efforts used Monte Carlo sampling of emission angle and position for a material sample and a blackbody to determine spectral sample emissivity from the optics constant and extinction coefficient of the material and oxide layers. Of particular interest was the cut-off at which further oxide thickness did not affect emissivity. Preliminary results have bench-marked these modeling predictions of spectral emissivity against experimentally measured results assuming bi-layered chromium- and iron- oxide films grow thermally on alloy steel substrates. The research has laid the foundation that provides a clear pathway for future researchers and end-users interested in numerical modeling of emissivity.

The findings of this research have been disseminated quite extensively in the nuclear engineering community in forums such as *American Nuclear Society Conference*, two *High Temperature Reactor Conferences*, *DoE-NERI Panel Review* meetings, *UW-INL Site Visit meeting*, and the *Materials Science and Technology* conference and published in the proceedings of some of these conferences. Portions of this work have been published in the journal *Nuclear Technology*, and as an invited paper in the journals *Nuclear Engineering and Design*, and the *Journal of Nuclear Materials*. We foresee the publication of at least two more articles in relevant journals in the coming year.

The project has provided a rich scientific environment for training and educating students. Over the three-year term of the project seven undergraduate students from the University of Wisconsin, Madison were actively involved in various phases of this project, including design and construction of the high temperature spectral emissivity system, materials characterization, and data acquisition and analysis. Five of these students were Nuclear Engineering majors, and one student each majoring in Materials Science and Engineering Mechanics. Two students received their Masters degrees in Nuclear Engineering with this project as their thesis research topic. Additionally, a high school student selected by the Madison School District's science program worked on this project over a summer for one university credit. A post-doctoral research associate was also involved in this project.

We thank the U.S. Department of Energy – NERI program for providing the funding for this project.

This page intentionally left blank

Table of Contents

List of Figures

List of Tables

1. Technical Background

1.1 Very High Temperature Reactor

1.1.1. Introduction

The Generation IV (GEN IV) Nuclear Energy Systems Initiative was instituted by the Department of Energy (DOE) with the goal of researching and developing technologies and materials necessary for various types of future reactors. These GEN IV reactors will employ advanced fuel cycles, passive safety systems, and other innovative systems, leading to significant differences between these future reactors and current water-cooled reactors. The leading candidate for the Next Generation Nuclear Plant (NGNP) to be built at Idaho National Lab (INL) in the United States is the Very High Temperature Reactor (VHTR).

Due to the high operating temperatures of the VHTR, the Reactor Pressure Vessel (RPV) will partially rely on heat transfer by radiation for cooling. Heat expulsion by radiation will become all the more important during high temperature excursions during off-normal accident scenarios. Radiant power is dictated by emissivity, a material property. The NGNP Materials Research and Development Program Plan [1] has identified emissivity and the effects of high temperature oxide formation on emissivity as an area of research towards the development of the VHTR.

1.1.2. VHTR Design

The VHTR is a helium-cooled, graphite moderated reactor. Helium is inert however corrosion of VHTR materials is expected to occur over the long term due to trace impurities present in commercial grade helium. The VHTR design is different from current commercial light water reactors (LWR), which use water as a coolant and moderator. Various NGNP designs have been proposed that range from 200 MWt to 600 MWt reactors [2]. This is smaller than a normal LWR, but the improved safety in the VHTR's design and lack of need for a large water supply makes it amenable to be located near urban areas, replacing existing fossil fuel plants. The VHTR also has a much higher operating temperature than a LWR (750^{o}C-800^{o}C). This means in addition to producing electricity the VHTR can provide cogeneration of process heat to near-reactor facilities for chemical, hydrogen production, and desalination plants.

1.1.3 Core Design and Fuel

There are two basic core configurations being considered for the NGNP: the pebble bed and the prismatic designs (Figures 1 and 2, respectively). Three nuclear reactor vendors have submitted designs to INL for the final design of the NGNP (Areva, General Atomics, and Westinghouse in conjunction with South African PBMR Ltd.) with the first two utilizing the prismatic core, and the Westinghouse/PBMR team favoring the pebble bed core [3-5].

Both designs start with the same basic fuel form: the TRISO (tri-isotropic) particle, consisting of uranium kernels with a multi-layered coating. The multi-layered coating consists of an inner pyrolytic carbon layer, an intermediate silicon carbide layer, and an outer pyrolytic carbon layer. This multi-layered coating system is expected to keep all fission products contained in the particle.

In the pebble bed design, the TRISO particles are embedded in a spherical graphite matrix with an outer graphite shell for extra protection and neutron reflectance. These pebbles are circulated slowly through a central annulus or cylinder in the core region. Each pebble can be re-circulated as many as ten times during the fuel's three year lifetime. The helium coolant flows

through the core, and the core is surrounded on either side by more graphite which acts as a reflector. In the prismatic design, the TRISO particles are packed into cylindrical compacts, which are then inserted into larger hexagonal graphite blocks. The blocks have extra cylindrical channels machined through them to allow for coolant flow. The fueled blocks are again surrounded by pure graphite blocks to reflect and shape the neutron flux. The fuel configurations for each core design are summarized in Figure 3.

The TRISO particle design recently set a new world record for uranium burn-up (~19%) [2]. About 300,000 particles were exposed in INL's Advanced Test Reactor (ATR) to a high neutron flux and temperatures of about 1250^{o}C. Not only was a new burn-up record set, but none of the particles experienced failure during testing.

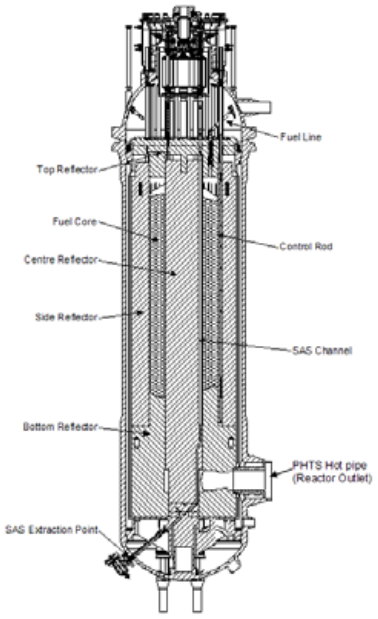

(a)

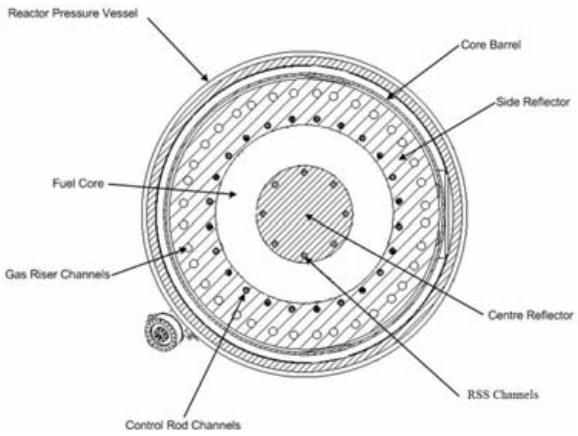

(b)

Figure 1. Westinghouse design for pebble bed core VHTR (a) vertical section and (b) cross-section [3].

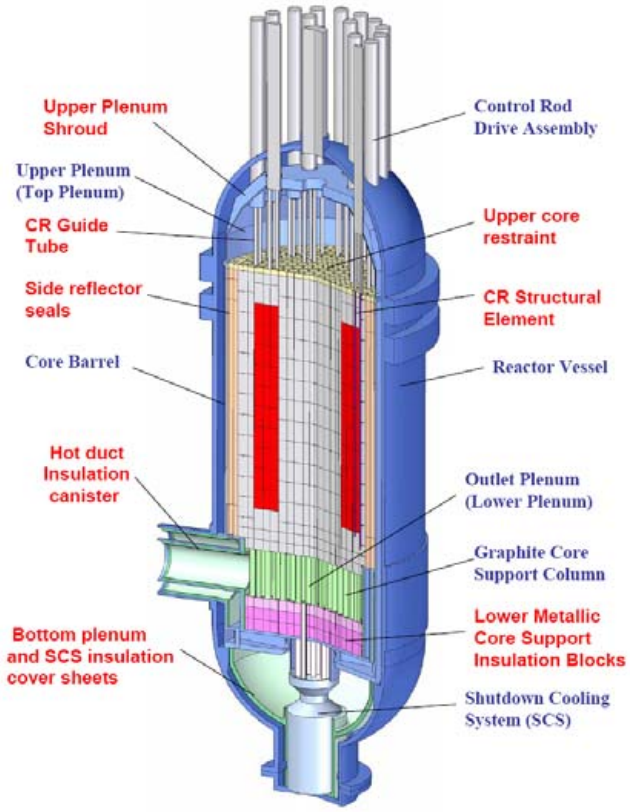

(a)

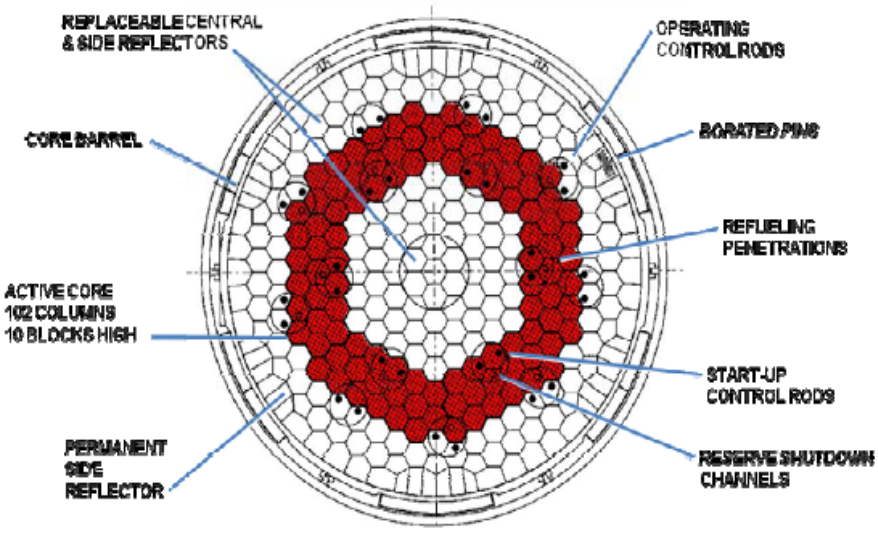

(b)

Figure 2. General Atomic design for prismatic core VHTR (a) vertical section and (b) cross- section [4].

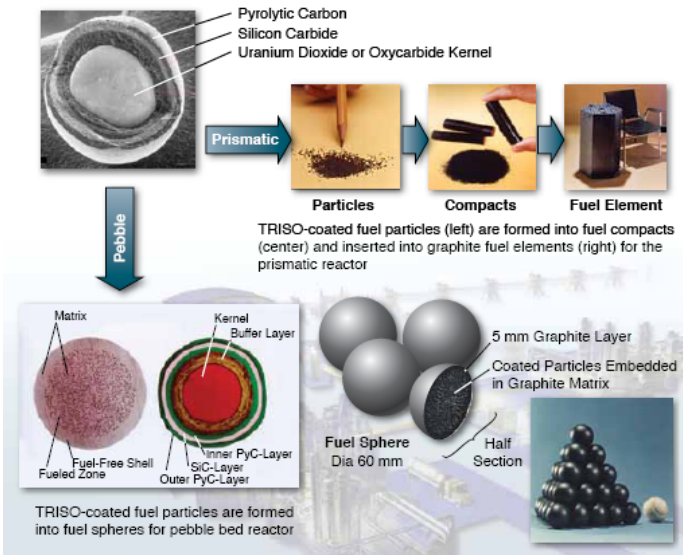

Figure 3. TRISO particles formed into fuel elements for prismatic core (top) and pebble bed (bottom) designs.

1.1.3 Reactor Temperature Profiles and Material Selection

The high outlet helium temperature in the NGNP designs raises a number of material issues not present in lower temperature LWR. Past experience with helium cooled test reactors show that for an outlet temperature of 950°C the inlet temperature of helium into the core must be in the 490°C -590°C range [4]. This means that all internal core components, including the core barrel, will be at or above this inlet temperature. Ceramics are often the materials of choice at high temperatures, due to their high melting point and chemical inertness, and indeed the NGNP designs incorporate many ceramic components. However, ceramics are much more expensive than steels and irradiation effects on material properties have not been investigated as thoroughly in ceramics as in metallic materials. So wherever temperature limits allow, metallic materials will be the material of choice. The most commonly considered alloy for internal reactor components is Incoloy 800H, which is code-certified up to 760°C.

It is important when deciding whether to use ceramic or alloy to not only consider the normal operating temperature of the components, but also how the temperature will change in an accident scenario. Figure 4 shows how the temperature of two reactor components, the shutdown cooling system (SCS) heat exchanger in the bottom plenum area and the upper core restraint (UCR), react to a pressurized conduction cool down (CCD) event (VHTR terminology of a loss of coolant accident) with an inlet helium temperature of 590°C [4]. The normal operating temperatures for both components fall within the operation limit for Incoloy 800H. During the pressurized CCD the SCS starts cooling immediately in an exponential fashion but the temperature of the UCR rises above the 760°C limit for Incoloy 800H before it begins to cool. This means Incoloy 800H could be used for SCS components but the UCR must be made of ceramics.

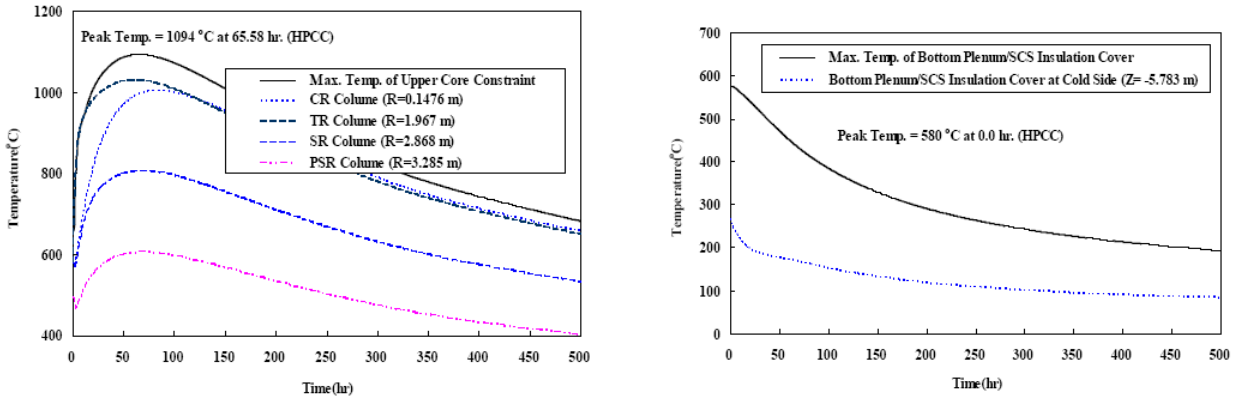

(a) **(b)**

Figure 4. 500 hour transient temperature responses to a pressurized CCD for the (a) UCR and (b) SCS [4].

There are other alloys besides Incoloy 800H being considered for the NGNP reactor. Inconel 617 and Haynes 230 are advanced alloys with higher operating temperature limits than 800H (both alloys code certified to 982°C). The concern with using Inconel 617 or Haynes 230 is that both contain cobalt, which can become thermally activated post-irradiation [6]. Both alloys are also suspected to have poor post-irradiation mechanical properties. They could still be used in reactor locations with low neutron fluence or could also be coated with a layer of boronated graphite to reduce the thermal fluence. A number of studies have investigated the corrosion of these alloys in air and impure helium [7-10], but very few relate corrosion to spectral emissivity. SA 508 is the primary steel being considered for the RPV, mostly because its history of use in RPV's for LWR. Furthermore, both the normal and accident temperature on the RPV inner wall is well within the operating limits of SA 508 at steady state (391°C) due to a secondary cooling system. The elemental compositions of these four alloys are shown in Table 1.

Table 1. Nominal elemental compositions (wt.%) some of the alloys being considered for use in the NGNP VHTR [11].

Alloy	Fe	Ni	Cr	C	Si	Mn	Mo	Al	Ti	Co	W
800H	Bulk	30	19	.05	-	-	-	.15	.15	-	-
SA 508	Bulk	.82	.17	.19	.08	1.35	.51	-	-	-	-
IN 617	-	Bulk	22	-	-	-	10	-	-	13	-
H 230	2	57	22	.1	.4	-	2	.3	-	.3	14

1.2 EMISSIVITY MEASUREMENTS

1.2.1 Basic Theory

There are three main modes of heat transfer in materials: conduction, convection, and radiation [12]. While conduction and convection vary linearly with temperature, radiation varies with the fourth power of temperature according to the Stefan-Boltzmann equation (1), making it

a dominant mode of heat transfer at high temperatures [13], such as those that would be experienced in the VHTR. This is especially true for metallic reactor components such as the core barrel and RPV since there is no means of conduction and only limited convection.

$$E = \varepsilon \sigma T^4 \quad (1)$$

where,

E = Emissive Power
ε = Emissivity
σ = Stefan-Boltzmann Constant (5.67E-8 J/sec-m^2-K^4)
T = Temperature (in Kelvin)

Emissivity (ε) is defined as the ratio of radiation emitted from a sample surface to radiation emitted from a blackbody at the same temperature as presented in equation (2). It can be clearly seen from equation (1) that the Stefan-Boltzmann constant and temperature will cancel in this ratio. An ideal blackbody has an emissivity of unity and emits radiation according to Planck's law (equation 3).

$$\varepsilon(\theta, \lambda, T) = \frac{E_{Sam}(\theta, \lambda, T)}{E_{BB}(\theta, \lambda, T)} \quad (2)$$

where,

E_{Sam} = Emissive Power from Sample (test material)
E_{BB} = Emissive Power from Blackbody
θ = Emission Angle
λ = Wavelength

$$L(\lambda, T) = \frac{2hc^2}{\lambda^5 (e^{\frac{hc}{\lambda kT}} - 1)} \quad (3)$$

where,

L = Emitted Radiation
h = Planck's Constant (6.63E-34 J-sec)
c = Speed of Light (3E8 m/s)
k = Boltzmann's Constant (1.38E-23 J/K)

Emissivity is an important property that has been used in applications other than radiative cooling. Using emissivity, temperatures in manufacturing processes can be measured by a non-contact method [14]. Environmental scientists attempt to measure the emissivity of Earth's surface to use in atmospheric weather or global warming models [15]. Knowledge of the spectral emissivity of rare earth oxides can lead to their use in thermo-photovoltaic energy conversion devices [16].

There are a number of ways that emissivity can be measured, but they can be broadly characterized into two main categories: calorimetric (heating) or radiometric (optical) methods [17]. One calorimetric method involves heating a sample with a laser and determining the temperature distribution. This can be used to calculate the emissivity at the wavelength of the laser [18]. It is also possible to heat the sample and use a measured heat transfer rate to calculate emissivity [19,20]. In the radiometric method, the emissivity can be directly calculated by using a pyrometer [15,21,22,23], spectroscope [14,16], radiometer [24], or Fourier Transform Infrared (FTIR) spectrometer [17,25,26,27] to measure sample emission, or indirectly calculated by

measuring reflectivity and transmittance and applying Kirchhoff's law [28]. The blackbody spectrum can be theoretically calculated by using equation (3) [14], or created by a commercial blackbody [17] or from a cavity in a high emissivity material [25]. It has been found that using the FTIR for measurements provides the widest spectral range and most reliable data. As such, this measurement method was chosen in the present research.

1.2.2 Trends in Emissivity

Emissivity is a surface property and as such, is affected strongly by factors such as chemical composition, roughness, and porosity of the material's surface. Emissivity is also dependant on wavelength, emission angle, and temperature of the material. At higher temperatures, metallic samples will inevitably oxidize or undergo some type of other environmental reaction, unless testing is preformed under high vacuum or in a reducing atmosphere. The composition and morphology of the oxide layer will also have an effect on a material's emissivity. The effects of various factors on emissivity are discussed in the following sections.

1.2.3 Chemical Composition

The elemental make-up of a material strongly affects its emissivity. Each material has a distinct emissivity spectrum which depends on optical properties and lattice structure. Groups of similar materials (e.g. stainless steels) will tend to have similar emissivities. Duller, darker materials, such as some ceramics and graphite, generally have a higher emissivity [13,27] than shinier materials, such as metals. This high reflectivity of metals is one of two main reasons for the low emissivity of metals. Emissivity is inversely related to reflectivity; the higher the reflectivity, the lower the emissivity. Additionally, atoms of metallic materials are surrounded by a cloud of "free" electrons which also makes them good conductors. These electrons can scatter photons emitted from the surface, lowering the emissivity [29].

1.2.4 Wavelength

The dependence of emissivity on wavelength is strongly correlated to a material's composition. Again, un-oxidized metals tend to have similarly shaped spectra. A base metal's emissivity is generally highest at low wavelengths (~2μm) and decreases quickly in a parabolic fashion to about 5 μm then decreases slowly in a linear matter at higher wavelengths (Figure 5) [30,31,32]. Other materials, such as ceramics, can have very differently shaped spectra. This is highly dependent on elemental composition and impurities. Boron nitride for example exhibits a very uniquely shaped spectral emissivity as will be seen in a later section of this report.

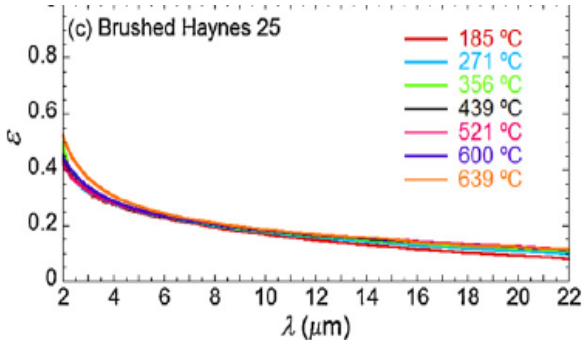

Figure 5. Wavelength dependence of spectral emissivity of Haynes 25 alloy in a reducing (N_2+5%H_2) atmosphere [30].

1.2.5 Sample Roughness

A rougher sample tends to have a higher emissivity than a more polished sample (Figure 6 and Table 2) [14,19,20,26,30]. However, once a sample is in the optically smooth region, changes in roughness have almost no effect on emissivity. The optically smooth region is defined in equation (4) [33]. To be optically smooth in the normal direction for the 2-10 micron range, the surface average roughness must be less than 0.25 microns. A rough sample will especially affect directional emissivity [34]. On a smooth surface, a photon emitted at a harsh angle will not impact a detector positioned in the normal direction. On a rough surface the same photon may be reflected off another section of the surface back to normal, increasing the directional emissivity in the normal direction.

It is possible for two samples with the same average surface roughness to have very different emissivities. In Figure 6, the Ra (average roughness) for sand blasted and brushed samples is very close, but in reality the brushed samples are only roughened in one direction while the sandblasted samples are roughened in two directions giving a higher actual roughness and so, a higher emissivity. The as-received wire-cut samples are the roughest and also have the highest emissivity.

$$d \ll \frac{\lambda}{8\cos\theta} \tag{4}$$

where,

d = Average Surface Roughness
λ = Wavelength of Incident Light (μm)
θ = Incidence Angle

Table 2. Effect of surface roughness on emissivity of epoxy-siloxane/40% Al composite coatings [26].

Sample	Roughness (μm)	Total Emissivity
1	0.92	0.14
2	1.01	0.15
3	1.23	0.18
4	1.39	0.20

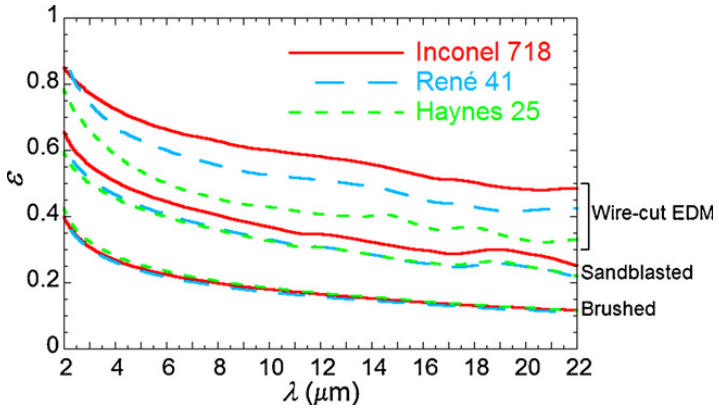

Figure 6. Normal spectral emissivity for three alloys with three surface conditions at 515°C in a reducing (N_2+5%H_2) atmosphere [30].

1.2.6 Emission Angle

The variation of emissivity with emission angle is a strong function of the material in question, as shown in Figure 7. In this figure 0^o is the normal direction and 90^o, at which all emissivities go to zero, is parallel to the surface. The emissivity of aluminum oxide, a ceramic, is approximately the same from 0-60^o, at which point it begins to decrease. Ice has a maximum emissivity at 0^o and decreases steadily as angle increases. A metal will tend to increase from the normal to a maximum at about 70-80^o [35], and then quickly go to zero at 90^o (Figure 8). This is predicted by electromagnetic theory [30], and is especially true at higher wavelengths, while at lower wavelengths the emissivity may remain steady until the abrupt decrease.

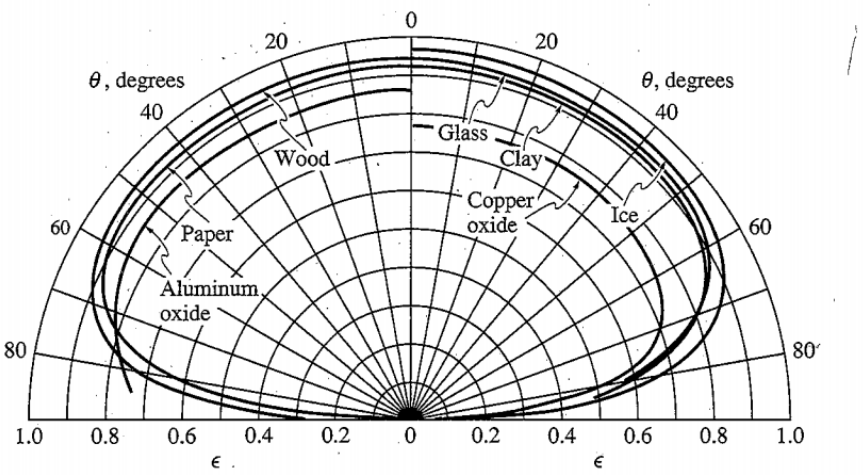

Figure 7. Angular variations in total emissivity for a variety of materials [12].

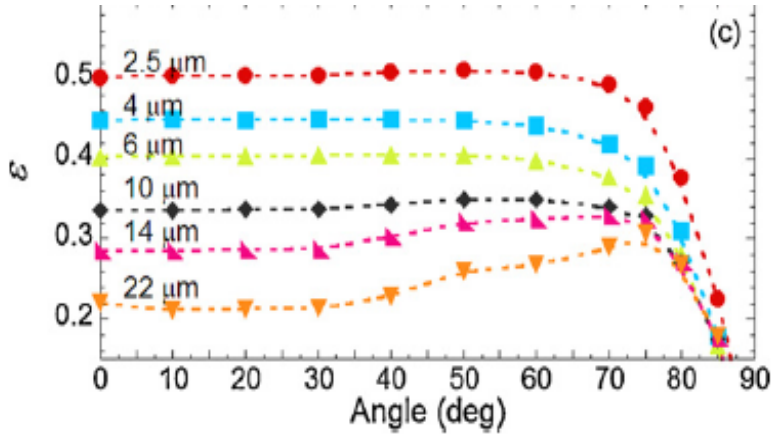

Figure 8. Angular variations in emissivity for Haynes 25 alloy at a number of wavelengths in a reducing (N_2+5%H_2) atmosphere [30].

1.2.7. Temperature and Oxidation

Changes in temperature and oxide growth go hand in hand and are therefore included together in a single section. If a sample is being tested under high vacuum or in a reducing atmosphere, temperature has very little effect on emissivity (Figure 9). At low wavelengths there

is a small increase in emissivity with temperature, while the increase is even less pronounced at high wavelengths.

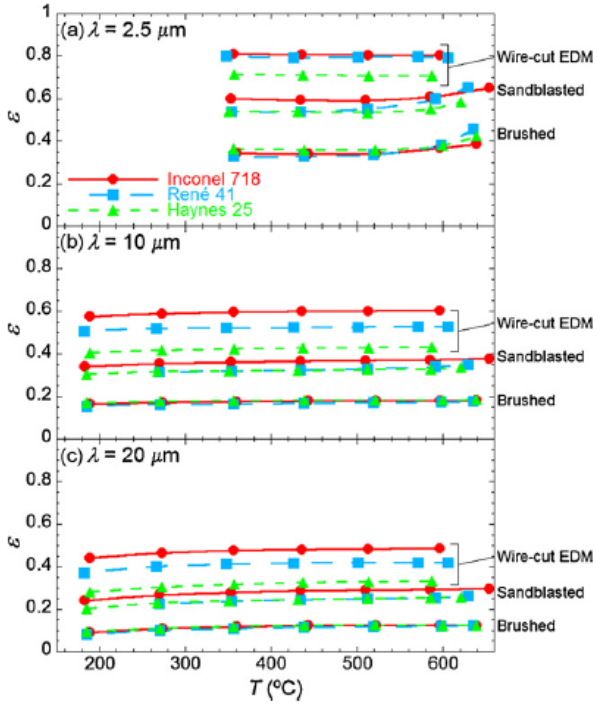

Figure 9. Variations in emissivity with temperature for three alloys at three surface conditions at (a) low, (b) medium, and (c) high wavelengths in a reducing (N_2+5%H_2) atmosphere [30].

Temperature has the strongest effect if oxide growth is considered. The growth of an oxide layer can be described by equations (5) and (6) [36]. In the equations 'n' is the empirical constant and depends on the materials being oxidized. If 'n' is close to 2, the growth is parabolic and tends to be a self-limiting and protective since the thickness approaches an equilibrium value. This is often the case for alloys high in chromium, since it forms a chromium oxide (Cr_2O_3) or Fe-, Cr- spinel oxide ($FeCr_2O_4$) layer which is protective. If 'n' is closer to 1, growth is linear, in which case oxides grow rapidly and can crack or spall because of poor adhesion. This is sometimes the case for iron oxides such as magnetite (Fe_3O_4) or hematite (Fe_2O_3) but studies have shown these oxides can also be protective [36] depending on the alloy.

An oxide will usually have a higher emissivity than a base metal [19,20] since an oxide is generally duller and darker. An oxide is also often rougher than the base metal, which has been shown to increase emissivity. However, it is possible for emissivity to decrease at very high temperature due to color change of the metal's surface or vaporization of the oxide layer [14,23]. Figure 10 shows the difference in spectral emissivity for five alloys at a temperature of 800 K. AISI 630, a stainless steel, has the highest chromium, so it forms a thin, protective oxide layer giving it the lowest emissivity. Alloys with less chromium or other alloying elements like Al or Si have thicker, less protective oxides so their emissivity is higher.

$$x^n = k_x t \tag{5}$$

where,

x = Thickness of Oxide
k = Rate Constant
t = Time
n = Empirical Exponent

$$k_x = k_x^0 \exp\left(-\frac{Q}{RT}\right) \tag{6}$$

where,

k^0 = Rate Constant at Zero Temperature
Q = Activation Energy for Oxidation
R = Ideal Gas Constant
T = Temperature

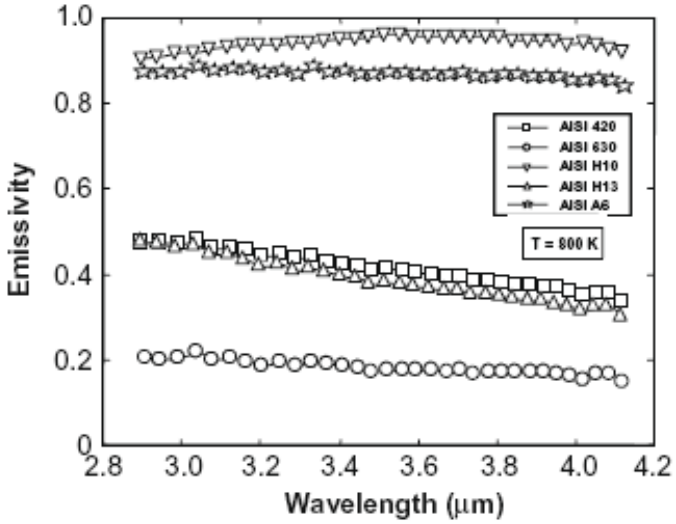

Figure 10. Effect of alloy composition on spectral emissivity [14].

The thickness of the oxide layer plays the strongest role in dictating the emissivity of the material as a whole. For a substrate alloy with a very thin oxide layer, almost all photons will be emitted from the substrate, and there will be little to no reflection or absorption in the oxide layer. As the oxide layer grows there is more reflection and absorption, as well as more photons emitted from the oxide, which would reduce the contribution from the substrate alloy and increase the emissivity.

The growth of the oxide layer can cause an interference pattern in the emissivity spectrum [21,22,31,36] which can be either constructive (a maximum peak) or destructive (a minimum peak), as shown in Figure 11. In one experiment [36], a 99.8% pure iron sample was oxidized in air at 480°C for 24 hours. For the first 20 minutes data was taken every 2-3 seconds, while later more time was allowed between data collection. The ramp up to temperature was performed in a reducing atmosphere to prevent pre-oxidation. The oxide growth occurs very quickly, with the first constructive and destructive interference peaks occurring within five minutes of being held at temperature. These peaks tend to shift to higher wavelengths at longer times. As the growth slows (>5 hours) there is very little change in the spectra with time, with only a slight

wavelength shift. It is possible to correlate the location of these interference peaks to the thickness of the oxide layer by making some assumptions about the optical properties of the two layers. Figure 12 shows that the oxide growth rate is parabolic and therefore protective [36]. About half of the total oxide thickness grows in the first 1000 seconds of the 24 hour test duration. Another experiment [37] testing the emissivity of a variety of polished, commercial aluminum-alloys confirmed that large changes in emissivity caused by oxidation occur within a period of a few hours (Figure 13).

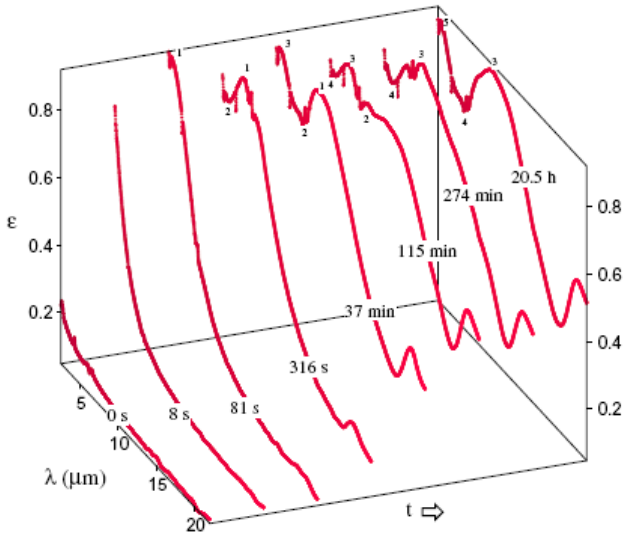

Figure 11. Spectral emissivity changes with time for an iron sample oxidized in air at 480°C showing constructive and destructive interference by oxide [36].

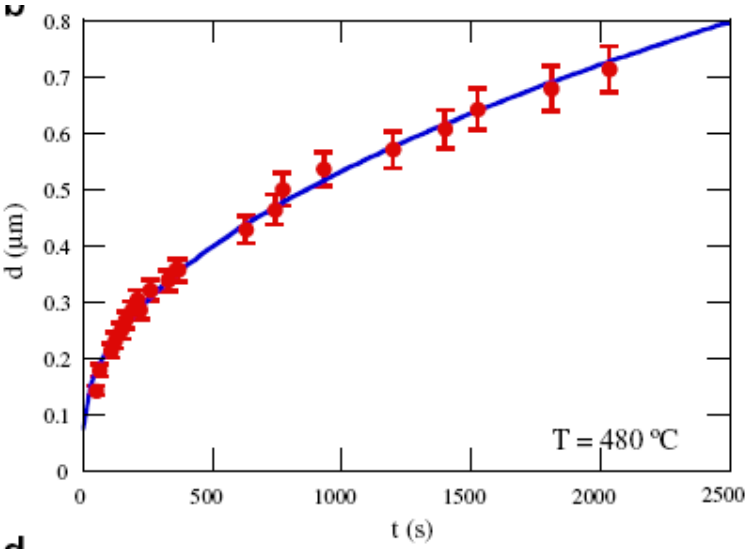

Figure 12. Calculated oxide thickness (red points) and best fit parabolic curve vs. time [36].

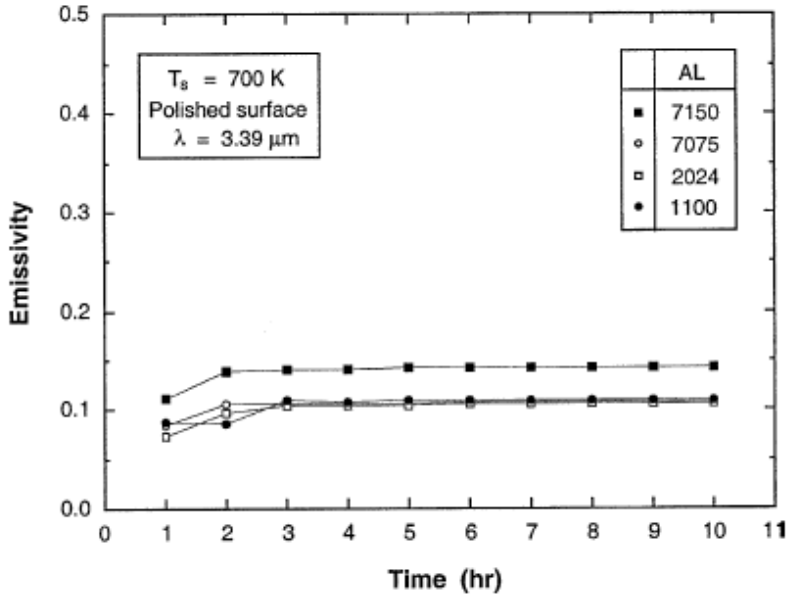

Figure 13. Effect of oxidation time on emissivity for four aluminum alloys in air at 700 K and wavelength of 3.39 microns [37].

2. Design and Construction of High Temperature Spectral Emissivity Measurement System

2.1. System Design and Construction

The emissivity measurement apparatus designed and constructed at the University of Wisconsin – Madison (UW) was in part based on the emissivity measurement systems at the National Physical Laboratory (NPL) in England [25] and the University of Pais Vasco in Spain [17]. A schematic illustration of the UW system is shown in Figure 14 and each design decision is explained below. Essentially, the system consists of four main components: a sample chamber, central lid, optics chamber, and an FTIR.

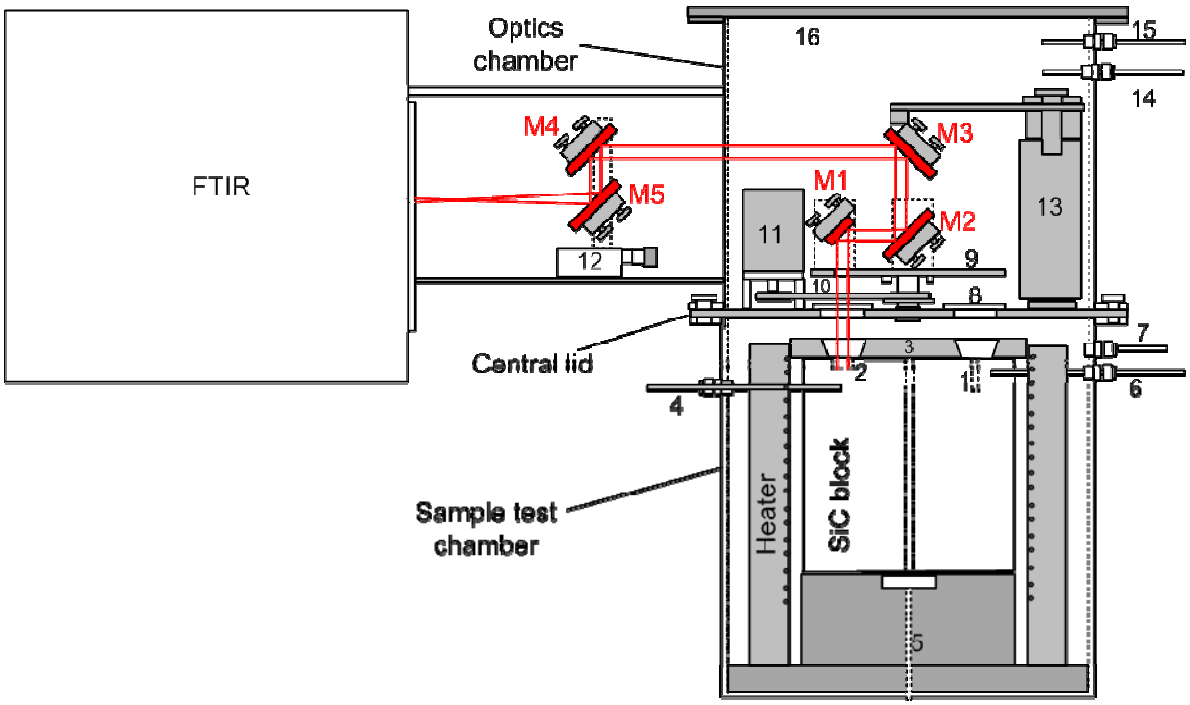

Figure 14. Schematic illustration of the high temperature spectral emissivity measurement system. M1, M2, M3 and M4 are flat mirrors and M5 is a parabolic mirror. M1 and M2 can rotate during emissivity measurement. 1: blackbody hole, 2: sample holder cavity, 3: insulation board for SiC block, 4: thermocouple for sample cavities, 5: gas inlet, 6: thermocouple for blackbody, 7: gas outlet, 8: CaF_2 windows, 9: rotational mirror platform for mirrors M1 and M2, 10: stainless steel mini chain for optics rotation, 11: step motor, 12: optical stage for mirrors M4 and M5, 13: vertical optical adjustment for mirror M3, 14: N_2 purge gas inlet, 15: N_2 purge gas outlet, 16: transparent plastic cover for watching optics chamber.

2.2. Sample Chamber

The sample chamber consists of the lower section of stainless steel pipe with welded bottom plate and top flange, as well as everything contained within: sample holder, heaters, and insulation. The central feature of the sample chamber is a silicon carbide block that houses the samples and the black body. Silicon carbide (SiC) was chosen due to its high thermal conductivity (125.6 W/m-K at room temperature), emissivity (~0.9), thermal shock resistance,

and resistance to oxidation. A custom-built silicon carbide cylinder, 8" in diameter and 8" high, was procured from Saint Gobain, Valley Forge, NY. The top circular face of the block has eight cavities machined circumferentially, seven with a diameter of 0.75" and depth of 0.25" to house the test samples. An eighth cavity with a diameter of 0.25" and depth of 1.5" is also provided and this cavity acts as the blackbody. Research [38] has shown that the emissivity for a high depth-to-diameter ratio can be calculated using equation (7). Inputting the blackbody dimensions from the block yields an emissivity of about 0.998 for our system which in a practical sense can be regarded as unity.

$$\varepsilon_c = \frac{\varepsilon_m(16h^3 + 8Dh^2 - (1-\varepsilon_m)(4D^2h + D^3) - \varepsilon_m 4Dh^2)}{4h^2(4h\varepsilon_m + D)} \quad (7)$$

where,

ε_c = Cavity Emissivity

ε_m = Material Emissivity

h = Cavity Depth

D = Cavity Diameter

The silicon carbide block also has a 0.25" diameter hole machined axially all the way through its center for introducing experimental gases to the system. Eight holes are drilled on the sides of the block in line with each of the eight cavities to allow for thermocouples to be inserted for the individual determination of the temperature of the eight cavities. The thermocouple lead rests the 0.5" below each of the cavities and given the high thermal conductivity of silicon carbide, it was assumed that the thermocouples corresponding to each of cavities would read the actual cavity temperature. The system is schematically shown in Figure 15. These thermocouples independently monitor the temperature of each sample as well as the blackbody to ensure the block has a uniform temperature distribution such that the temperature effects will cancel out when the emissivity of the sample is calculated. All the thermocouples used in this experiment were calibrated using a high precision platinum resistive thermal device (RTD).

The silicon carbide block rests on three layers of hard insulation, is surrounded by two semi-cylindrical radiation heaters, and is topped by more insulation. The heaters are controlled using the Lab-View computer program. This program also monitors the thermocouples and controls the stepper motor that is used to optically align the samples in each of the seven cavities. Originally three alumina heat shields were attached to the chamber lid above the block and could rotate to selectively view one sample at a time. However, the temperatures in the sample chamber caused the plates to become displaced, so they were replaced with insulation.

To confirm that the block heated uniformly a model was created in ANSYS, a finite element analysis program. The model simulates the presence of the silicon carbide block, the three original alumina heat shields, and the stainless steel lid. The heaters were simulated by imposing a 500^{o}C boundary condition to the outside of the silicon carbide block. Additionally, the lid to the optics chamber had a boundary condition of 100^{o}C, which assumes good cooling of the lid. The model was run with and without the heat shields (Figure 16). The upper third of the block, where the samples are located, showed a ~5^{o}C temperature gradient without and ~3^{o}C with heat

shields, respectively. The current design, with the heat shields replaced by soft insulation is expected to result in a temperature distribution within these two extremes.

Figure 15. Photograph of the silicon carbide block showing sample and blackbody cavities and two of eight thermocouples inserted.

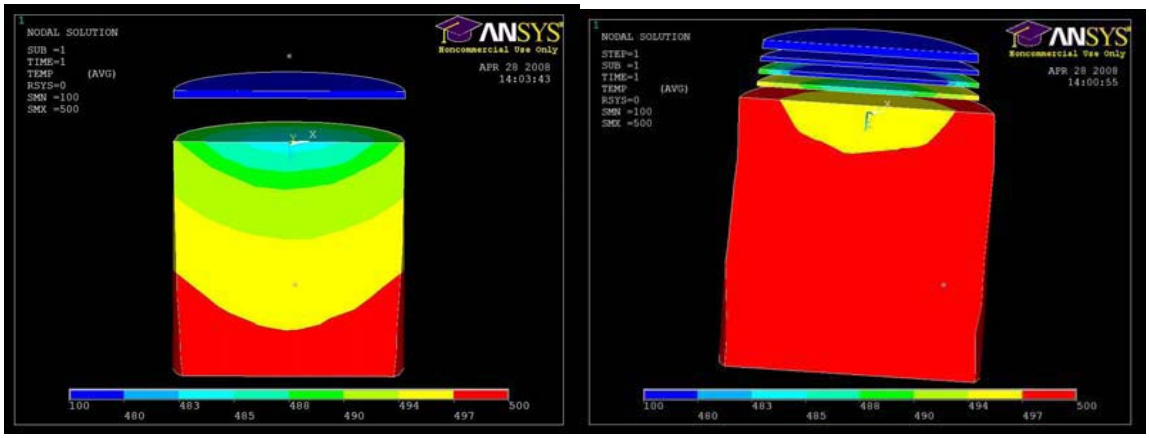

(a) (b)

Figure 16. ANSYS models of temperature gradients in silicon carbide block (a) without radiation shields and (b) with radiation shields.

The stainless steel chamber was machined to have holes which allow the eight thermocouples to enter the silicon carbide block, as well as six additional holes, one in the bottom plate and the other five around the side. To keep the chamber sealable, Swage-lok © fittings were welded on the inside of the steel chamber. The hole machined in the bottom is connected to a mass flow controller (MFC) which in turn is connected to the experimental gas cylinder (Figure 17a). It was determined that the maximum flow rate of 200 mL/minute would exchange all the gas in the chamber approximately every two hours. The other five machined holes are for feed-throughs for the heaters, a thermocouple for the heater, a pressure transducer which measures the pressure in the chamber, and an inlet/outlet pipe which connects to a series of valves which can pull vacuum on the can using a roughing pump, fill or flush chamber with experimental gas quickly, or connect gas outflow to composition analyzing system (Figure 17b).

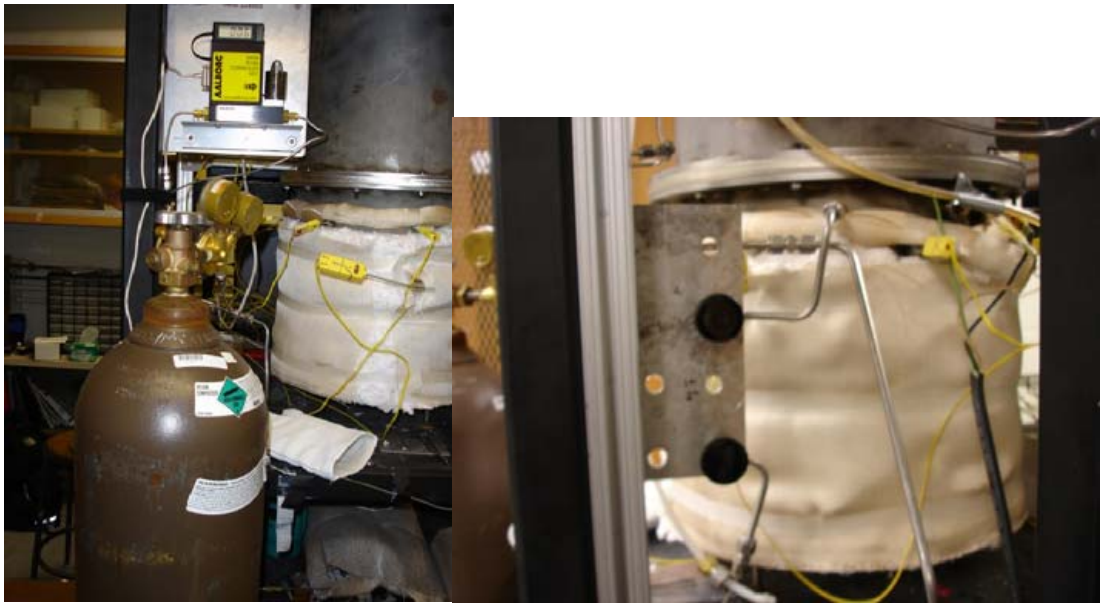

(a) (b)

Figure 17. (a) Mass flow controller and experimental helium cylinder and (b) sample chamber inlet/outlet and connected valve system.

2.3 Central Lid

The central lid is a 0.5" thick circular 304 stainless steel plate which separates the sample chamber and the optics chamber. It is connected to a flange welded to each chamber. There is a shallow groove machined in the top of the sample chamber flange and central lid, into which a rubber o-ring is inserted. This allows each chamber to seal and maintain a separate atmospheric condition. The central lid and flanges are tightened together with a series of bolts. Nine holes were machined into the lid, one in the exact center and the other eight directly above the sample and blackbody cavities in the silicon carbide block. The central hole had a tightly fit bearing pressed into it for use with the rotating platform.

Calcium Fluoride (CaF_2) windows are affixed above the other eight holes using aluminum window holders (Figure 18). Teflon rings are attached to both sides of the windows using vacuum grease, the window is centered above one of the holes in the lid, the holder is lowered into the position created by four bolts welded to the underside of the lid, and the entire assembly is tightened down using four nuts and a hex-head screwdriver. CaF_2 was chosen as the window material due to its high and nearly constant transmittance (Figure 19) over the wavelength range of interest (>80% from 1 to 9 microns) and the fact that it is not hydroscopic.

Figure 18. CaF_2 window, aluminum window holder, and Teflon rings.

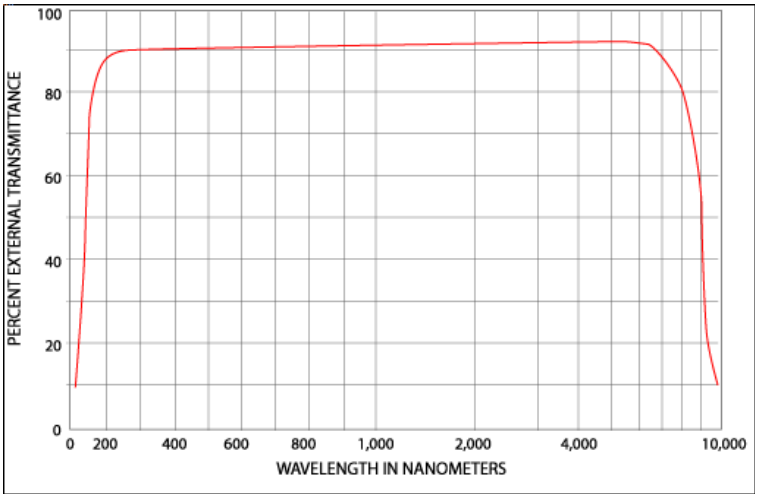

Figure 19. Spectral transmittance of CaF_2 [39].

The central lid also contains the water cooling system and welded bolts to attach the stepper motor and adjustable vertical cylinder to mount the third mirror. The water cooling system consists of an inlet manifold connected to the room's non-potable water supply which splits the water flow into four separate aluminum blocks which have been machined to seal to the lid and allow water to flow through. An outlet manifold combined the flow out from each aluminum block and directs it into the room drain. The cooling system keeps temperatures in the optics chamber below 100°C for testing up to 700°C which is well within temperature limits for optical components. Figure 20 shows the central lid and the original design for the rotating platform, including installed window holders, stepper motor, and the cooling system.

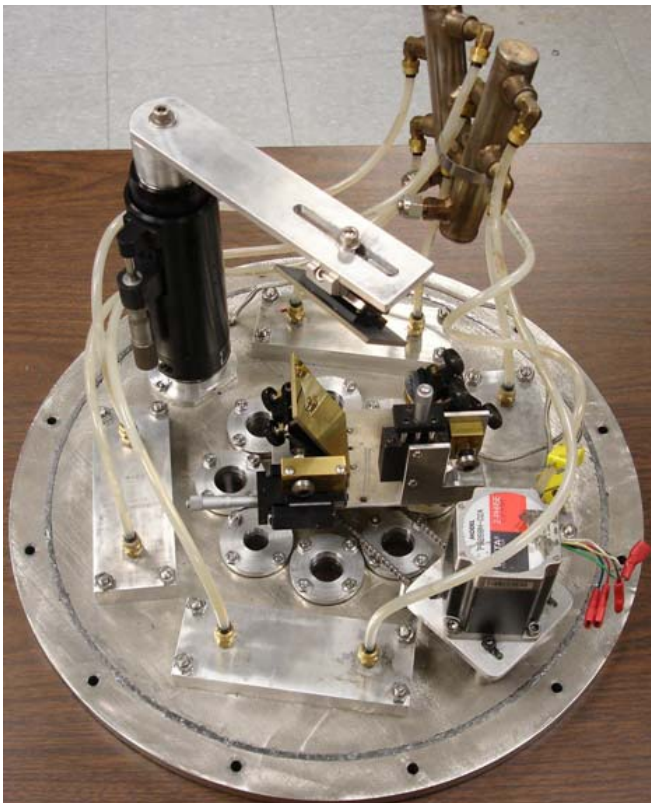

Figure 20. Central lid with rotating platform and third mirror installed.

2.4 Optics Chamber

The optics chamber consists of the stainless steel tube with welded flanges at the top and bottom and the attached stainless steel box (Figure 21), as well as the five-mirror system contained within. All five mirrors in the system are gold-coated, giving them a very high reflectivity in the infrared region. Three of the mirrors are contained in the cylindrical section of the optics chamber, two on a rotating platform and one on a vertical beam (see Figure 20), and the other two are contained in the box section (Figure 22). The stainless steel tube has five holes machined with welded fittings, two for gas inlet/outlet, one for a pressure transducer, one for thermocouple feed-throughs, and one for the stepper motor control feed-throughs. The stainless box also has one welded fitting for gas inlet.

Figure 21. External view of optics chamber with installed thermocouple and stepper motor feed-throughs.

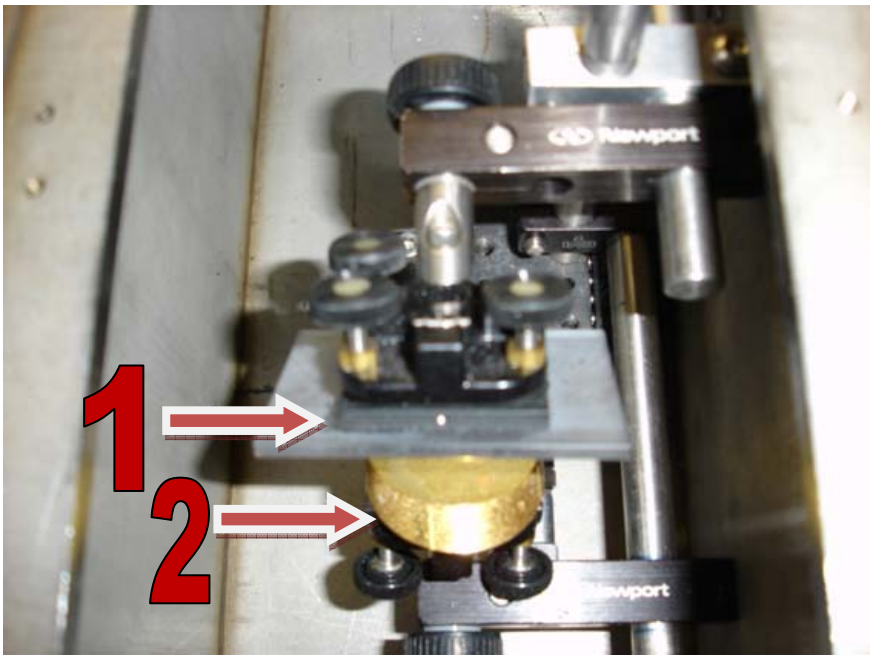

Figure 22. Internal view of stainless steel box section of optics chamber with (1) flat mirror and (2) parabolic mirror installed.

The rotating platform consists of an aluminum plate with a large, circular hole machined out of it, a stainless steel rod to insert into the bearing in the center plate, two mirrors, and two optical platforms. Each mirror is attached to an individual optical platform, which in turn bolts to the plate and allow for small adjustments in mirror position. The mirror mounts themselves contain two or three set screws which allow for small adjustments in mirror tilt. The first mirror, a small flat mirror, is mounted at a 45^{o} angle above the hole in the aluminum plate and is, when

the platform is inserted into the central lid, directly above the sample or blackbody cavities in the silicon carbide block.

A thin aluminum plate with small aperture is clamped to the platform below the first mirror. This aperture ensures that only light radiated from a small spot size on a sample will reach the mirror and be reflected to the other mirrors and eventually, the FTIR. The second mirror, a larger flat mirror, is also mounted at a 45^{o} angle directly along the central axis of the steel rod and by association, the silicon carbide block. The steel rod has an attached gear, which is connected to the stepper motor with a metal chain, and aluminum plate to hold the chain on the gear. The rotating platform, fully assembled, is shown in Figure 23.

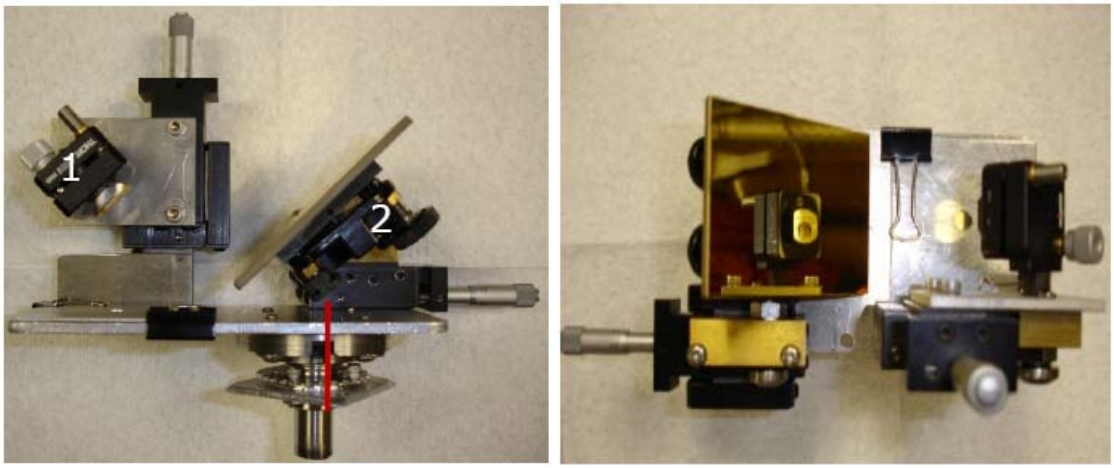

(a) (b)

Figure 23. Rotating platform with both flat mirrors installed, shown in (a) front view and (b) top view.

The third mirror is another large flat mirror, attached to the central lid by means of an adjustable vertical stage, and an aluminum cantilever beam. This mirror is positioned directly above mirror two, aligning it with the central axis of the system, and is mounted at a 45^{o} angle. This means that it reflects the light from mirror two (which is completely vertical) horizontally into the box section of the optics chamber.

The box section contains two mirrors both mounted on an adjustable optical stage, as seen previously in Figure 22. The top, or fourth, mirror is another flat, 45^{o} mirror which receives the light radiated horizontally from mirror three and reflects it completely vertically to mirror five. Mirror five is the only parabolic mirror in the system. It is aligned vertically to the input port for the FTIR, and the center is positioned 180.5 mm from the FTIR port, such that the focal point for light into the FTIR is the same point as the focal point for the mirror, determined from the provided schematic (Figure 24).

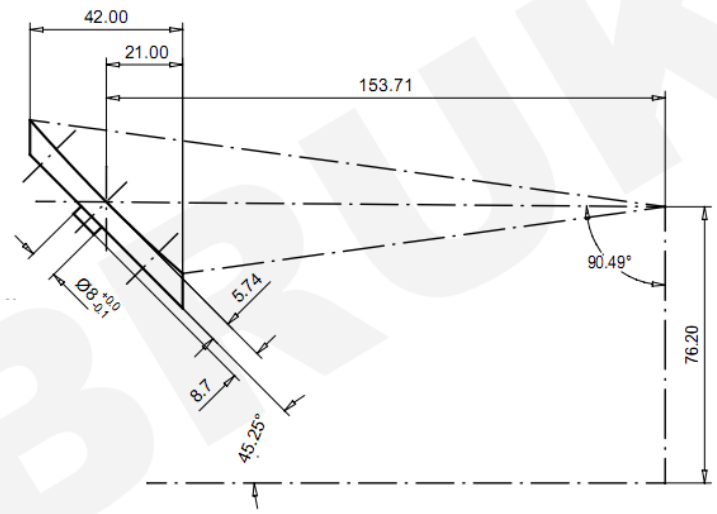

Figure 24. Schematic of parabolic mirror.

During the course of literature review for the project, it was discovered that the carbon dioxide and water vapor present in natural air have strong absorption bands in the wavelength range of interest. Some previous experiments [14, 37] were not able to confidently report results in these bands, as data taken there was unreliable. A spectrum taken of an infrared source interior to the FTIR confirmed this absorption (Figure 25). An ideal emission spectrum, such as from a blackbody, would be a smooth curve up to some maximum wavelength and another smooth curve back to zero, however there are strong deviations at wave numbers of 1500-2000 cm^{-1} (H_2O), 2500 cm^{-1} (CO_2), and 3500-4000 cm^{-1} (both). As this is a large fraction of the spectral range of interest, it is desirable to have reliable data in these regions.

It was decided to purge the optics chamber, as well as the FTIR, with pure nitrogen to reduce CO_2 and H_2O impurities. A large, 150 liter Dewar (Figure 26a) was filled with liquid nitrogen and transported into the laboratory. The liquid nitrogen gradually boils off, and this gas is either introduced into the optics chamber and FTIR through two MFC's (Figure 26b) or slowly vented into the well ventilated lab through a 23 psi relief valve. Figure 27 shows the CO_2 absorption region both without any nitrogen purging and after purging for a full day. While there is still some absorption, it is greatly diminished, and data can be taken in this region reliably.

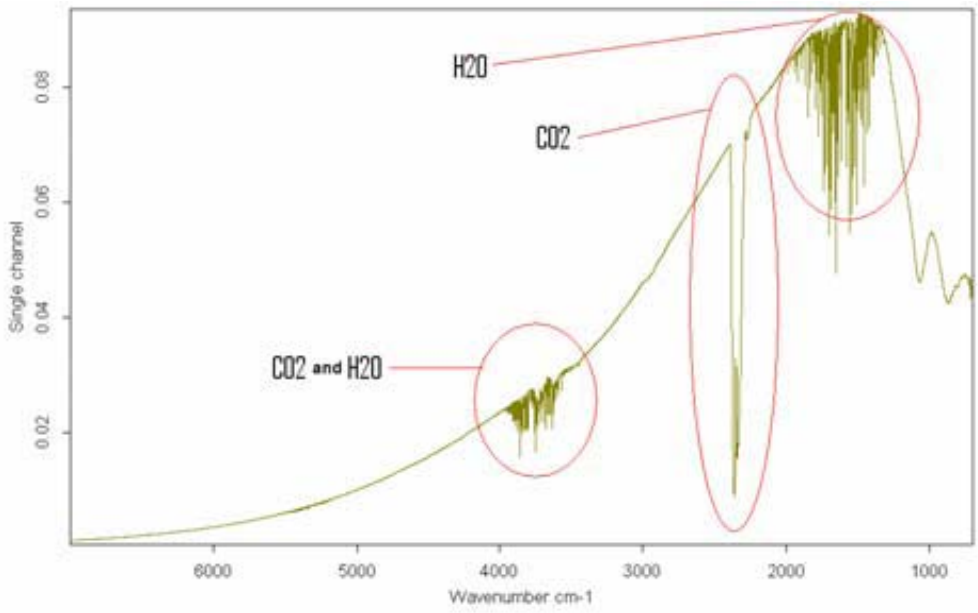

Figure 25. Spectrum of FTIR interior showing absorption by CO_2 and H_2O.

(a) **(b)**

Figure 26. (a) Liquid nitrogen dewar and (b) mass flow controllers for FTIR and optics chamber purge.

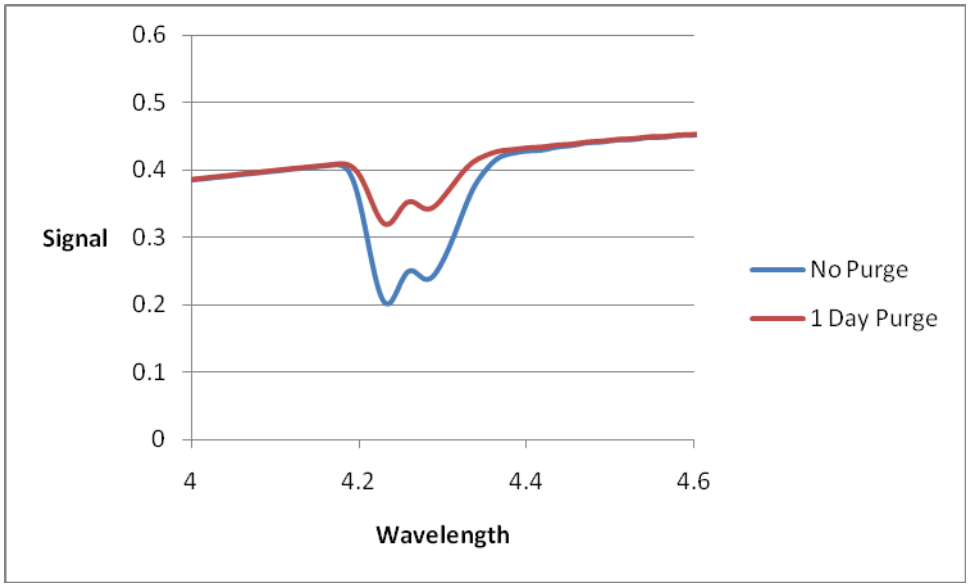

Figure 27. CO_2 absorption band without nitrogen purge and after one day purge.

2.5 FTIR

The FTIR used for data collection was a state-of-the-art model Vertex 70, procured from Bruker Optics, a German company which specializes in infrared test equipment. All mirrors used in the experiment were also provided by Bruker Optics. A schematic of the interior is shown in Figure 28. The photons, emitted from the sample or blackbody, enter through one of the inlet ports and are reflected off a series of gold-covered mirrors and through apertures to a potassium bromide (KBr) beam splitter and are then recombined to produce an interferogram. This signal is then reflected and focused into one of two detectors installed in the system. OPUS 6.5 software, provided by Bruker, performs a Fourier transform on the signal and displays the spectral intensity of the emitted light.

The first detector is a mercury-cadmium-telluride (MCT) detector, which has very high resolution, a spectral range from 1-25 microns and needs to be cooled continuously with liquid nitrogen. The second detector is a deuterated L-alanine doped triglycene sulphate (DLaTGS) detector. It has a smaller spectral range and about 30x lower resolution than the MCT, however it works at room temperature with no necessity for cooling. Since the spectral range for this experiment is restricted by the windows used and the resolution of the DLaTGS is more than sufficient for reliable data collection, this detector was used for most of the experiments. Figure 29 shows the photograph of the Bruker Optics FTIR system used in this research.

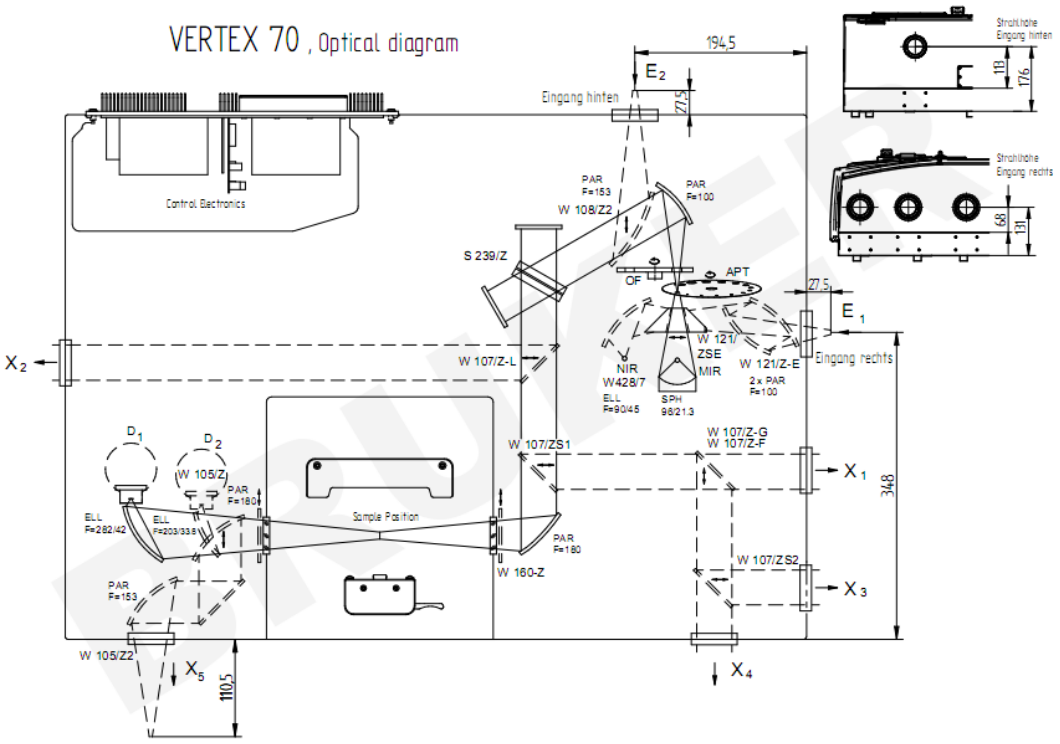

Figure 28. Schematic of the interior of the FTIR.

Figure 29. Picture of the Bruker FTIR system used in this project.

2.6 Alignment

After the design and construction of the system, it became necessary to calibrate the system with some widely researched standards and to develop a procedure for mirror alignment so that data taken would be reliable and repeatable. These steps were also necessary to comply with DoE's quality assurance protocols.

A number of methods were experimented with to get the five mirrors in the system into perfect alignment, including: high precision measurements of each mirror's location, mounting a laser in a sample cavity and reflecting it into the FTIR and maximizing the signal received by the FTIR by making slight changes to mirror set screws after they were positioned approximately.

All the methods were able to produce realistic results for one sample cavity, but the results were not repeatable and did not hold for other sample positions. The solution came with the purchase of a self-leveling laser. This laser can be mounted or used by itself, and the internal mechanics will cause lasers to be emitted perfectly level in five directions (upwards, downwards, and three in the x-y plane) even if the surface on which the laser is resting on is unbalanced.

A complete mirror alignment procedure has been developed as part of a complete testing procedure. In summary, the two mirrors on the rotating platform are aligned outside the optics chamber by means of the mounted laser (Figure 30) and two plates machined to have cavities similar to sample and blackbody cavities in the silicon carbide block. The three other mirrors are installed and aligned individually, again using the laser. When this is complete, the rotating platform is inserted into the central lid, the chain is attached, and data can be taken.

To test how well the procedure aligns the optics for each sample position, emission signals were compared for each empty sample cavity. The block was precisely leveled before testing to ensure that the bottom of each cavity was the same distance from the first mirror. The results of the test are shown in Figure 31. Only a section of the spectra is shown so that differences are visible. As can be seen, there is some small variation between sample positions. The maximum difference across the entire wavelength range is about 10% between maximum and minimum positions. Therefore, to be conservative, results obtained using this mirror alignment procedure is stipulated to have +/- 10% error across the entire spectrum.

Figure 30. Laser installation for aligning the rotating platform.

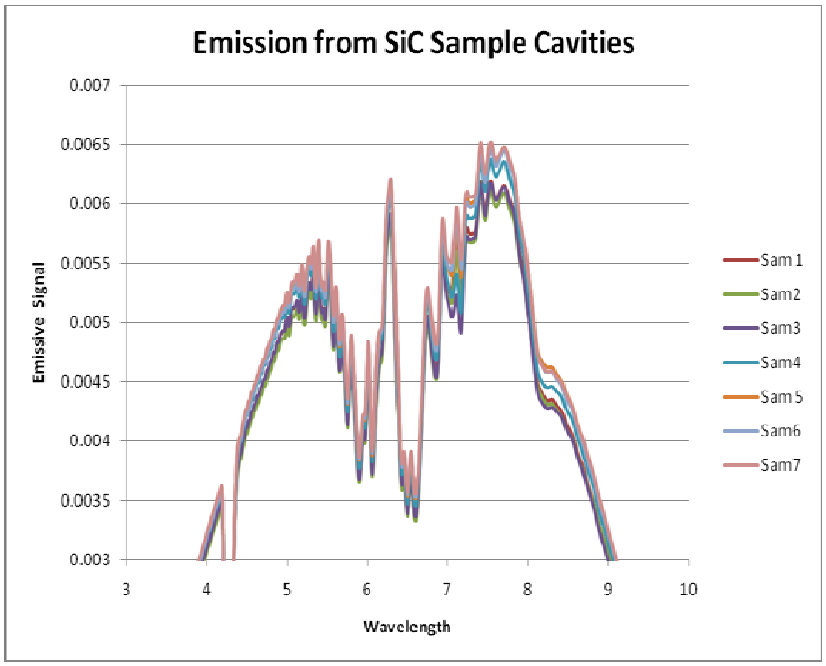

Figure 31. Variation in emission signal from each sample cavity in the silicon carbide block.

2.7. System Calibration

To ensure DoE quality assurance requirements, emphasis was initially placed on achieving reproducibility in emissivity data and to reliably bracket error margins. Since metals tend to oxidize and affect emissivity, it was decided that inert ceramic standards SiC, BN and Al_2O_3 would be used for this purpose. Figure 32 shows a photograph of these ceramic samples. Figures 33, 34, and 35 show the reproducibility in emissivity data for SiC, BN and Al_2O_3 for measurements made at 600^{o}C for three separate tests. These measurements were performed on different days and the optics was realigned for each measurement. These measurements clearly show that spectral emissivity measurements within 5% range can be achieved. Because all the samples were placed in the same chamber, the exposure atmosphere and time and other measurement parameters are exactly identical for all samples, and the systematic measurement errors from the equipment are the same for all samples and the blackbody. Thus, during calculation of the emissivity based on $\varepsilon = \frac{S_{sample}}{S_{blackbody}}$, the measurement errors will cancel out, thereby providing for further refinements in precision and repeatability of measurements.

Figure 33 shows the measured emissivity and literature values of SiC from the reference "*Y.S. Touloukian and D.P. Dewitt, Thermophysical Properties of Matter, v. 8. Thermal and Radiative Properties, IFI/Plenum, NY, 1972"*, which is a compilation of data from a large number of previous literature and has the most complete spectral emissivity values of SiC, BN and Al_2O_3. The emissivity of SiC changes very slightly with wavelength in the wavelength ranges tested (2-9 μm). Emissivity data for SiC from literature measured by different methods, ranges typically from 0.83 to 0.96, and our measurements using the custom developed facility are well within the literature data range. The measurement error for SiC is less than 5% based on three different tests.

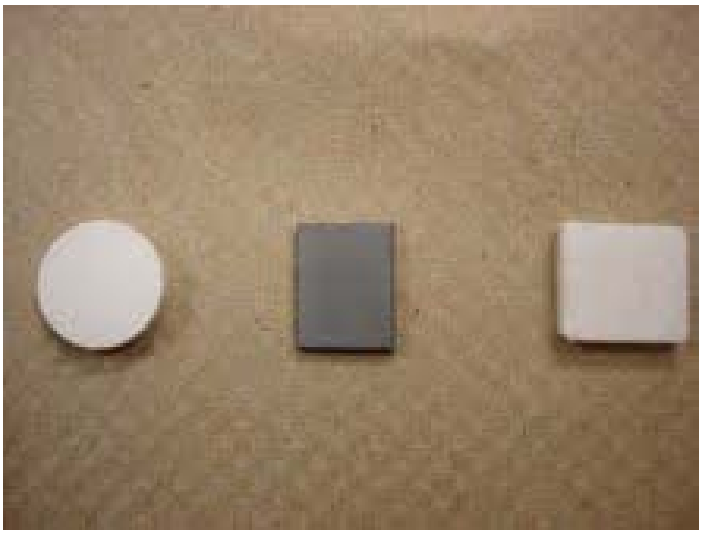

Figure 32. Ceramic samples used for system calibration (from L-R: BN, SiC, alumina).

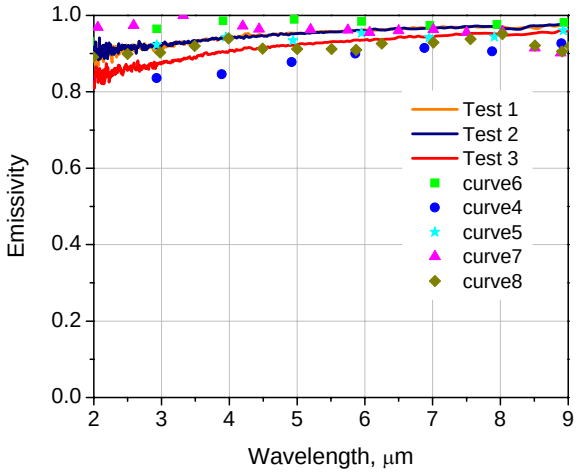

Figure 33. Spectral emissivity of silicon carbide measured at 600°C in three separate tests and comparison with literature data. The literature values (Curves 4-8) were selected from reference, *Y.S. Touloukian and D.P. Dewitt, Thermophysical Properties of Matter, v. 8. Thermal and Radiative Properties, IFI/Plenum, NY, 1972 (Ref. 40)*. Tests 1, 2, and 3 are measured emissivity values.

As shown in Figure 34, the emissivity measurement for BN is also very repeatable. The standard deviation of three tests is less than 5%. The emissivity of BN increases between 2 and 6 μm wavelength and then decreases sharply and reaches a minimum at 6.5 to 7 μm wavelength. The measured emissivity of BN is also well within the published literature data. Moreover the rather unique trend in variation of emissivity of BN with wavelength is also highly repeatable.

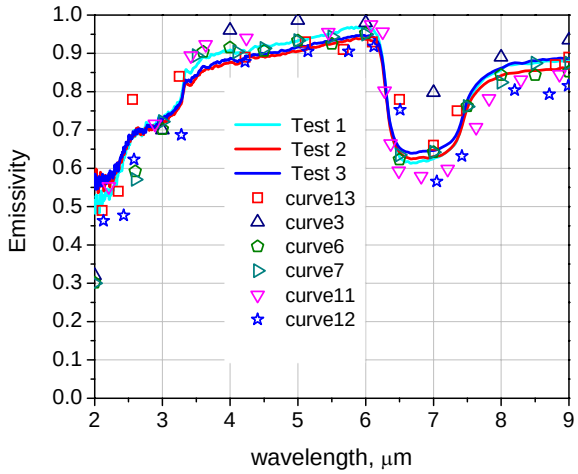

Figure 34. Spectral emissivity of boron nitride measured at 600°C in three separate tests and comparison with literature data. The literature values (curves 3, 6, 7, 11-13) were selected from reference, *Y.S. Touloukian and D.P. Dewitt, Thermophysical Properties of Matter, v. 8. Thermal and Radiative Properties, IFI/Plenum, NY, 1972 (ref. 40)*. Tests 1, 2, and 3 are measured emissivity values.

As shown in Figure 35, the measured emissivity of alumina ranged from 0.7 and 0.99 for wavelengths of 2 μm and 8-9 μm, respectively. From three independent measurements, it can be seen that the emissivity of alumina is also very repeatable and standard deviation of the three measurements is less than 5%. The literature values on the emissivity of alumina show a reasonably large scatter especially at low wavelengths. When comparing the measured emissivity of alumina with literature values at a wavelength range of 2-9 μm, the scatter in data in literature above 5-6 μm wavelength is very small and our measured emissivity values agree well with the literature data at 5-9 μm wavelength range. The measured emissivity of alumina at 2-5 μm is also in agreement with literature data range though there is a large scatter between literature values in 2-5 μm wavelength range.

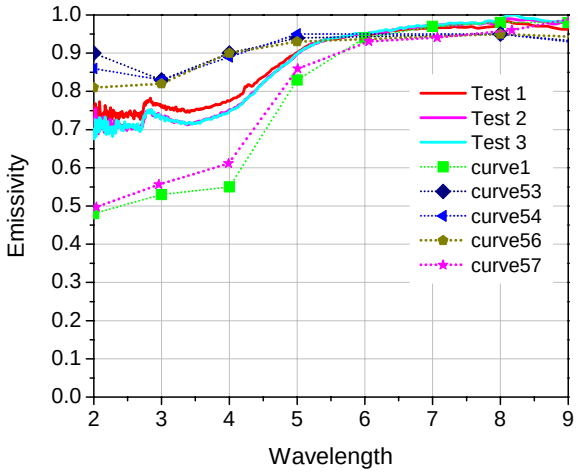

Figure 35. Spectral emissivity of Al_2O_3 measured at 600°C in three separate tests and comparison with literature data. The literature values (curves 53-57) were selected from reference, *Y.S. Touloukian and D.P. Dewitt, Thermophysical Properties of Matter, v. 8. Thermal and Radiative Properties, IFI/Plenum, NY, 1972 (Ref. 40)*. Tests 1, 2, and 3 are measured emissivity values.

After comparing the measured emissivity of SiC, BN and Al_2O_3 with literature values and repeating the measurements for each material, it can be concluded that the emissivity measurement our custom built facility is reliable and repeatable. The emissivity of the three materials agree well with literature values and the overall measurement error is less than 5%. There is a large spread in the literature values for alumina, and the data from the present research falls well within this spread. Therefore this system calibration was declared a success and testing of actual samples commenced. All subsequent testing included at least one, and usually all three, ceramic samples as controls. If the emissivity of any of the controls was significantly different during a test, it would be obvious that something was not correct, and the test would be paused until the issue was resolved.

2.8 Uncertainty Analysis

An uncertainty analysis of the emissivity measurements was also performed. To some extent such an analysis was prompted by our meeting with Mr. Gary Roberts, quality assurance expert at INL who impressed to us the importance of this type of analysis for the construction of prototype VHTR under construction at INL. The calculation was performed with previously collected data for the emissivity of tantalum at 500°C, as well as systemic data from thermocouple calibration and FTIR response. The FTIR response was determined by the variation in observed spectra over 100 spectra, with each spectra being composed of 16 scans. The response of the FTIR was very regular over much of the range of the instrument, except below 750 wave numbers and above 9500 wave numbers. Also, the atmospheric compensation routine of the FTIR software did not correctly compensate for H_2O and CO_2 for 22 of the 100 scans. Normally, data collected in these two bands is not considered reliable. Purging of the interior of the FTIR reduces the effect of atmospheric interference. A sample distribution for variation on one specific wave number over the entire spectra is shown in Figure 36.

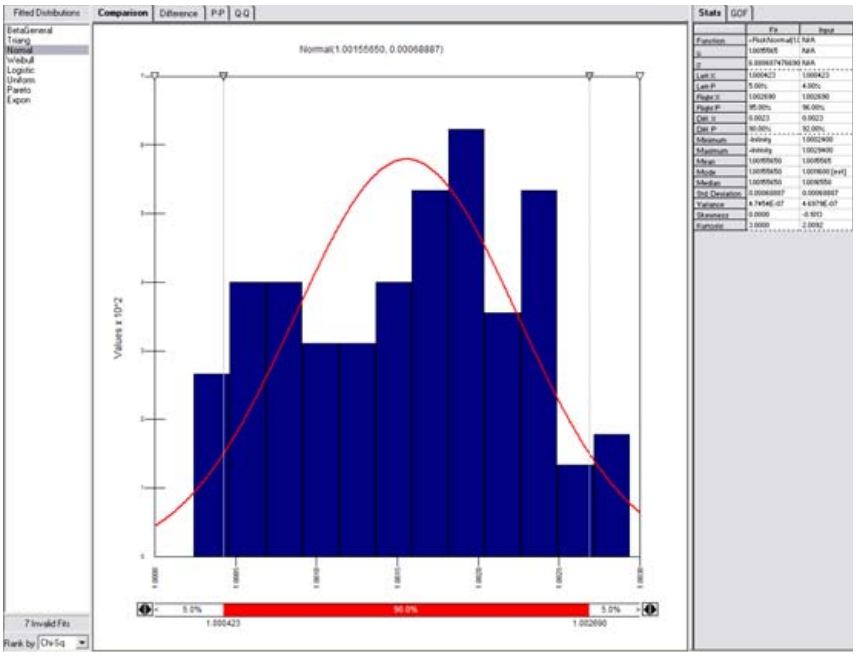

Figure 36. Statistical variation in spectra at one wave number.

The uncertainty analysis also showed that the most important parameter on the uncertainty in emissivity is temperature. The errors in thermocouple calibration are due to differences between thermocouples and a NIST certified platinum RTD, as shown in Figure 37. Uncertainty could also come in natural variation in room temperature. However, the bulk of the variation in temperature will occur due to temperature fluctuations of the silicon carbide block, due to PID controlled heating.

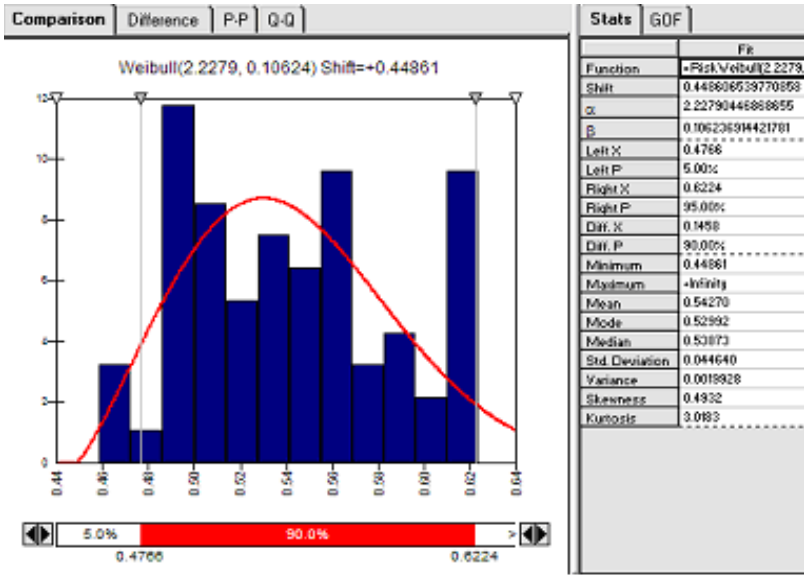

Figure 37. Distribution of the difference between RTD and Sample 1 thermocouple.

Finally, the effect of the blackbody on the calculated emissivity was investigated. The blackbody has a much smaller effect, but the emissivity of the blackbody does vary over both the temperatures and wavelengths of interest because the emissivity of SiC varies. However, the total variation in blackbody emissivity is about 1.5%, leading to a small variation in calculated sample emissivity.

Modeling each input uncertainty with distributions and Monte Carlo simulation was accomplished using the Excel plug in @Risk. The output was anomalous for smaller wave numbers, but gave good results for large wave numbers.

In conclusion, these uncertainty analyses along with the calibrations indicated that accurate and reproducible data can be obtained from the spectral emissivity measurements system. Consistent with quality assurance requirements, errors in measurements, small as they are, have been quantified.

3. Spectral Emissivity of Reactor Materials

3.1. Composition of the Alloys Tested:

Table 3 shows the nominal compositions of the alloys tested for high temperature spectral emissivity.

Table 3. Nominal compositions (wt.%) of the materials tested in this project.

Alloy	Composition (wt.%)
SA508	Fe-0.17Cr-0.17Ni-0.48Mo-1.28Mn
T22	Fe-0.31Si-0.49Mn-2.19Cr-0.91Mo
T91	Fe-0.45Mn-0.28Si-0.21Ni-8.37Cr-0.9Mo-0.17Cu
IN 800H	Fe-0.08C-22Cr-32.5Cr-0.38Al-0.38Ti
Haynes 230	Ni-22Cr-2Mo-14W-0.4Si-0.5Mn-0.3Al-5Co-3Fe
IN617	Ni-22Cr-9Mo-1.2Al-22.5Co
SS 316	Fe-17Cr-2.5Mo-12Ni
SS 304	Fe-19Cr-9.5Ni-1Si-2Mn

3.2. SA 508

SA 508 is a very low alloy steel that is primarily being considered for use as the RPV material for the VHTR due to its current use as the material for the construction of LWR RPV. Due to the low concentrations of alloying elements such as chromium, SA 508 is not corrosion resistant and will oxidize considerably, even at medium temperatures. SA 508 steel is predominantly pure iron, and therefore the oxide would be expected to consist of a thin hematite (Fe_2O_3) inner layer, and a thick magnetite (Fe_3O_4) outer layer [36].

Mirror polished samples of SA 508 (Ra = 0.004 μm) were tested for spectral emissivity in air for test duration of up to five hours test duration at 350°C, 500°C, and 700°C. Figure 38 shows the spectral emissivity data for spectral emissivity data taken at 350°C. Measurements were made after 1, 2, 3, 4, and 5 hours of exposure at temperature, however, the data taken for 1, 2, and 5 hours are reliable because some sticking issues in the rotating platform were encountered for measurements taken after 3 and 4 hour tests. The spectral emissivity data for SA 508 at low temperature (350°C) shows the trends expected for slightly oxidized steel: highest at low wavelengths with a fairly gradual decline with increasing wavelength. The emissivity values are generally lower than would be expected of an oxide, indicating that the small thickness of oxide layer results in substantial contributions from the substrate steel. There was essentially no change in emissivity values between 1 and 5 hours because of the slow rate of oxide growth at this low temperature. Plan view SEM imaging (Figure 39a) of the sample after testing did not show a clear appearance of oxidation, however the corresponding EDS spectrum (Figure 39b) did show 9% oxygen, so some oxidation of the surface did occur during testing.

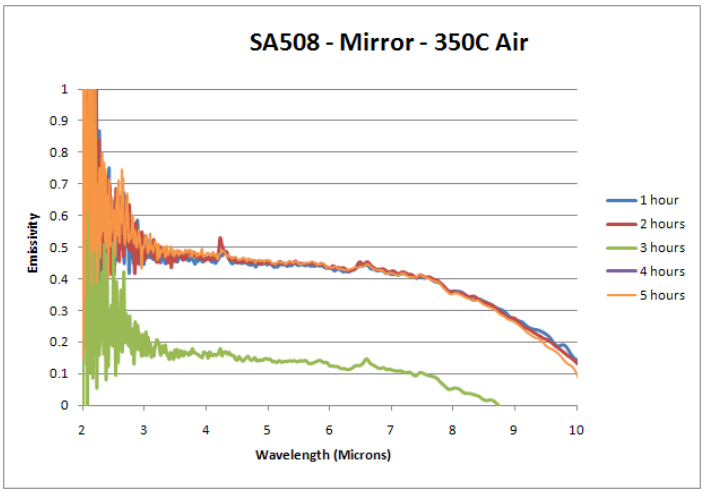

Figure 38. Spectral emissivity of mirror polished SA 508 in air at 350°C. Values reported for 1, 2, and 5 hours are regarded as reliable.

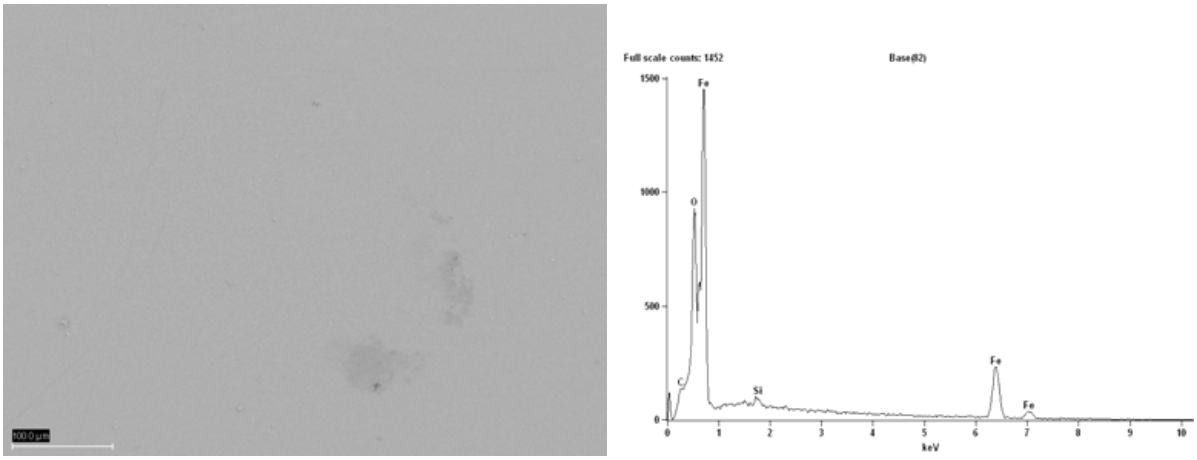

(a) (b)

Figure 39. (a) Plan view SEM image of mirror-polished SA 508 tested at 350°C for 5 hours (b) corresponding EDS elemental spectrum of the oxidized surface.

Emissivity spectra at 500°C and 700°C (Figures 40 and 41, respectively) both show relatively high emissivities (0.8-0.9) due to higher levels of surface oxidation. For 500°C, emissivity increases slightly with increasing wavelength while at 700°C the emissivity is fairly constant. Both show little variation with exposure time at low wavelengths with some variation at higher wavelengths. This can be caused by two separate effects. First, as the oxide grows in thickness and sporadic spallation can occur. The oxide will continue to grow at these locations, but the lower thickness in these regions can affect the emissivity of the overall surface. Visual inspection of the samples after testing which showed a non-uniform surface supports this observation. Secondly, the continued growth of an oxide layer can cause constructive and destructive optical interference which lead to maxima and minima in spectral emissivity which tend to move to higher wavelengths with increasing time. The variations in spectral emissivity data observed for samples tested at 700°C sample emissivity especially support the interference theory.

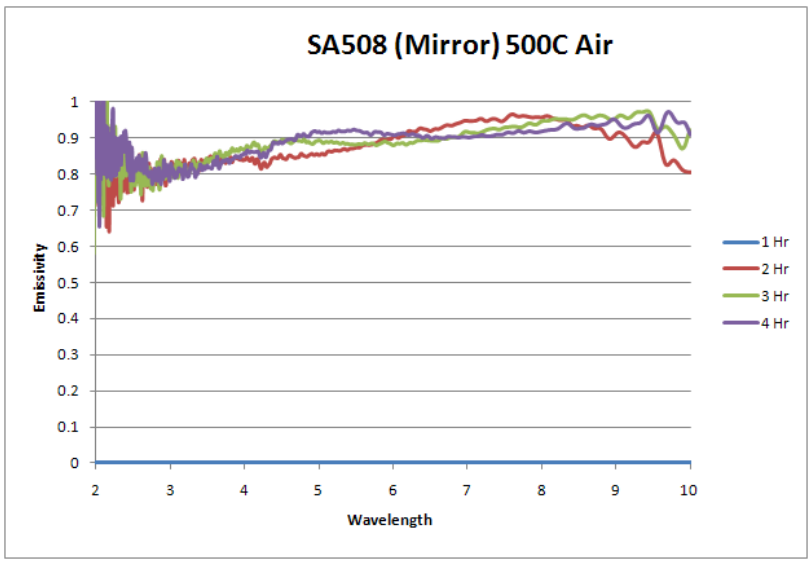

Figure 40. Spectral emissivity of a mirror polished SA 508 steel at 500°C.

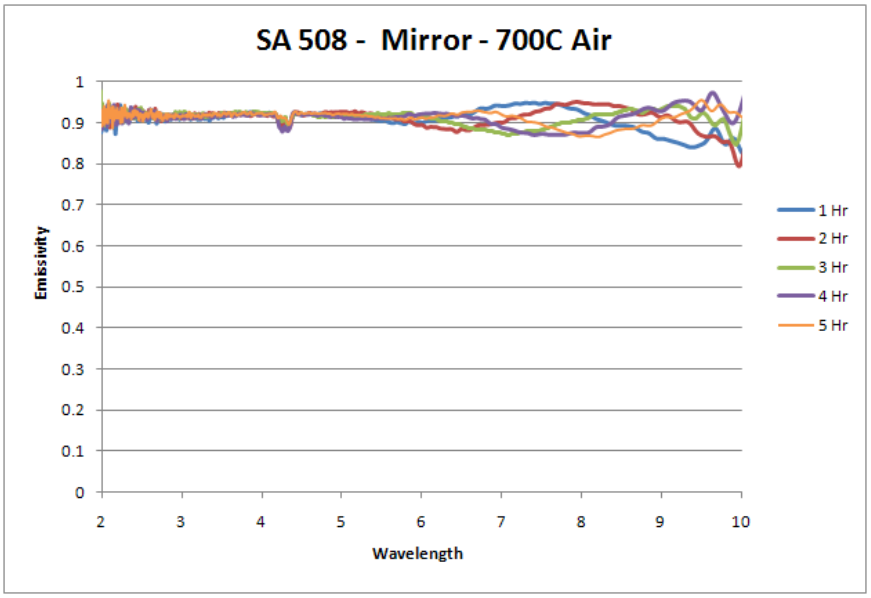

Figure 41. Spectral emissivity of mirror polished SA 508 steel at 700°C.

Plan view SEM imaging of SA508 samples tested at 500°C and 700°C (Figures 42a and 42b, respectively) shows pronounced oxidation. The grain boundaries and polishing marks that were clearly visible on the mirror polished sample have been completely obscured by an oxide layer. The corresponding EDS surface scans (Figures 43a and 43b) indicate about the same levels for oxygen (~25%) in the near-surface regions of these samples. Profilometry of the samples tested at 500°C and 700°C have been compared with those of the mirror polished (pre-testing) sample (Figure 44). While both tested samples were rougher than a mirror polished sample, the samples tested at 700°C was significantly rougher (Ra=1.0251 µm) than the samples tested at 500°C (Ra=0.029 µm). This increased surface roughness could also contribute the higher emissivity.

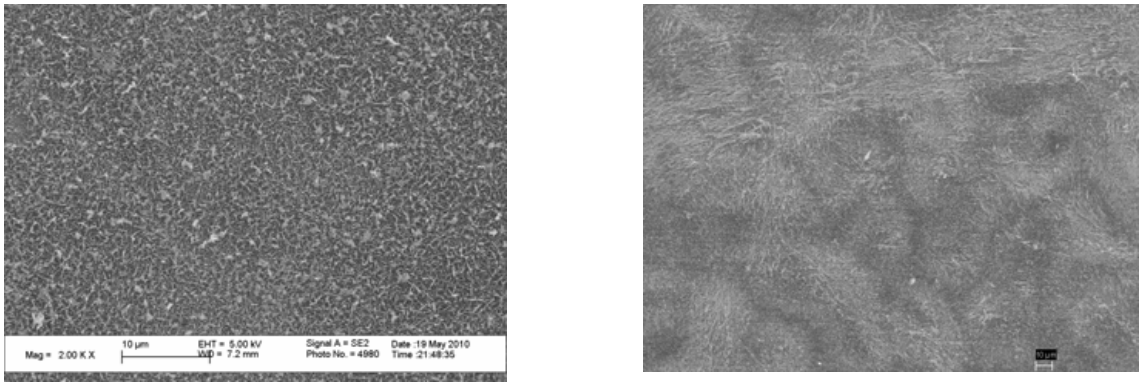

(a) **(b)**

Figure 42. SEM plan view images of the surface of SA508 steel after emissivity testing at (a) 500°C and (b) 700°C.

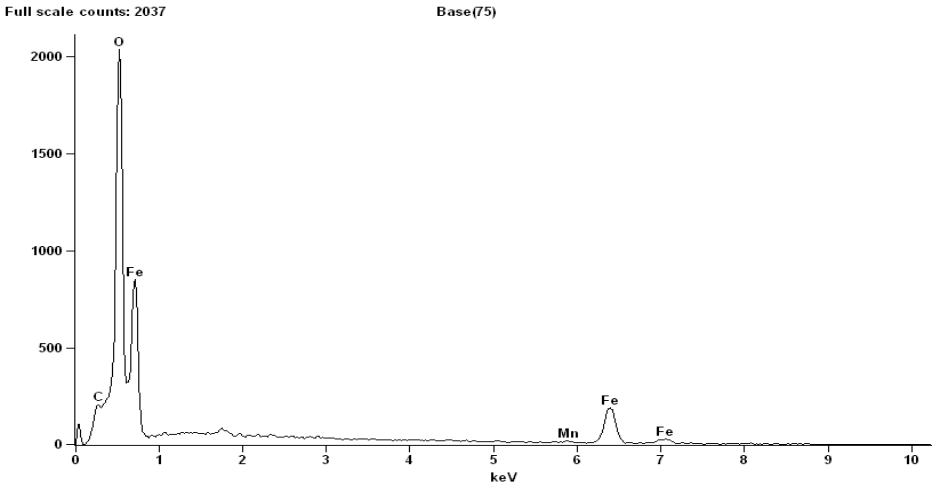

(a)

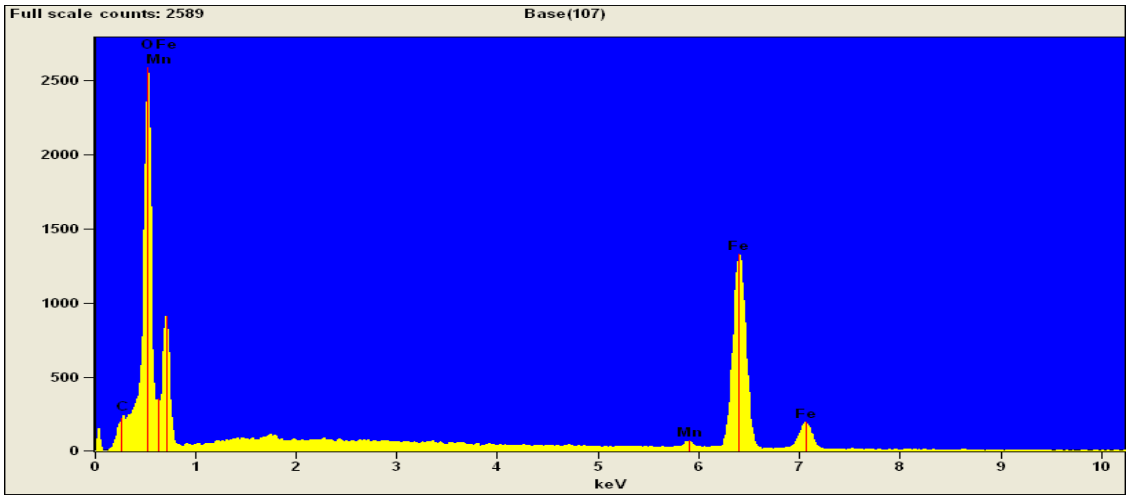

(b)

Figure 43. SEM-EDS elemental analysis of the surface of the SA508 steel samples after emissivity testing at (a) 500°C and (b) 700°C.

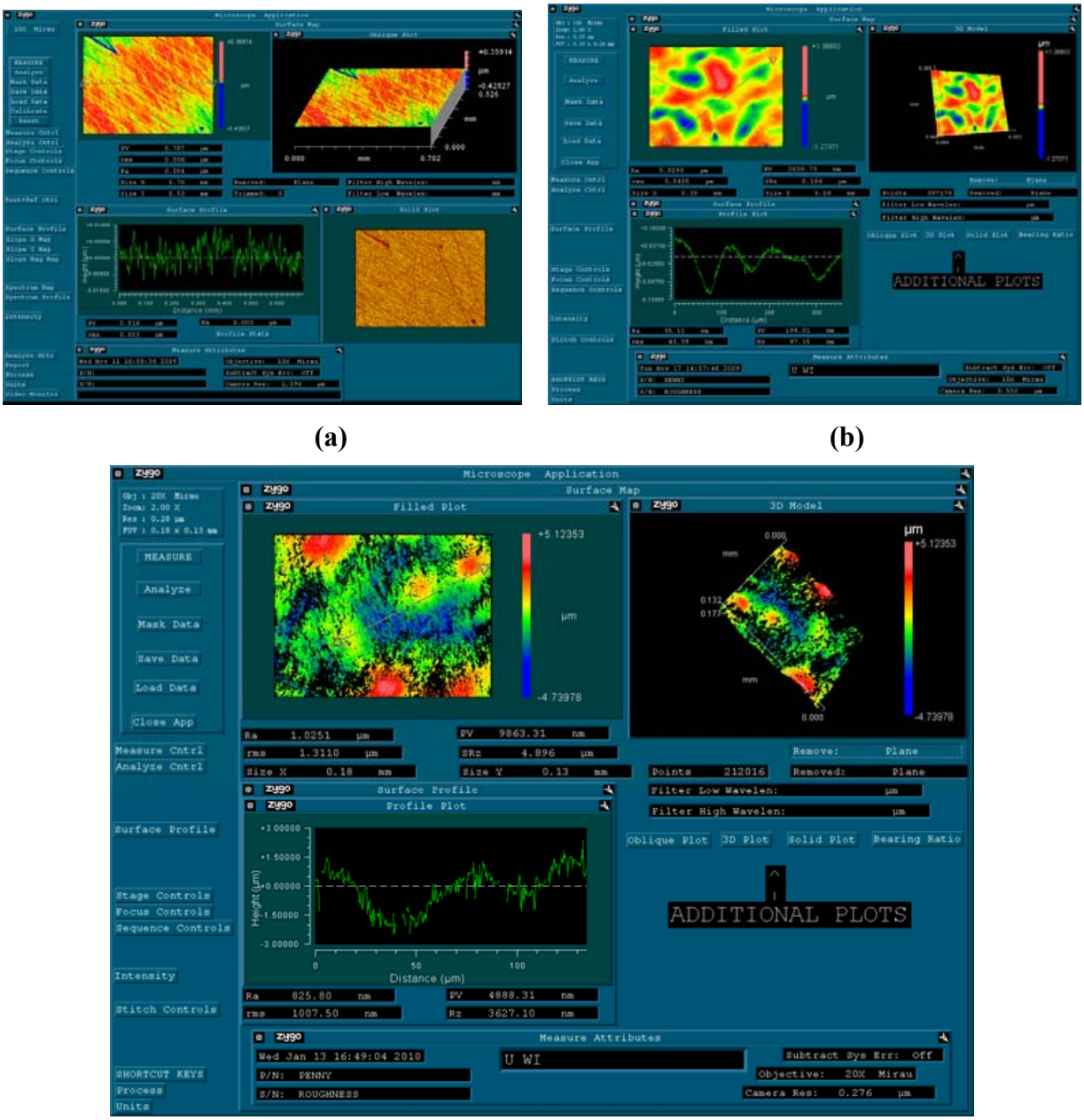

Figure 44. Profilometry of the surface of the SA 508 steel samples (a) before emissivity testing, (b) after emissivity testing at 500°C, and (c) after emissivity testing at 700°C.

Since the growth of an oxide layer seems to have profound effect on spectral emissivity values, the SA508 samples from the 500°C and 700°C tests were mounted in cross-section to evaluate the oxide layer thickness (Figure 45). Both samples exhibit an internal oxidation layer in addition to the stoichiometric oxide layer. The total thickness for the two layers at 500°C is about 2-3 microns, while at 700°C, the total thickness is much greater and about 40-45 microns. The oxide thickness at 500°C could allow some substrate contributions to emissivity, while at the 700°C the much greater thickness agrees with oxide growth rate theory and means that the sample emissivity is only that of the oxide layer.

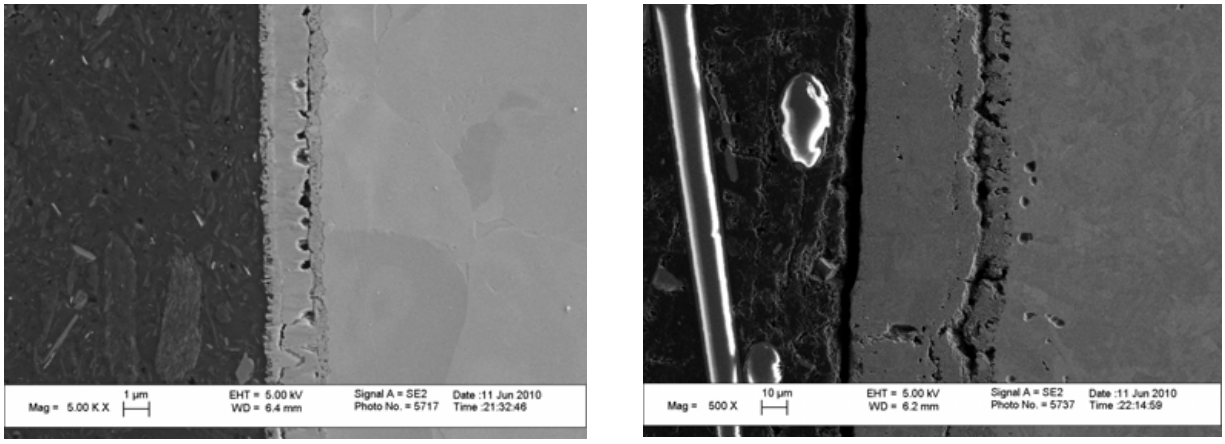

(a) **(b)**

Figure 45. SEM cross-sectional images of the SA508 steel showing the oxide layer thickness after emissivity testing at (a) 500°C and (b) 700°C.

3.3. Incoloy 800H

Incoloy 800H (referred to here as IN800H) is an iron-based alloy, with high concentrations of nickel and chromium. It is being widely considered for use in VHTR internal components due to its high temperature mechanical properties and corrosion resistance. The alloy is code certified for use up to 760°C. However, at elevated temperatures some oxidation, possibly a Cr-Fe oxide or Cr-Fe-Ni spinel oxide formation, is expected to occur in this alloy [9].

Mirror polished samples (Ra = 0.018 µm) of IN800H were tested in air at 500°C and 700°C after exposing the samples for durations up to 5 hours (Figures 46 and 47). For both tests, the emissivity changes are very minimal; the magnitude of the emissivity spectra for each test is similar (0.4-0.55 range) but there are differences in the shape of the spectra. The two spectra are quite close at wavelengths above 6 microns. At 500°C, the emissivity starts about 0.4 at low wavelengths and increases linearly up to 6 microns wavelength; while at 700°C the emissivity starts higher (0.6) at low wavelengths, decreases up to about 4 microns wavelength and stabilizes after that point. This is consistent with temperature dependence for corrosion resistant alloys, where the small increase in oxide thickness has a higher effect at low wavelengths.

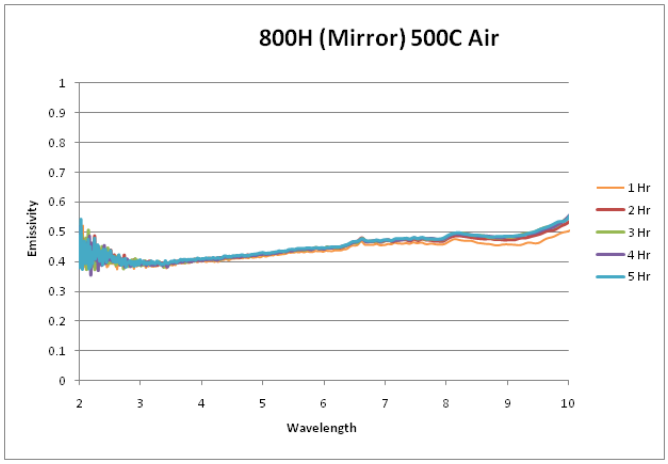

Figure 46. Spectral emissivity of a mirror polished IN800H at 500°C.

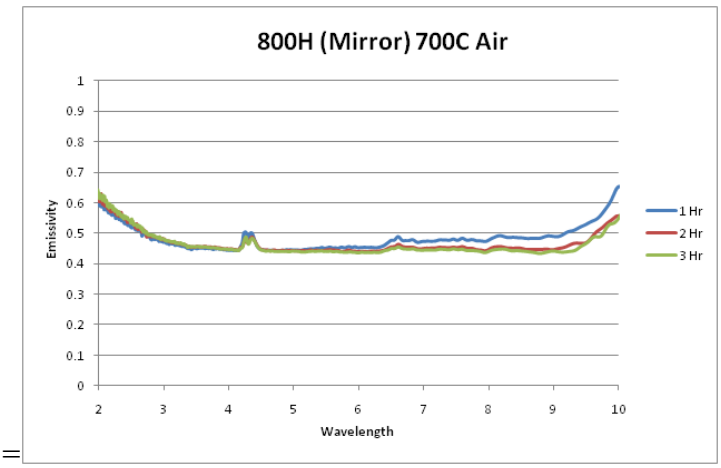

Figure 47. Spectral emissivity of a mirror polished IN800H in air at 700°C.

SEM imaging (Figure 48a) of the IN800H sample at 500°C shows little visible oxidation, however EDS scans (Figure 48b) indicate that the sample surface contains 6% oxygen compared to negligible oxygen before testing. For the samples tested at 700°C, SEM imaging and EDS scans (Figure 49a and 49b) show more visible surface oxidation and an increase in surface oxygen content to 14 %. In addition profilometry was performed on an untested 800H sample, as well as the two tested samples (Figures 50 and 51). The average roughness of the sample at 500°C (Ra = 0.026 μm) was greater than that of a mirror polished sample, and for both, different grains were clearly visible. The sample tested at 700°C had the same average roughness as 500°C tested (Ra = 0.0261 μm), but grains were no longer visible. This is also indicative of the slow oxide growth rate kinetics of IN800H alloy.

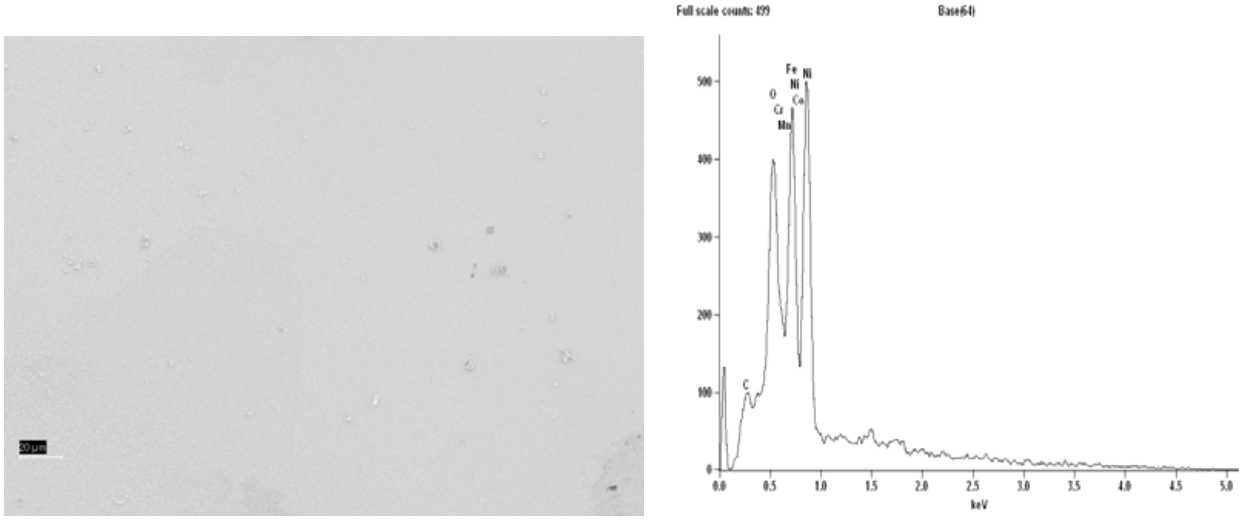

(a) **(b)**

Figure 48. (a) SEM plan view image of IN800H after testing at 500°C and (b) corresponding EDS elemental spectrum.

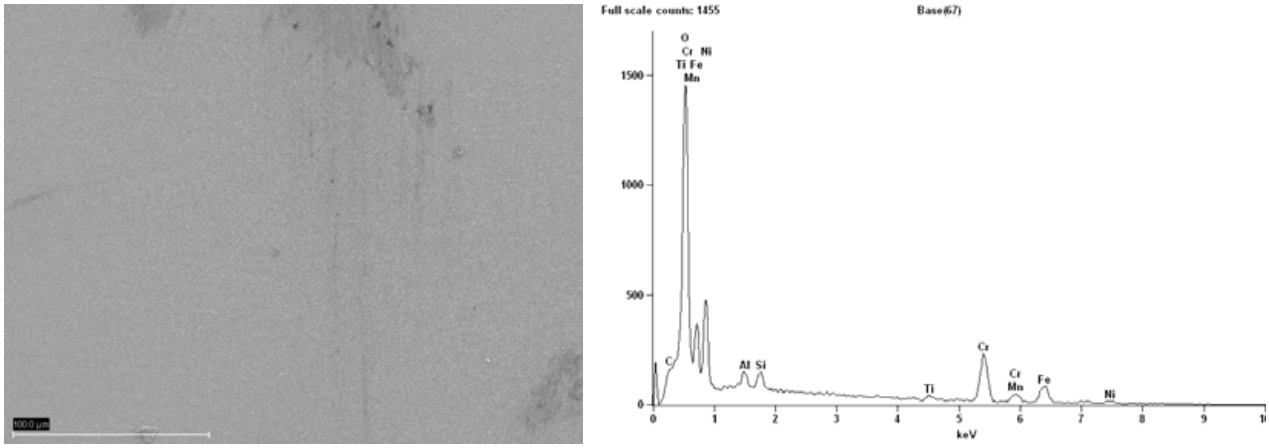

(a) **(b)**

Figure 49. (a) SEM plan view image of IN800H after testing at 700°C and (b) corresponding EDS elemental spectrum.

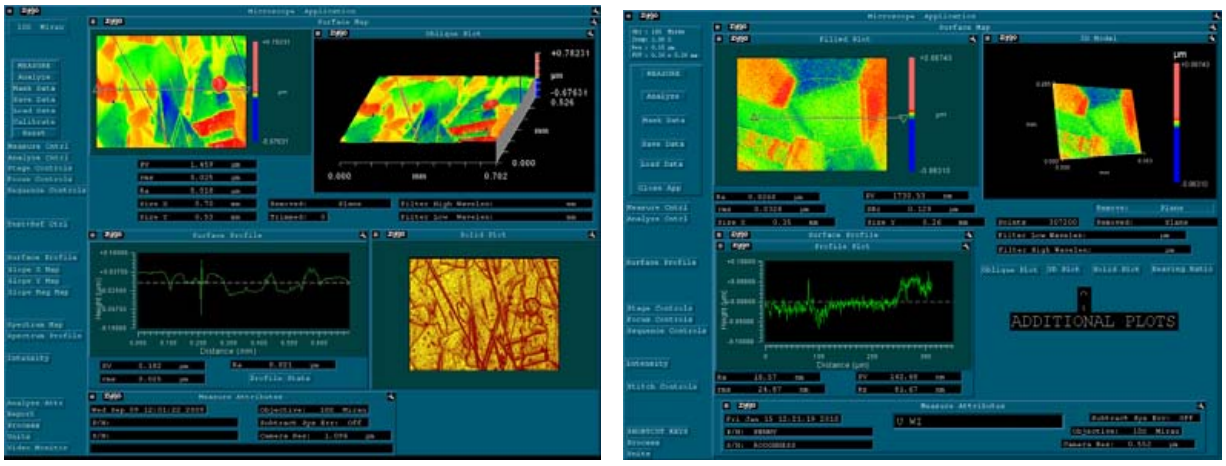

(a) **(b)**

Figure 50. Profilometry of IN800H samples (a) pre-testing and (b) after emissivity testing at 500°C.

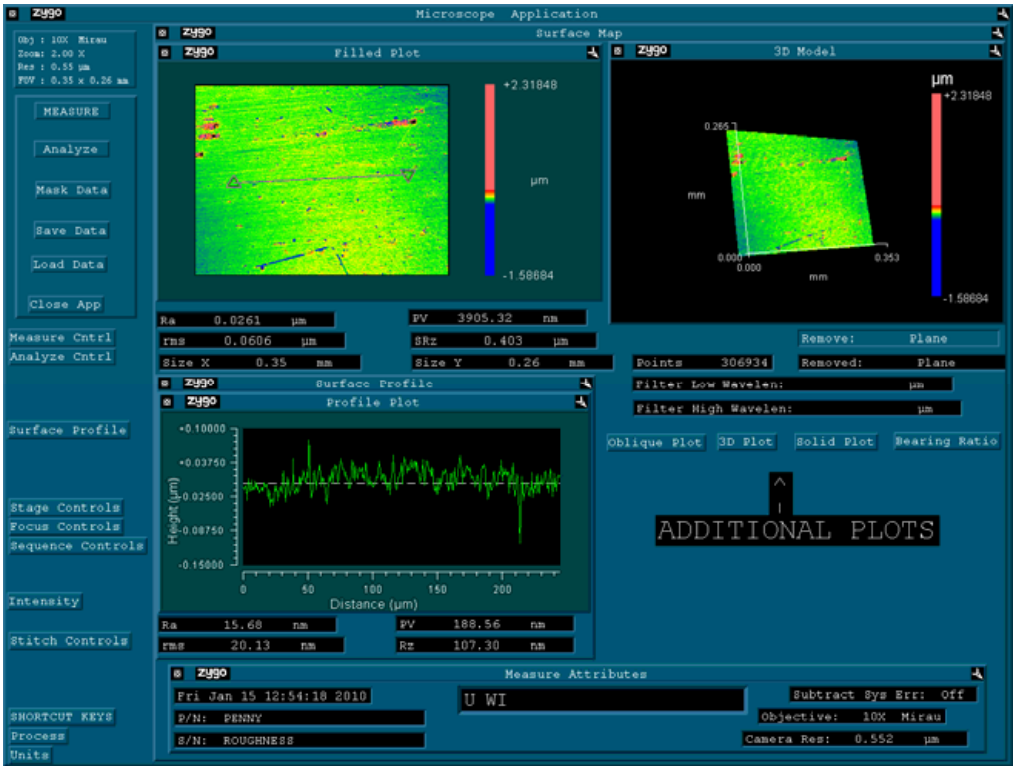

Figure 51. Profilometry of IN800H samples after emissivity testing at 700°C.

3.4. Inconel 617

Inconel 617 (IN 617) is a nickel-based alloy designed for use in high temperature environments. Due to its high chromium content (~20%), it is very corrosion resistant. It is being considered for use in reactor internal components; however the cobalt in this alloy is a concern due to cobalt activation. Since the alloy contains little to no iron any oxide that forms will most likely be a chromium oxide or possibly a chromium-nickel spinel oxide [7].

Spectral emissivity of mirror-polished IN 617 samples (Ra = 0.007 µm) were tested at 500°C and 700°C. The spectral emissivity at 500°C (Figure 52) displays the trends expected of very slightly oxidized materials, with generally low levels of emissivity and large contributions coming from the substrate alloy. The spectrum shows constant emissivity up to about 6 microns wavelength and then decreases linearly as wavelength increases. There is essentially no difference in emissivity with increasing exposure time except minor variations at high wavelengths. The SEM images of the IN 617 after emissivity testing at 500°C were indicative of any significant oxide growth (Figure 53).

At 700°C the emissivity spectrum (Figure 54) is significantly different. The magnitude of the emissivity spectrum is higher than at 500°C, and additionally the shape is different. The spectral emissivity is highest at low wavelengths and begins to decrease immediately as wavelength increases. There is also an increase in emissivity with increasing exposure time at all wavelengths. This shows that an oxide layer is present which continues to grow during testing, but growth is slow due to the oxide forming elements in the alloy such as Cr.

SEM imaging (Figure 55a) of the IN 617 sample after testing at 700°C confirms that some oxidation has occurred. Grain boundaries which were not visible in the pre-test baseline samples

were clearly evident. It appears that some grains have been preferentially oxidized while others remain unoxidized. EDS scans (Figure 55c) indicated an oxygen content of 8%. Cross-sectional SEM imaging (Figure 55b) showed that an oxide layer about 1μm had developed on the surface. Furthermore two types of oxide layers were observed in this oxide layer, most likely a chromium-oxide and a Ni-Cr spinel layer. It appears that the first oxide layer grew uniformly on the surface, while the outer layer either grew preferentially on certain grains. This is not unexpected, as studies have shown that the crystalline orientation of certain grains can cause preferential growth [42].

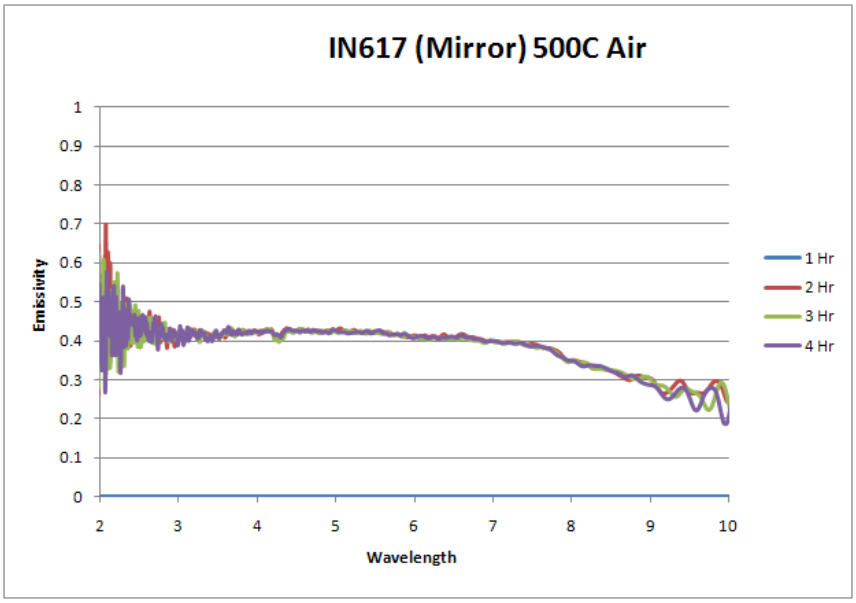

Figure 52. Spectral emissivity of IN 617 alloy at 500°C.

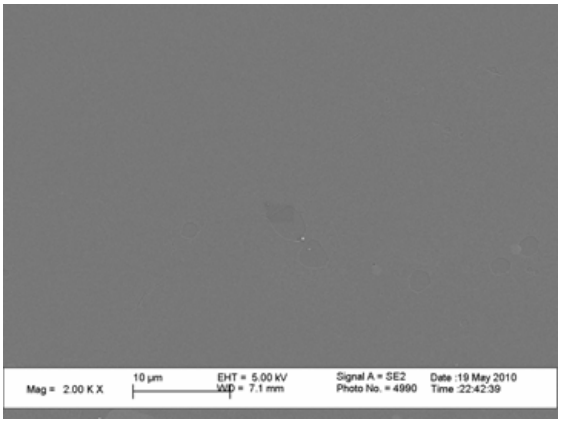

Figure 53. SEM plan view image of IN 617 after emissivity testing at 500°C.

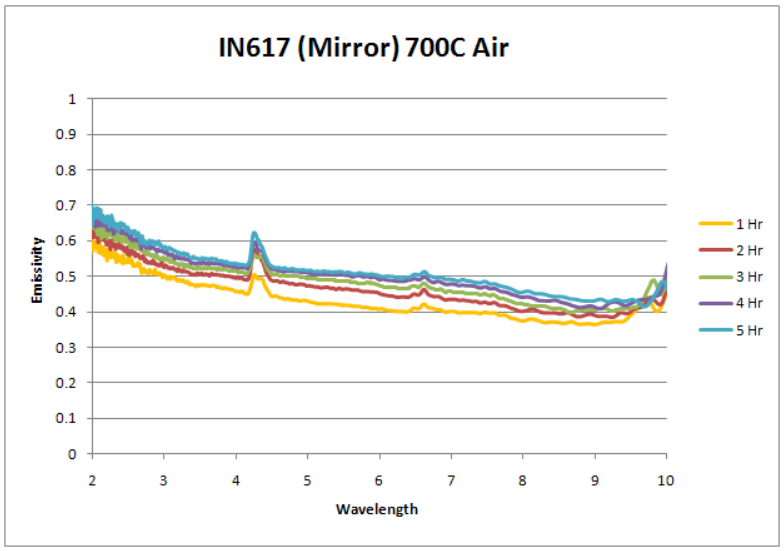

Figure 54. Spectral emissivity of IN 617 alloy at 700°C.

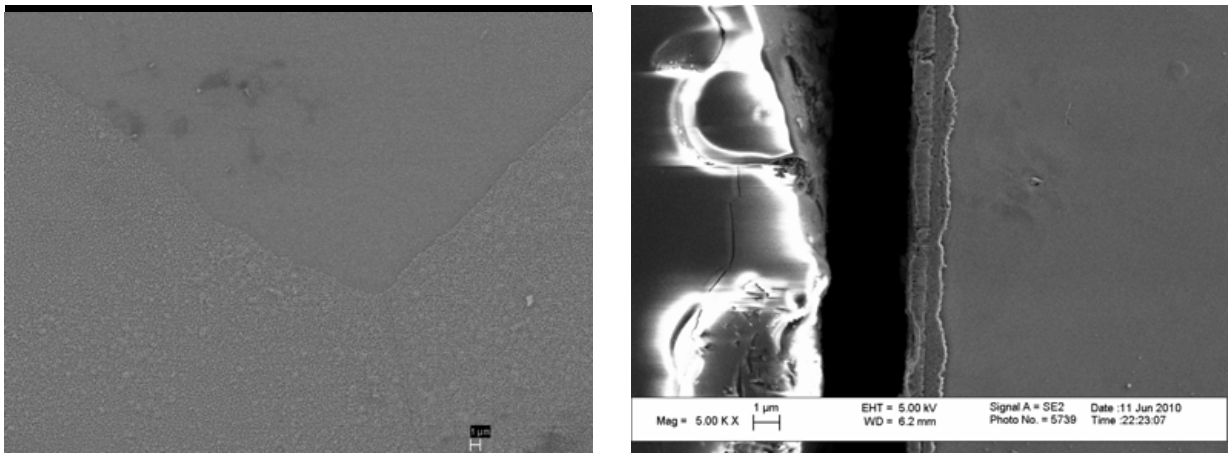

(a) **(b)**

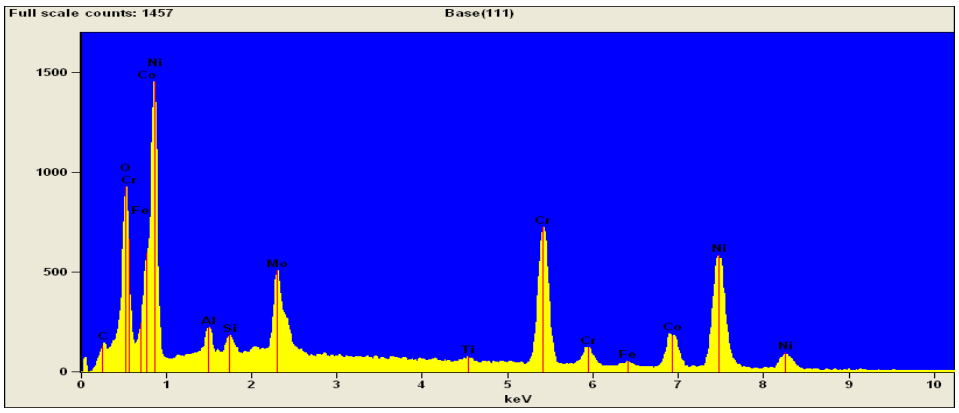

(c)

Figure 55. SEM and EDS analysis of IN 617 after emissivity testing at 700°C (a) plan view (b) cross section image (c) corresponding elemental EDS spectrum taken in the plan view image.

3.5. Haynes 230

Haynes 230 is another high temperature, highly alloyed, nickel-based alloy. Along with IN800H and IN 617, it is being considered for use in VHTR internal components. It has less cobalt than IN 617, so activation of the material is less of a concern, but still a possibility. It is a desirable alloy because of its high oxidation and creep resistance. Due to the high chromium content (~20%) and low iron content, the oxide that forms at higher temperatures is expected to be a relatively thin protective nickel-chromium oxide [28].

Spectral emissivity of mirror-polished samples of alloy Haynes 230 (Ra = 0.006 μm) were tested at 350°C, 500°C, and 700°C. The spectral emissivity of the sample at 350°C (Figure 56) shows the trends expected for a slightly oxidized material. The emissivity is level at 0.4 at low to medium wavelengths and declines sharply at high wavelengths. There are no changes in emissivity with increasing exposure time, again showing little to no oxide growth during testing. This emissivity recorded is very similar to that found in an earlier study on the spectral emissivity of Haynes 230 at 417°C [28].

SEM plan view images (Figure 57a) of Haynes 230 after testing at 350°C showed what appeared to be brush marks of sorts. These are not indicative of oxidation, and are instead most likely a residue from the polishing procedure. The corresponding EDS spectrum (Figure 57b) showed no detectable oxygen on the surface, indicating very little surface oxidation. Profilometry of the Haynes 230 samples before and after testing at 350°C (Figure 58) showed no significant difference in surface topography consistent with the observation that little or no oxidation occurred during testing at 350°C.

The spectral emissivity of the Haynes 230 at 500°C (Figure 59) was practically constant over the entire range of wavelengths tested, maintaining a value within the 0.4-0.5. The slight increase in emissivity at higher wavelengths compared to the samples tested at 350°C shows that some oxidation has occurred at 500°C. The similarity between the two spectra is in agreement with the idea of a protective chromium oxide which does not increase significantly in thickness, even with increasing temperature.

SEM images of the Haynes 230 sample tested at 500°C (Figure 60a) visually appear identical to the untested mirror polished sample, however the corresponding EDS spectrum (Figure 60b) showed 2.01%, oxygen at the surface indicating that there was at least slight oxidation. The post-testing profilometry (Figure 61) also showed evidence of oxidation, as the surface roughness (Ra = 0.0101 μm) was almost twice as high as the untested samples.

Figure 62 shows spectral emissivity measurements of alloy Haynes 230 at 700°C. The spectral emissivity was very similar to that observed in the 500°C tests (Figure 59). The similarity between the two spectra is in agreement with the idea of a protective chromium oxide which does not increase significantly in thickness, even with increasing temperature.

SEM plan view images of the Haynes 230 (Figure 63a) after emissivity testing at 700°C clearly showed grain boundaries indicating preferential oxidation attack of the microstructure. The EDS spectrum (Figure 63b) confirmed greater oxidation, as surface oxygen content was 5.69%. Additionally, post-testing profilometry (Figure 64) also visibly showed grain boundaries, and the average roughness (Ra = 0.1134 μm) which was about ten times greater than for the samples tested at 500°C. However, as the emissivity spectra prove, these oxidation effects did not lead to any significant change in spectral emissivity.

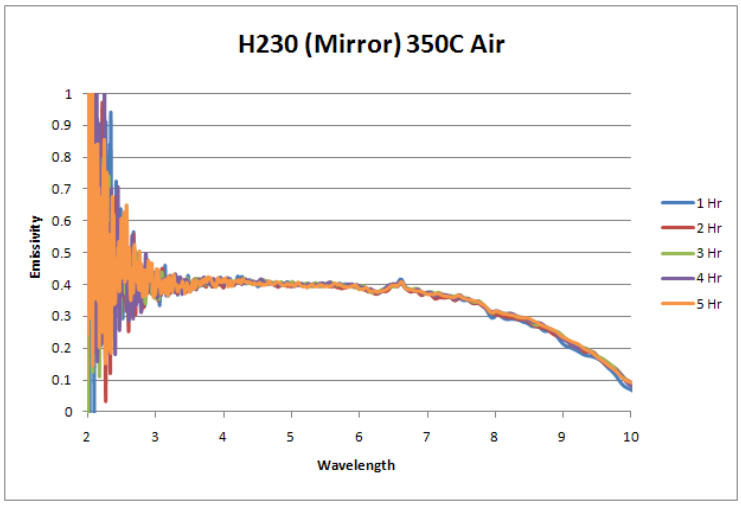

Figure 56. Spectral emissivity of a Haynes 230 alloy at 350°C.

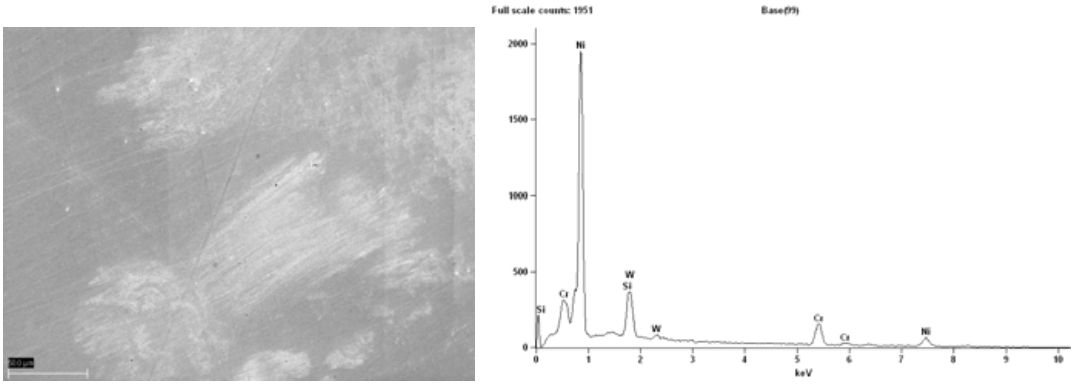

(a) **(b)**

Figure 57. (a) Plan view SEM image of a post-test Haynes 230 sample after testing at 350°C with (b) corresponding EDS spectrum.

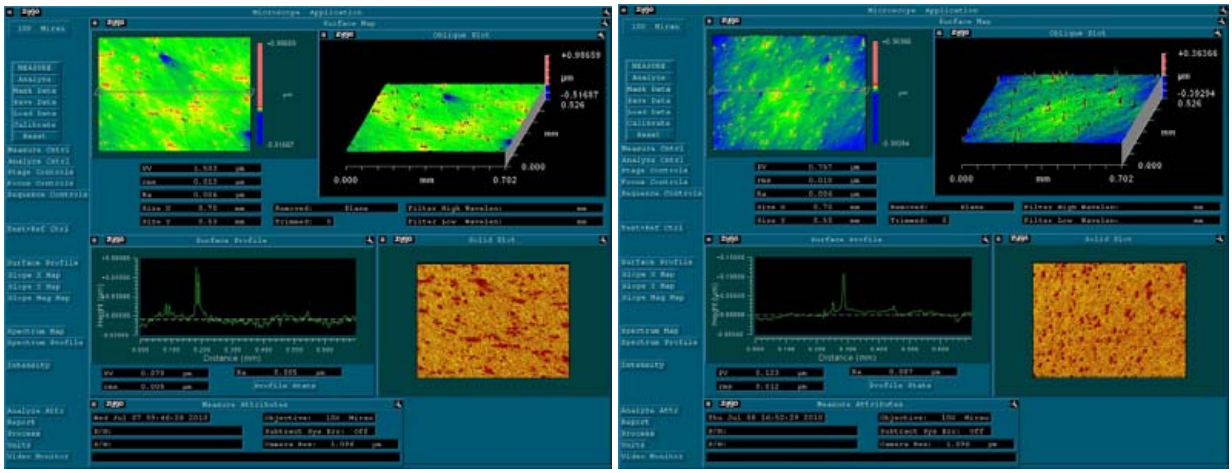

(a) **(b)**

Figure 58. Profilometery of the surface of the Haynes 230 sample with (a) before testing and (d) after emissivity testing at 350°C.

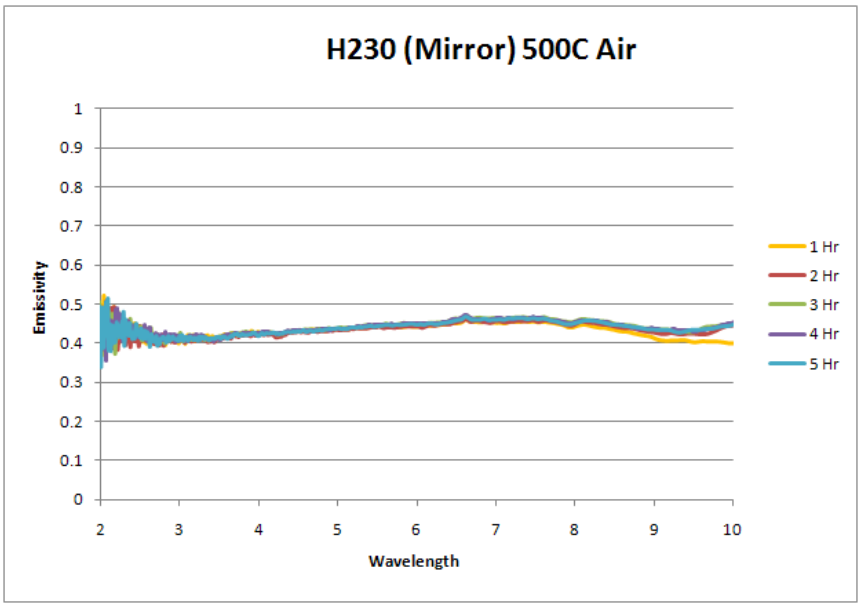

Figure 59. Spectral emissivity of a Haynes 230 alloy at 500°C.

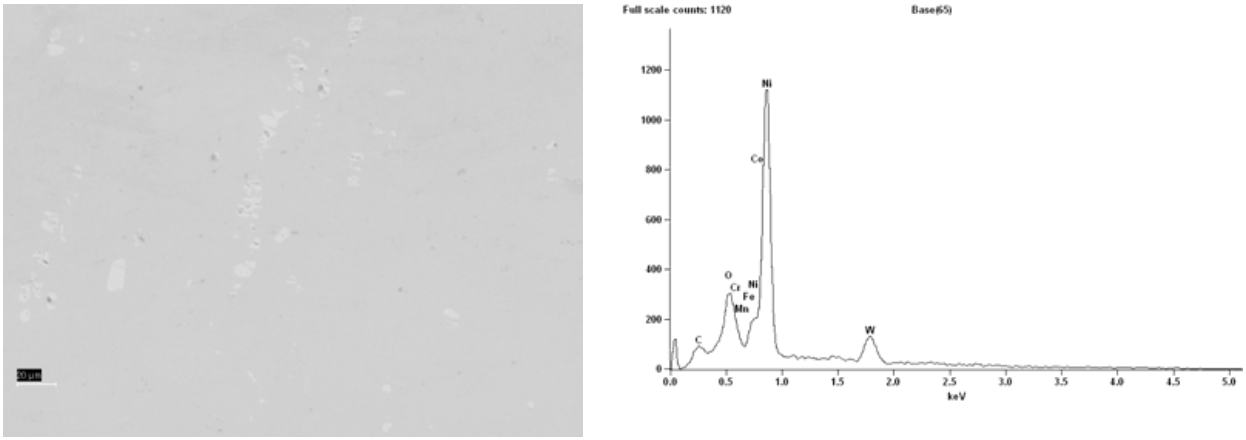

(a) **(b)**

Figure 60. (a) Plan view SEM image of a post-test Haynes 230 sample after testing at 500°C with (b) corresponding EDS spectrum.

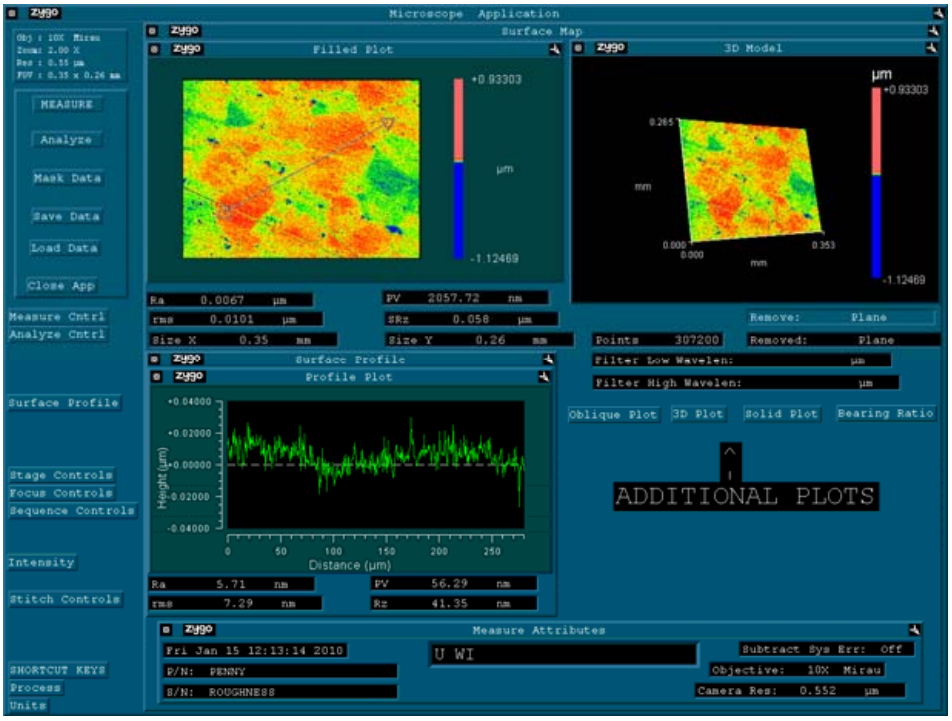

Figure 61. Profilometery of the surface of the Haynes 230 sample with (a) before testing and (d) after emissivity testing at 500°C.

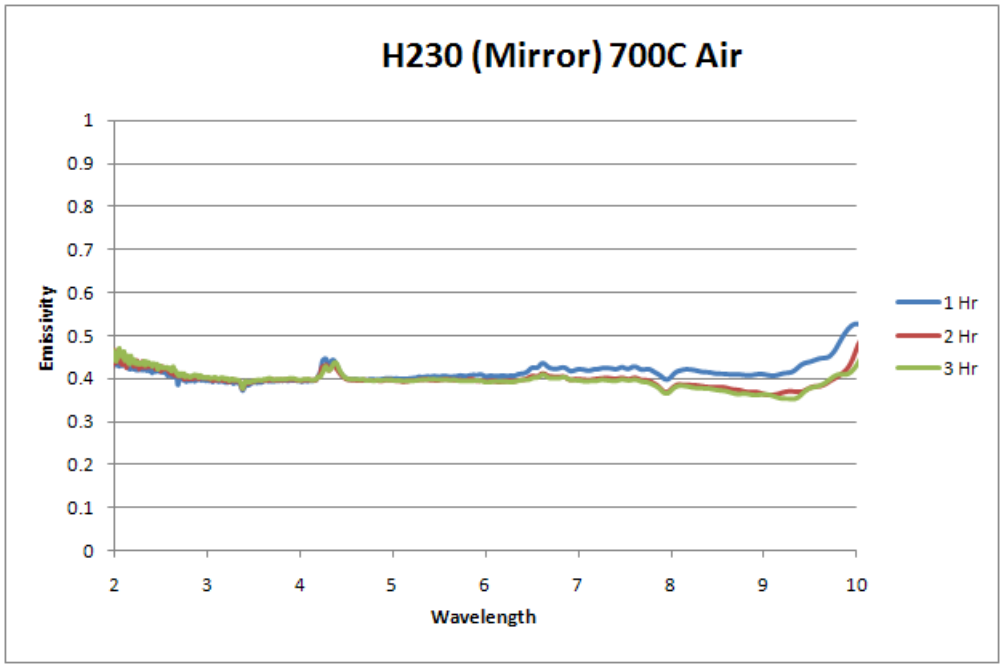

Figure 62. Spectral emissivity of a Haynes 230 alloy at 700°C.

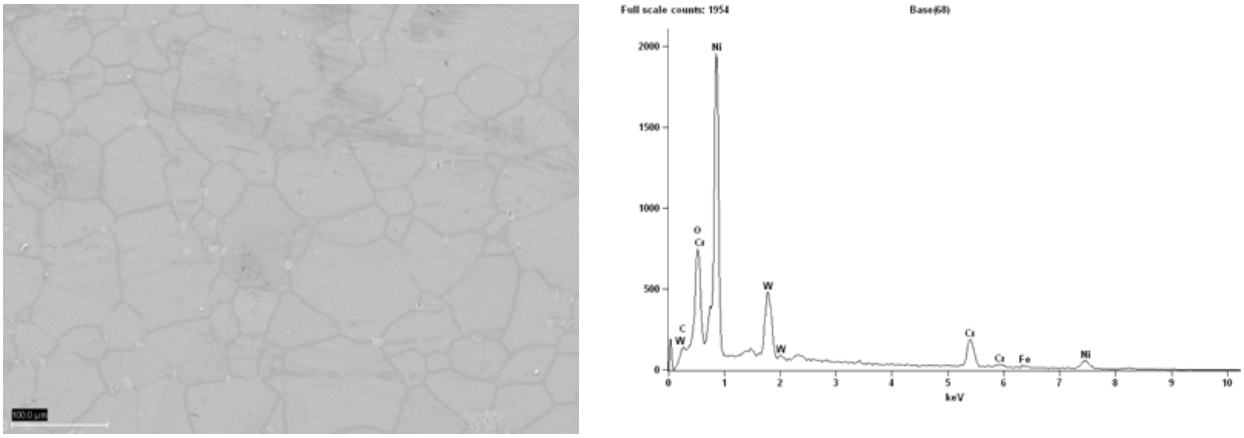

(a) **(b)**

Figure 63. (a) Plan view SEM image of a post-test Haynes 230 sample after testing at 700°C with (b) corresponding EDS spectrum.

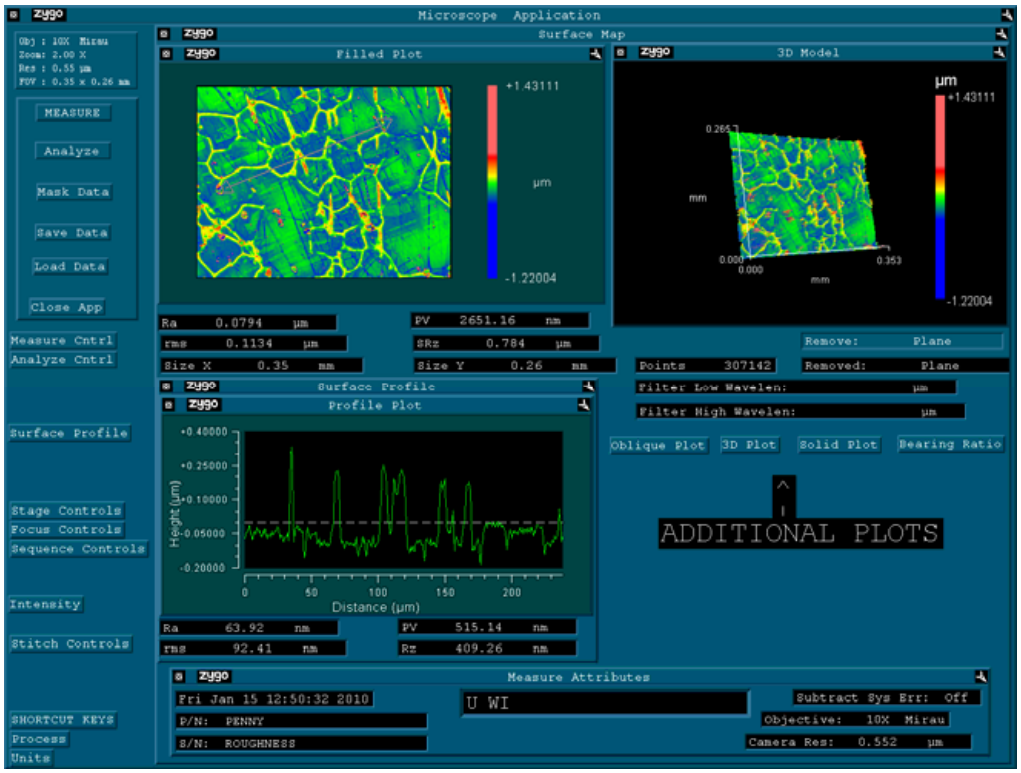

Figure 64. Profilometry of Haynes 230 alloy samples after testing at 700°C.

3.6. T22 and T91 Ferritic Steels

Figure 65 shows the spectral emissivities for T22 and T91 ferritic steels at 500°C, for exposures of 1 to 5 hours, in air. T22 which contains about 2.5%Cr and T91 which contains about 9%Cr represent intermediate cases between SA508 and 316 stainless steel in regards to Cr content. In both these cases, the emissivities change with exposure times between 1 and 5 hours. In the case of T22 steel a rather unique trend in emissivity values. In the case of T91 steel the

emissivity values increase with exposure time which clearly stems from the steady growth of the oxide layer over this time period. Even then the emissivity levels are lower than that of a magnetite/spinel oxide, implying that the underlying metallic substrate is still contributing to the overall emissivity, although its contribution decreases with the increasing thickness of the oxide layer. Unlike T22 steel, no spallation is observed in T91 steel because of its higher Cr content. Figure 66 shows the emissivities for T22 and T91 ferritic steels at 700°C. Here, the high emissivity indicates that the oxide thickness is high enough to almost entirely preclude substrate effects. For T22, although spallation occurs, the spalled region quickly reoxidizes at this higher temperature. Figure 67 and 68 show the SEM image and corresponding EDS elemental spectra for T22 and T91 ferritic steels, respectively, after emissivity tests at 500°C.

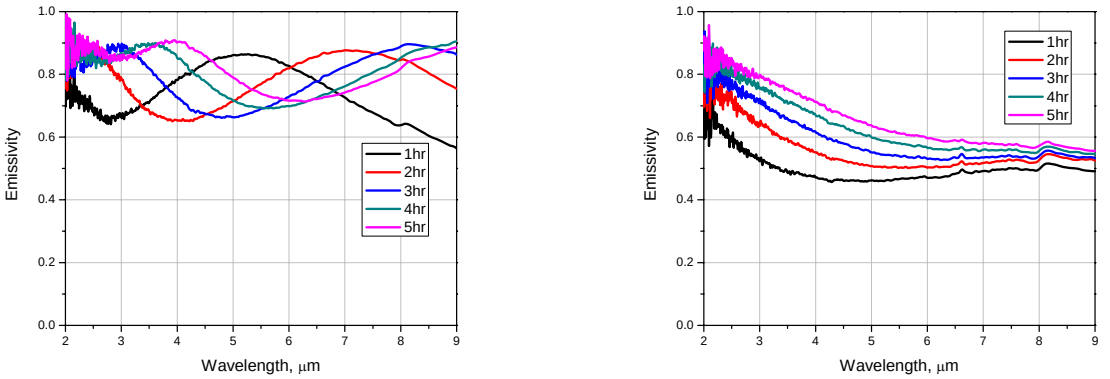

(a) **(b)**

Figure 65. Spectral emissivity data taken at 500°C for (a) T22 ferritic steel and (b) T91 ferritic steel.

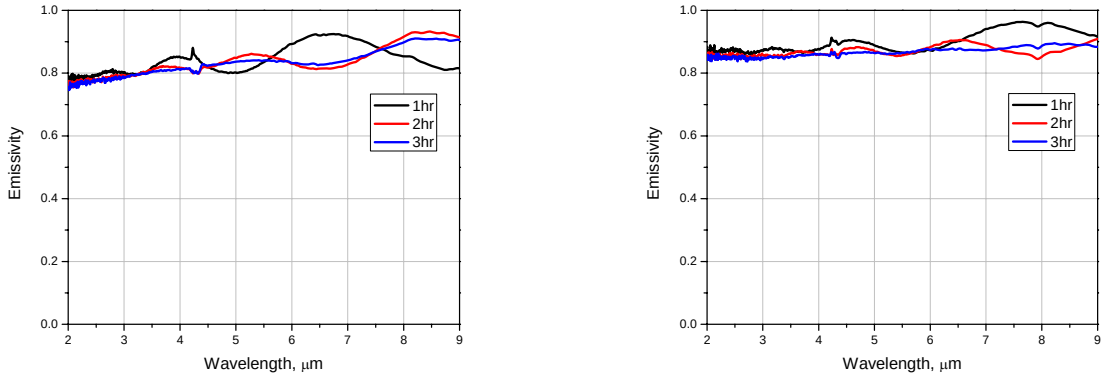

(a) **(b)**

Figure 66. Spectral emissivity data taken at 700°C (a) T22 ferritic steel and (b) T91 ferritic steel.

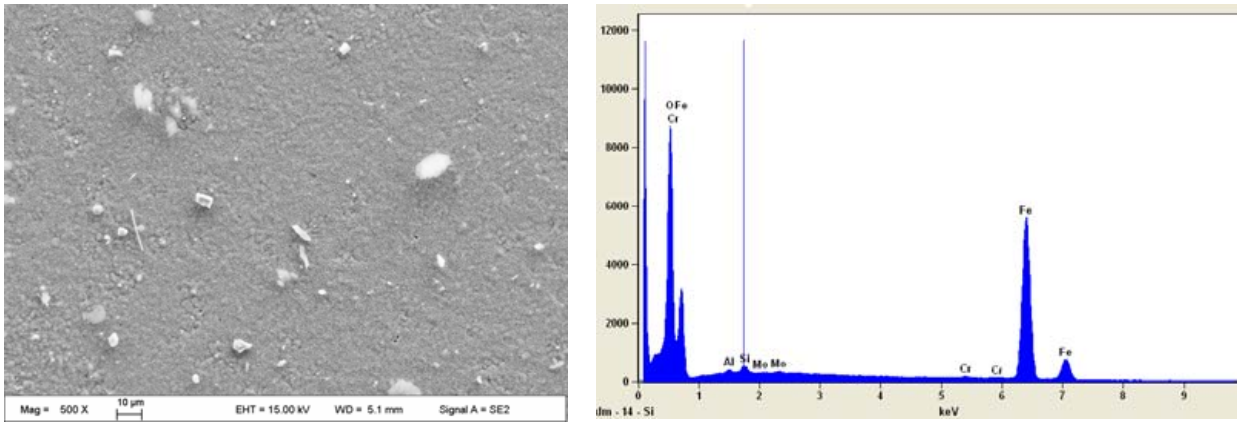

(a) **(b)**

Figure 67. (a) SEM surfaceimage of T22 ferritic steel after emissivity tests at 500°C, (b) corresponding EDS elemental EDS spectrum.

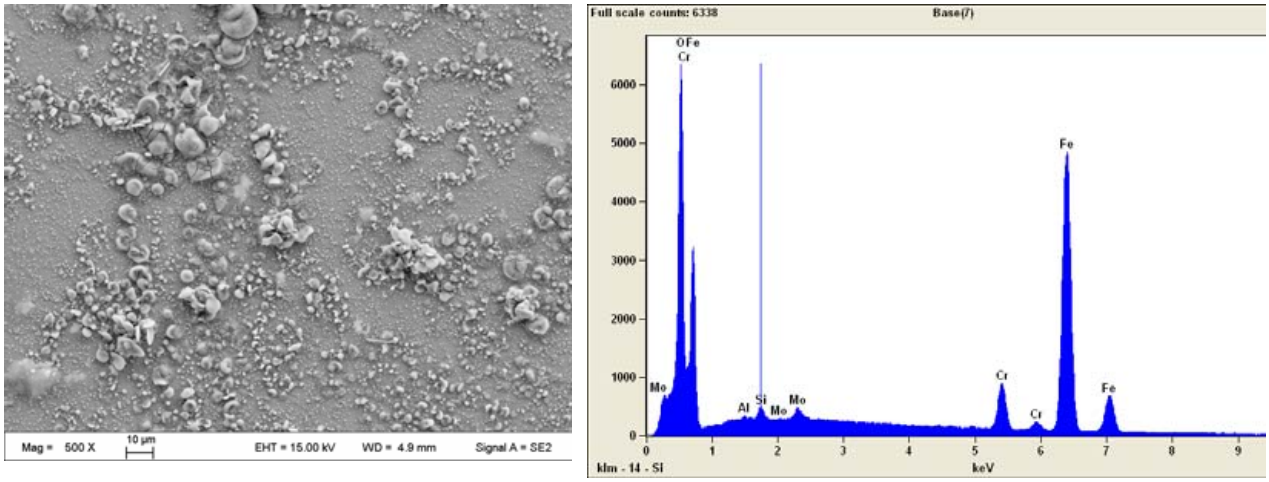

(a) **(b)**

Figure 68. (a) SEM surface image of T91 ferritic steel after emissivity tests at 500°C, (b) corresponding EDS elemental EDS spectrum.

3.7. 316 and 304 Stainless Steels

A comparison of the spectral emissivities of two widely used stainless steels, namely 304 and 316, at 700°C is shown in Fig. 69. Figure 70 shows the cross-sectional SEM images on 316 and 304 stainless steel that reveals the thickness of the oxide layer that develops on the two stainless steels after 700°C emissivity tests. The marginally higher thickness of the oxide layer may be responsible for the slightly higher emissivity observed for the 316 stainless steel compared to the 304 stainless steel.

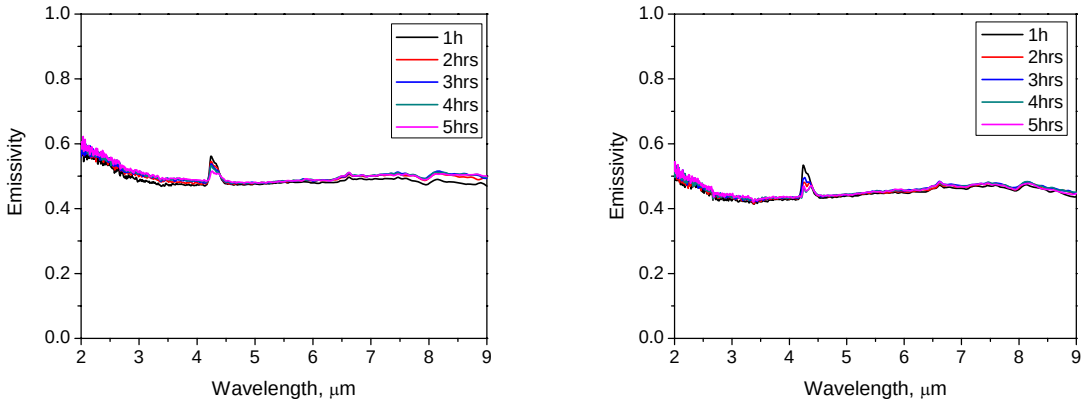

Figure 69. Spectral emissivity measurements at 700°C for (a) 316 stainless steel and (b) 304 stainless steel.

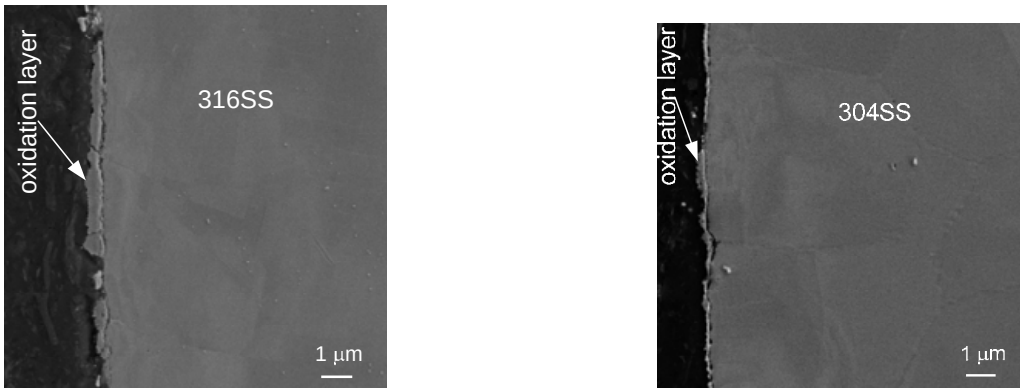

Figure 70. SEM cross-sectional images showing the oxide layer thickness after the 700°C emissivity tests for (a) 316 stainless steel and (b) 304 steel stainless steel.

3.8. Summary of Emissivity of Candidate Materials in Mirror-Polished Condition

To calculate integrated average emissivity of various materials tested thus far in their mirror-polished condition, the program MATLAB was used to perform a mathematical integration of data. MATLAB used a code written for this particular project that accepted a file containing two columns of data. One column contained the values of wavelength, and the other column

contained the emissivity values of each material, both outputs coming from the FTIR used in this experiment. The wavelength data across which analysis is desired must be manually extracted with the corresponding emissivity data and saved into a file. The program then integrates the curve data using a modified version of a middle Riemann's sum method to calculate the area under the emissivity curve. This used the principal of creating columns, based on a width of the difference between two wavelength points, and multiplying this by the emissivity value at that point, and then summing the total area found from these columns. The number of columns summed was the intrinsic wavelength interval between data points collected by the FTIR. This area was then divided by the wavelength range in question, in order to obtain an average height, or emissivity for the sample. From the examination of spectral emissivity data gathered thus far, it was decided that integrated emissivity 4 to 10μm wavelength range would provide the most reasonable assessment of the overall emissivity of a material. Figure 71 shows the integrated emissivties of various VHTR candidate materials at 350°C, 500°C, and 700°C in the 4 to 10μm wavelength range.

It is clear that in almost all materials emissivity increases with test temperature. At temperatures above 500°C, the emissivity of ferritic steels increases quite rapidly, in contrast with the austenitic alloys where the integrated emissivity remains below 0.5 even at 700°C. At 350°C, emissivity of all materials tested remains below a value of 0.5.

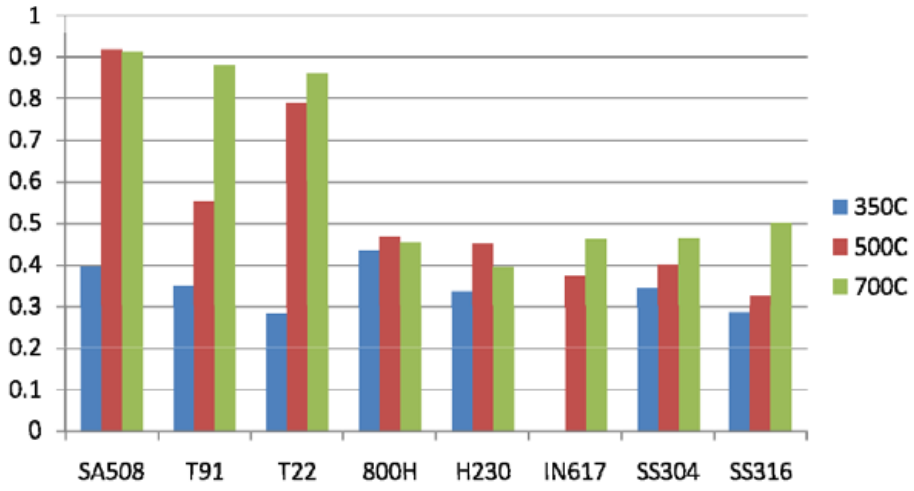

Figure 71. Intergated emissivities of various VHTR candidate materials in mirror-polished condition at 350°C, 500°C, and 700°C in the 4 to 10μm wavelength range.

4. Effect of Surface Roughness on Emissivity

The effect of surface roughness on spectral emissivity was examined by grinding the surface of the samples with various grits of silicon carbide grit paper.

Figure 72 shows the spectral emissivity at 350°C of T91 ferrtic steel ground to various levels of roughness (120 grit, 400 grit, and 1200grit). The results of these measurements indicate that surface roughness does not have a significant effect on spectral emissivity of T91 steel at 350°C.

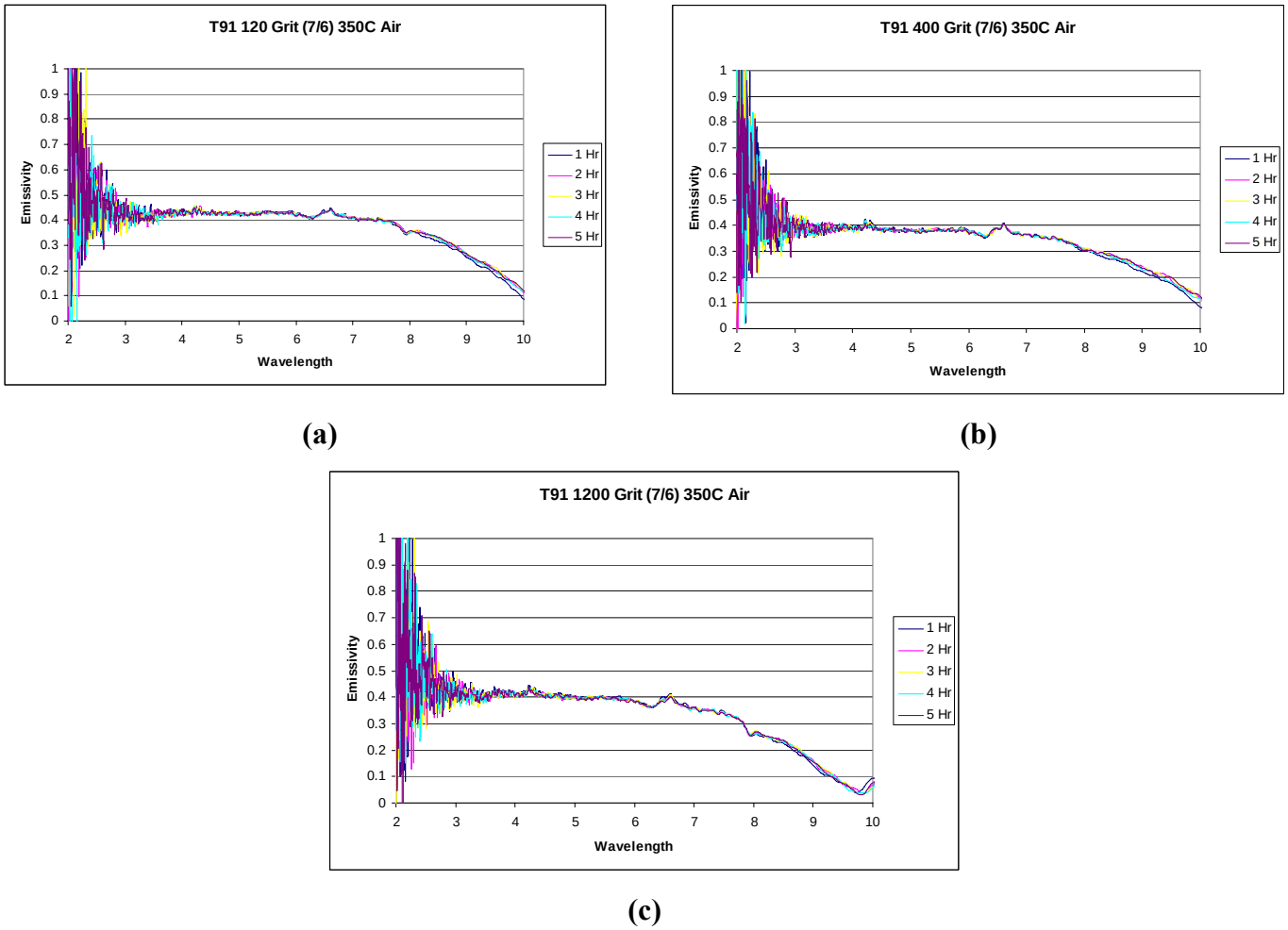

Figure 72. Spectral emissivity measurements of T91 ferritic steel at 350°C for three levels of surface finish, (a) 120 grit, (b) 400 grit, and (c) 1200 grit surface finish.

Figure 73 shows the spectral emissivity measurements for SA 508 steel (a popular RPV material) at 500°C and 700°C for mirror-like surface finish and 320 grit surface finish. As can be seen, increase in surface roughness increases emissivity values and higher temperature in general lead to an increase in emissivity due to the increased thickness of the oxide layer. The effect of surface roughness on emissivity is less pronounced at higher temperatures because of the overwhelming effects of increased oxidation.

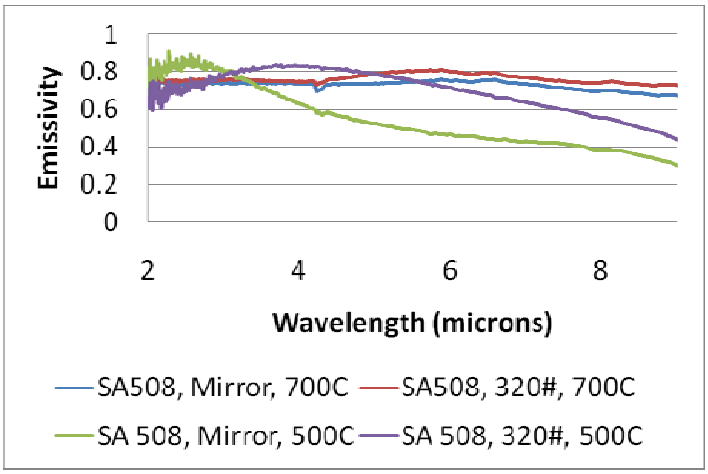

Figure 73. Experimentally determined spectral emissivity data for SA 508 at 500°C and 700°C for mirror-like surface finish and 320 grit surface finish.

Figure 74 shows the spectral emissivity data for T91 ferritic steel at 500°C and 700°C in mirror-like surface finish and 320 grit surface finish. Here again, increase in surface roughness is noted to increase in emissivity and the emissivity is higher at 700°C than at 500°C due to the higher thickness of the oxide layer. Likewise, the effect of surface roughness on emissivity is less pronounced at higher temperatures because of the overwhelming effects of the oxide layer. The increase in emissivity due to oxidation is less pronounced for T91 than SA508 because of the thinner oxide layer for T91 (due to its higher Cr content).

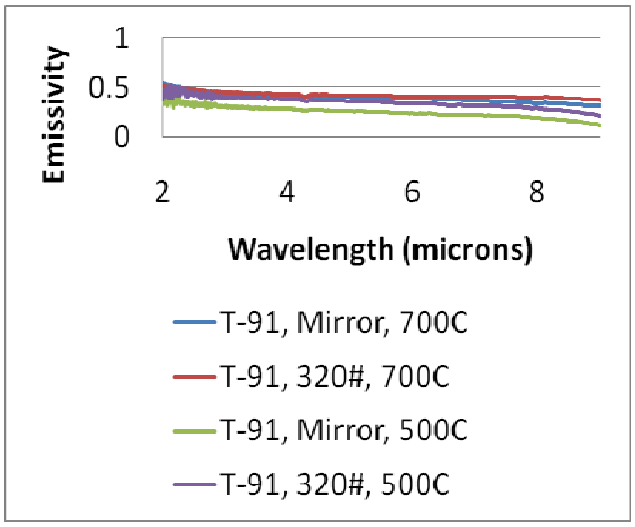

Figure 74. Experimentally determined spectral emissivity data for T91 ferritic steel at 500°C and 700°C for mirror-like surface finish and 320 grit surface finish.

Figure 75 shows the spectral emissivity data for 304 and 316 stainless steels at 500°C and 700°C in mirror-like surface finish and 320 grit surface finish. The effect of surface roughness is similar to observations made for SA 508 and T91 steels, in that emissivity increases slightly with roughness. The effect of temperature is not as pronounced for the stainless steels because of the formation of a very thin tenacious oxide layer on the surface that is kinetically resistant to growth.

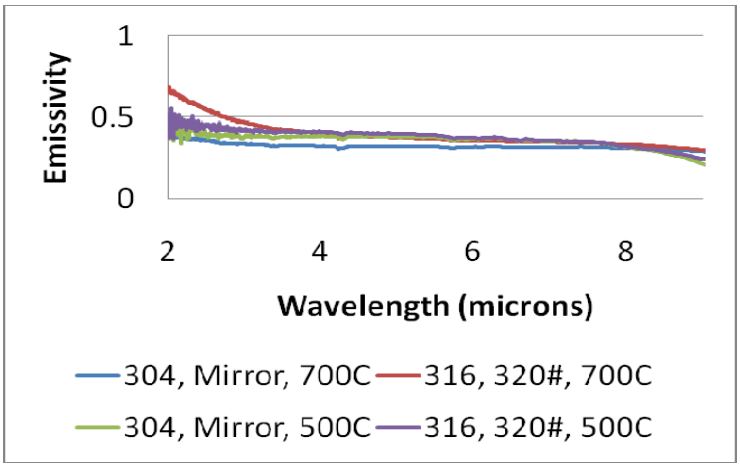

Figure 75. Experimentally determined spectral emissivity data for stainless steels 304 and 316 at 500°C and 700°C for mirror-like surface finish and 320 grit surface finish.

The emissivity data for T22 ferritic steel (2.5%Cr) presented in Figure 76 shows general trends similar to other steels discussed earlier, however some variability was observed emissivity data for various tests and test conditions. An observation of the surface of the T22 samples after the emissivity tests showed visible non-uniformity in the surface oxide coloration due to spallation and in some regions the metallic luster of the base steel was being revealed. Since the spot size from which the emissivity data is derived is about 0.25" in diameter, the variability in emissivity data is speculated to occur due to the averaging effects of oxide layers of various thicknesses (and in some regions the base alloy). Figure 77 shows the SEM images of the surface of T22 ferritic steel in the as ground condition (320 grit surface finish) and after emissivity measurements at 700°C showing oxide lay and its spallation in certain regions.

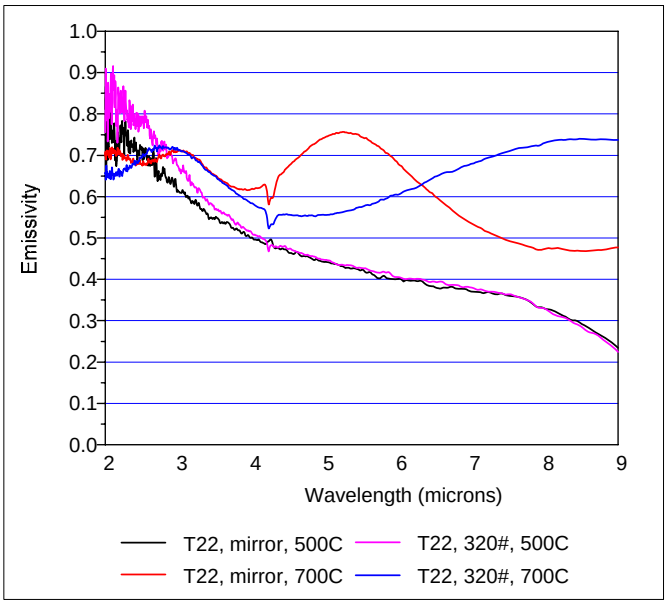

Figure 76. Experimentally determined spectral emissivity data for T22 ferritic steel two levels of temperatures and surface roughnessess. The larger variations in data for T22 were caused by spallation of oxide layer in certain regions.

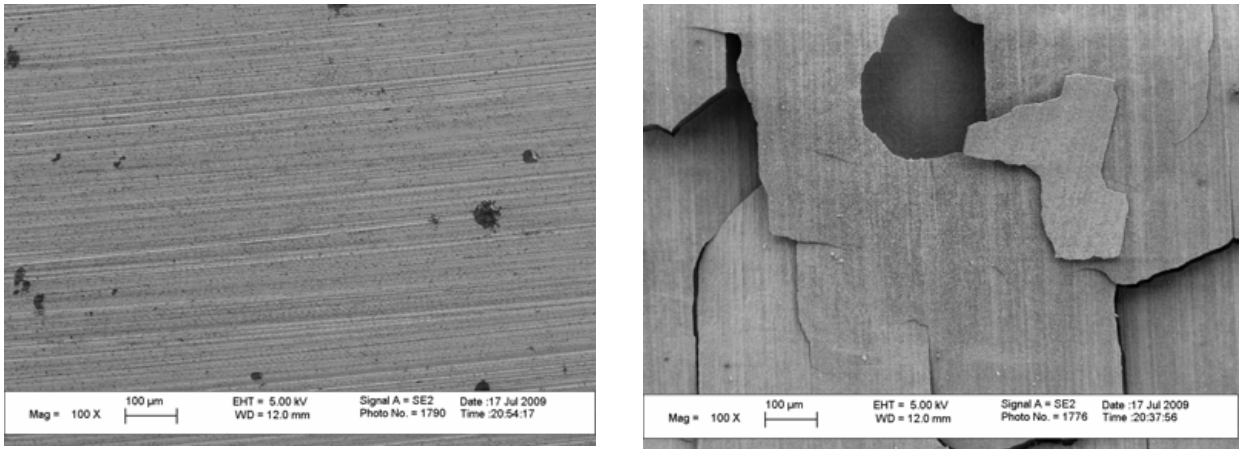

(a) **(b)**

Figure 77. SEM surface images of T22 ferrtic steel (a) 320 grit surface finish and (b) 320 grit surface finish after emissivity experiments at 700^{o}C.

Spectral emissivity measurements were also made for graphite samples procured specifically for this research from Oak Ridge National Laboratory. Figures 78 show the spectral emissivity measurements for graphite for three different surface roughness values corresponding to 400 (Ra=0.694µm), 600 (Ra=0.432µm), and 800 (Ra=0.102µm) grit, respectively, performed at 500^{o}C, in air. As expected, the emissivity of graphite is generally quite high. For all three surface roughness values, the emissivity is generally independent of exposure time. For 400 and 600 grit surface roughness values, the emissivities are quite high, close to 0.9. However, for surface roughness corresponding to 800 grit, the emissivity drops quite clearly. The surface roughness of the graphite samples also does not change significantly after the 500^{o}C tests in air (Figure 79).

However, at 700^{o}C the effect of surface roughness is insignificant (Figures 80). An examination of the sample surfaces after the 700^{o}C exposure showed profuse oxidation (conversion of carbon to carbon dioxide and corresponding mass loss) of the samples (Figure 81). Consequently, the surface roughened significantly and was beyond the resolution limits of the laser profilometer.

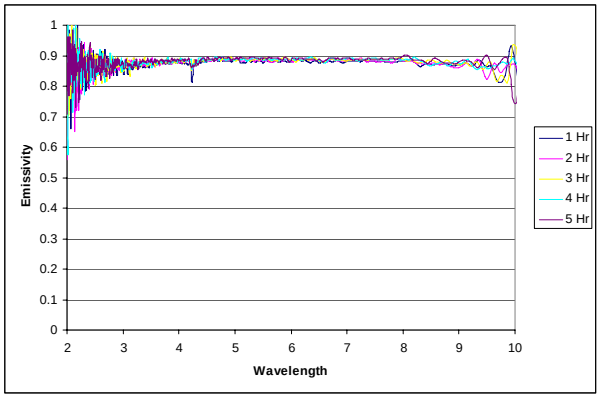

(a)

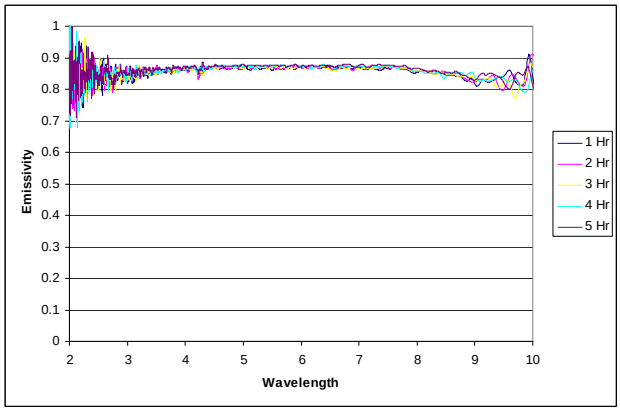

(b)

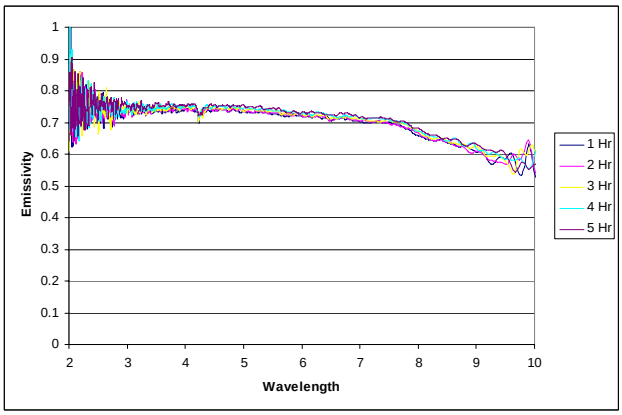

(c)

Figure 78. Spectral emmisivity of graphite at 500°C for exposure durations of 1 to 5 hrs, in air for (a) 400 grit surface finish (Ra=0.694μm), (b) 600 grit surface finish (Ra=0.432μm), and 800 grit surface finish (Ra=0.102μm).

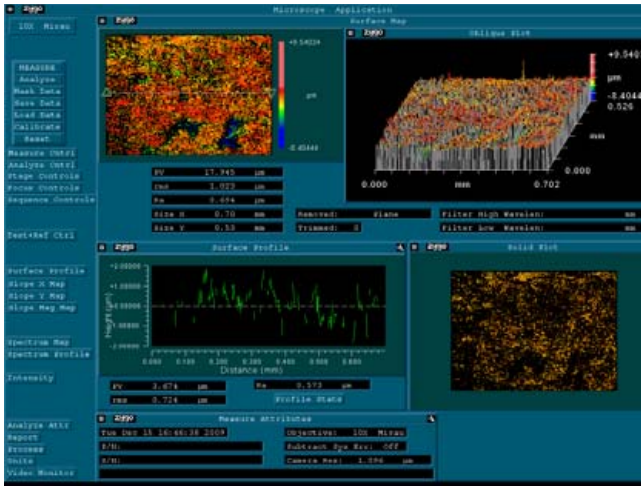

Graphite 400 grit, as-polished, Ra=0.694µm

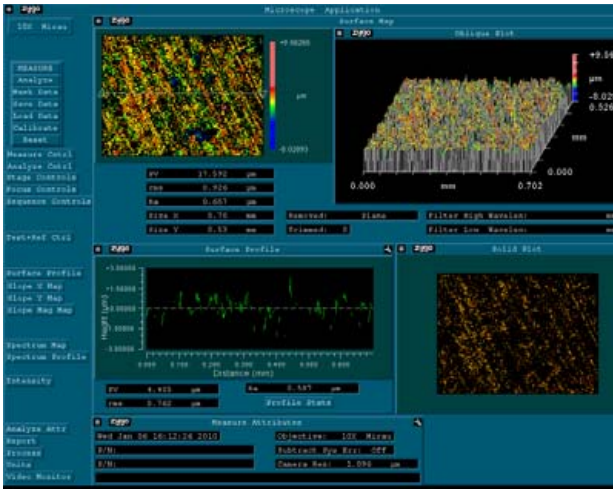

Graphite 400 grit, after 500°C test, Ra=0.657µm

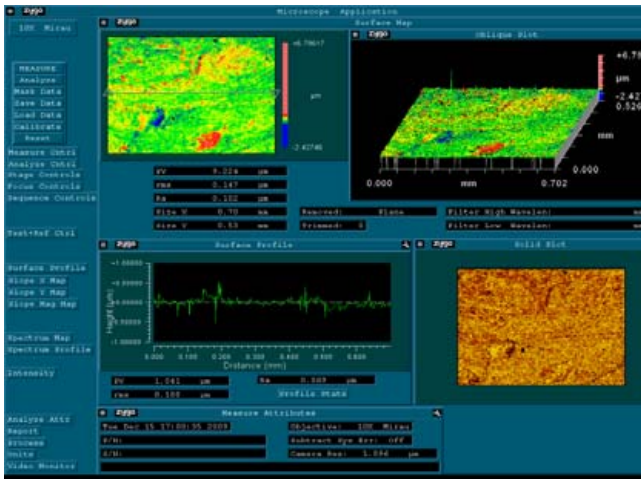

Graphite 800 grit, as-polished, Ra=0.102µm

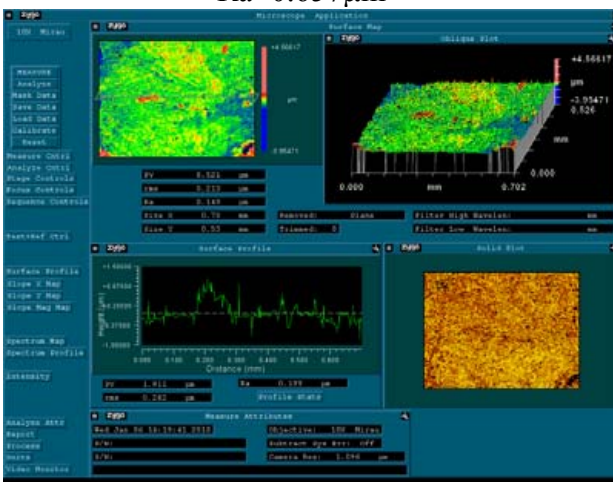

Graphite 800 grit, after 500°C test, Ra=0.149µm

Figure 79. Surface profilometry of graphite samples polished to 400 grit and 800 grit surface finish, before and after tests at 500°C, in air.

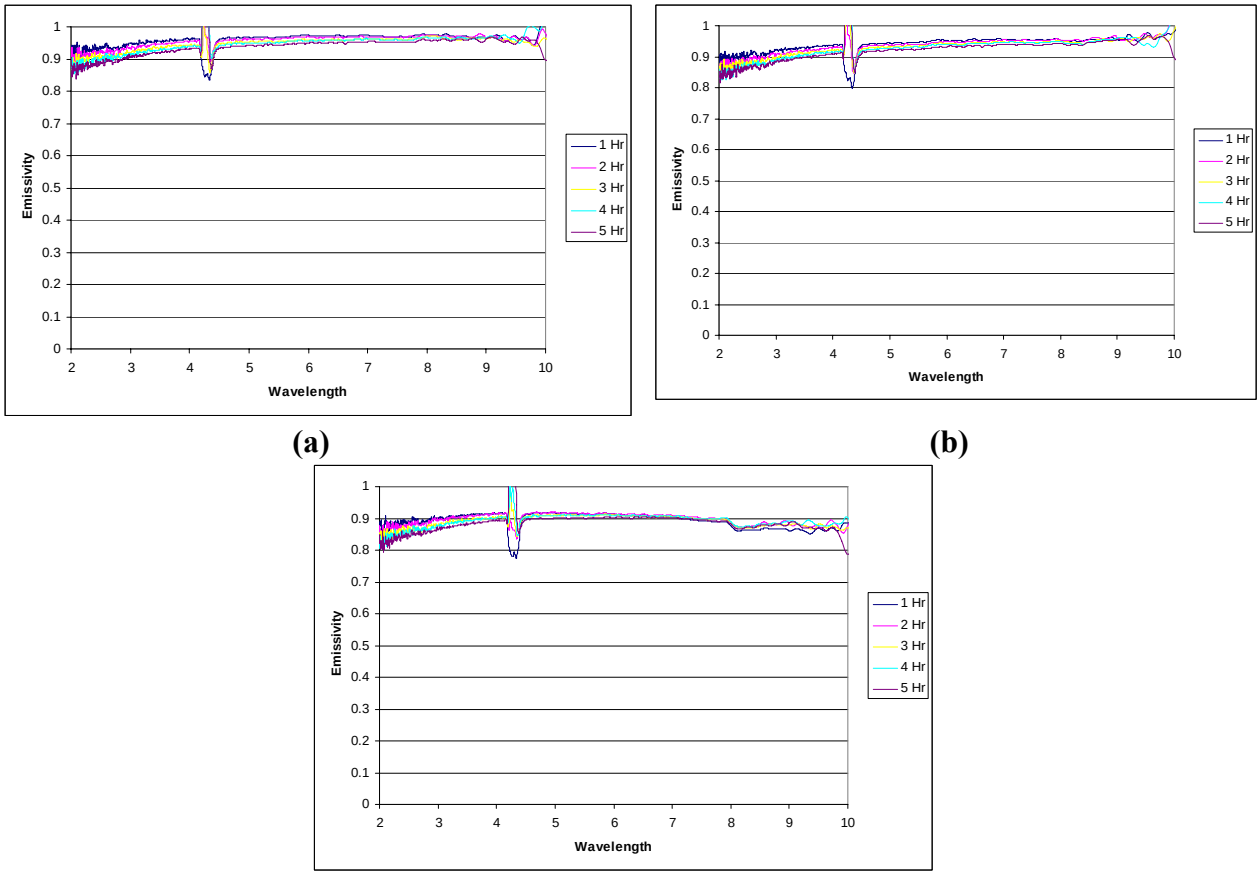

Figure 80. Spectral emmisivity of graphite at 700°C for exposure durations of 1 to 5 hrs, in air for (a) 400 grit surface finish (Ra=0.694μm), (b) 600 grit surface finish (Ra=0.432μm), and 800 grit surface finish (Ra=0.102μm).

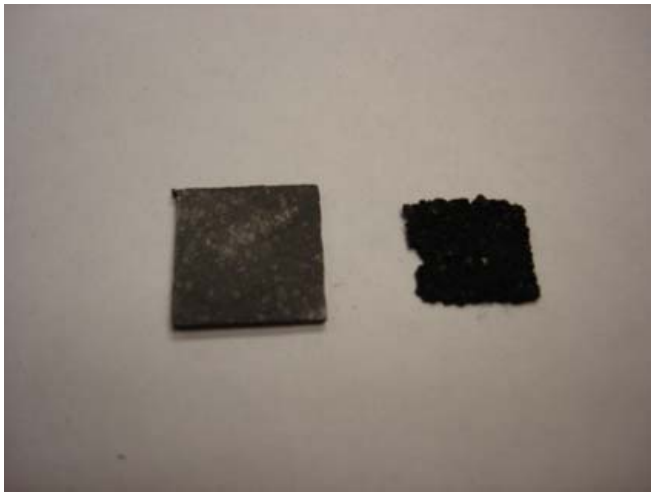

Figure 81. Photograph of the 400 grit polished graphite sample before and after emissivity measurement tests at 700°C, in air.

5. Spectral Emissivity of Surface Treated Materials

5.1. Surface Treatments used in the Present Project

Since emissivity is a near-surface material property, it stands to reason that surface modifications and coatings of materials would have an effect on their spectral emissivity. This could occur due to changes in the chemical composition of the surface, changes in physical topography of the surface, or by the modifications in the nature and thickness of the oxide layer that forms at the materials' surface as a result of these surface treatments. In this project we have investigated four coatings (chemical surface treatments), diamond-like-carbon (DLC), chromium, hafnium, and silicon carbide. The DLC coating was applied to mirror polished samples using a plasma ion implantation and deposition (PIIID) system developed at the University of Wisconsin (Figure 82). Chromium and hafnium sputter cathodes were purchased at 99.99% purity and were used in the sputter deposition system (Figure 83a) to deposit thin films on roughened samples. The SiC film deposition was performed at the commercial facility, LGA Thin Films located in Santa Clara, CA. Additionally two physical surface treatments were also investigated, including, shot peening and xenon ion bombardment. The shot peening system (Figure 83b) impinges the sample surface with small steel pellets, which roughens the surface on a microscopic level and introduces compressive stresses at the surface. Xenon ion bombardment is preformed using the PIIID system and changes the surface texture at the nanometer-level by differential sputtering.

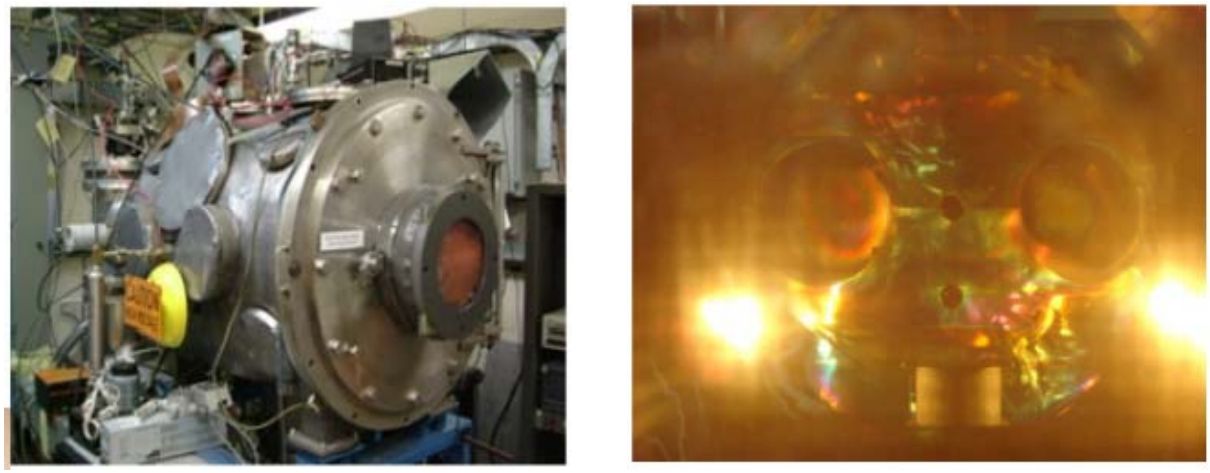

(a) (b)

Figure 82. (a) External view and (b) internal view of PIIID system during Xe ion bombardment. This system was also used for diamond-like carbon (DLC) film deposition.

(a) (b)

Figure 83. Thin film sputter deposition system used for the depositions of Hf and Cr thin films and (b) shot peening system.

5.2. Hafnium Thin Film Deposition on SA508

Samples of SA508 ferritic steel were coated with a 1μm thick hafnium film using sputter deposition. Hafnium was selected because it forms a stable oxide (as a result of reaction with atmospheric oxygen at high temperatures) which would mitigate the oxide layer growth on the underlying alloy. Additionally, hafnium has a high neutron absorption which could potentially reduce the neutron damage to the RPV.

The spectral emissivity of hafnium coated SA508 as measured at 500^{o}C is shown in Figure 84. As may be noted, the spectral emissivity of the coated material is very different from the spectral emissivity of the mirror polished SA508 sample measured under the same test conditions (500^{o}C). This shows the ability of Hf surface treatment to dramatically influence the spectral emissivity of SA508 steel. The hafnium coating seems to provide significant oxidation resistance to the base steel and therefore the oxide layer growth which contributes to the high emissivity of SA508 at 500^{o}C is not observed here. The emissivity is highest at low wavelengths and decreases fairly linearly as wavelength increases. There is a slight increase in emissivity with increasing exposure time, especially at lower wavelengths. There is most likely some oxide growth, which explains the increases in emissivity, but the Hf coating definitely increases oxidation resistance of SA508 steel.

SEM imaging of the Hf-coated SA508 steel showed no visual difference after emissivity testing at 500^{o}C (Fig. 85a and 85b). However, EDS analysis showed the oxygen content of the surface to be 9% after emissivity testing whereas it was about 0.48% before testing. As expected the Hf film oxidized but prevented further diffusion of oxygen to the base steel thereby limiting oxide growth on the base steel. Additionally SEM imaging of the same untested sample

(Figure 85) showed greater polishing mark clarity than in the post tested image, meaning the oxidation of the Hf coating may have lowered surface roughness.

Table 3 compiles the elemental weight percentages from EDS surface scans for all SA508 samples tested. The amount of oxygen from the scans is related to the amount of oxidation that occurs. It may be noted that between 350°C and 500°C, the oxygen content increases significantly for uncoated SA508 steel. However, this upsurge is delayed as evidenced by the still relatively low oxygen content of the Hf-coated SA508 steel even after emissivity testing at 500°C.

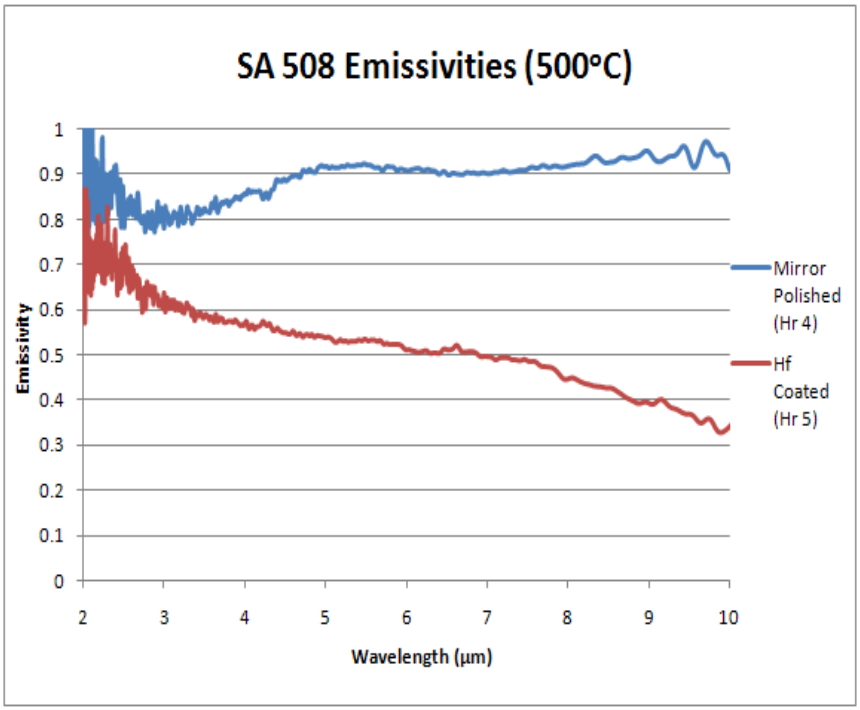

Figure 84. Spectral emissivity of a hafnium coated SA508 steel at 500°C. For comparison spectral emissivity of mirror-polished SA508 steel is also shown.

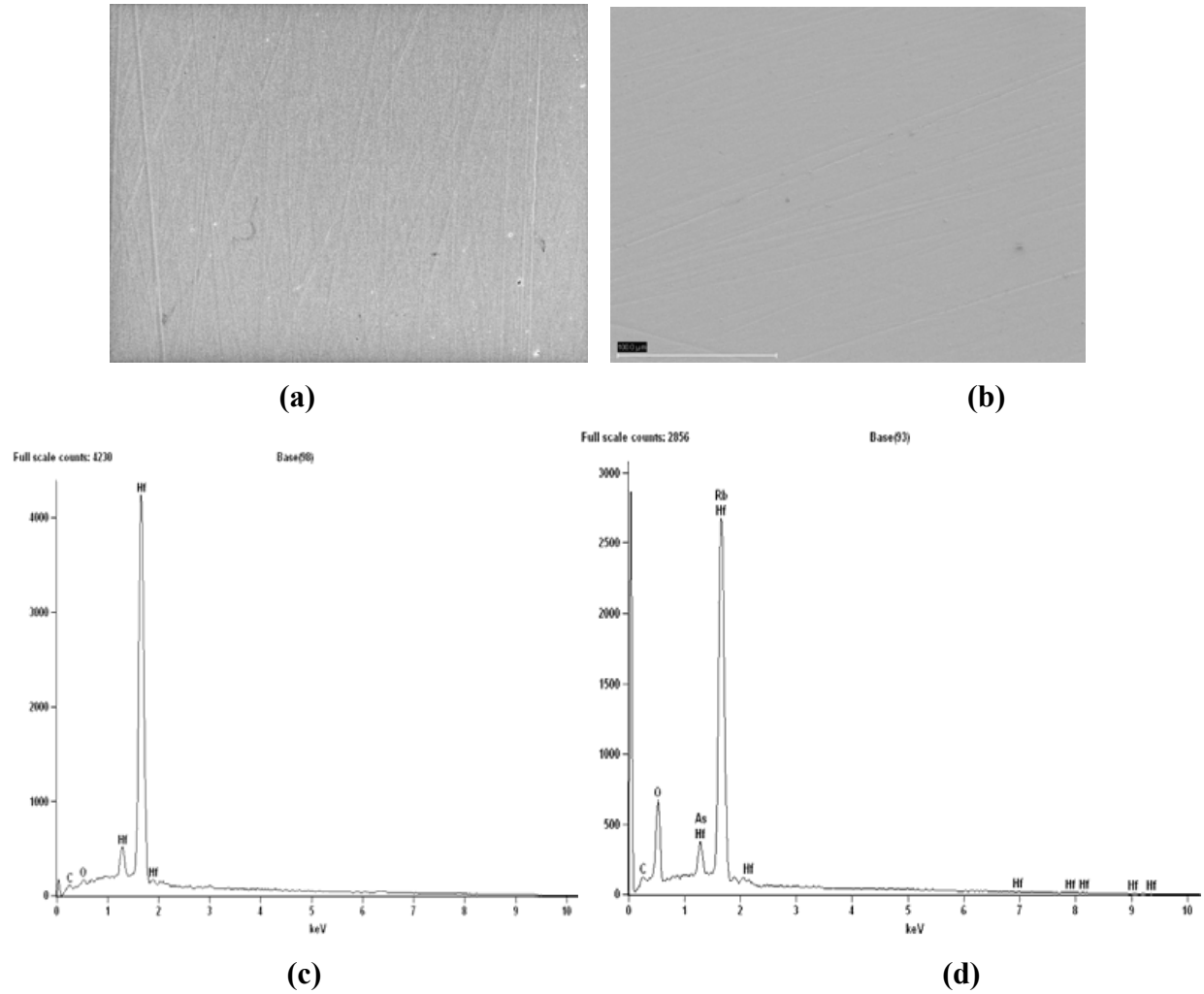

Figure 85. Plan view SEM images of (a) Hf coated SA508 steel (b) Hf coated SA508 steel after emissivity testing at 500°C and (c) and (d) corresponding EDS spectra.

Table 4. Elemental weight percentages for tested and untested SA508 samples.

Surface Condition	Test Temp °C	Fe	C	Si	Mn	O	Hf
Mirror	Baseline - 25	94.22	1.38	1.69	1.61	0	0
Mirror	350	89.14	0.99	0.65	0	9.22	0
Mirror	500	70.23	1.92	0	2.17	25.68	0
Mirror	700	71.34	2.37	0.28	1.83	24.14	0
Hf Coated	Baseline - 25	0	0.5	0	0	0.48	99.02
Hf Coated	500	0	1.48	0	0	8.65	88.46

5.3. Chromium Thin Film Deposition on IN800H:

Thin films of chromium, ~1μm in thickness, were deposited using the sputter deposition process on IN800H samples ground to a 400 grit surface finish. The surface roughness values (Ra) as measured by profilometry (Fig. 86) were 0.021μm and 0.027μm for the uncoated and Cr-coated samples of IN800H samples, respectively. This indicates that the deposited Cr films conformed reasonably well to the substrate surface. Figure 87 shows the spectral emissivity results at 500°C for IN800H samples ground to a surface finish of 400 grit (without Cr coating). The emissivity values remain constant at about 0.4 over the entire range of wavelengths. SEM images of the 400 grit sample (Figure 88a) showed the surface was visually similar to the mirror-polished sample after the 500°C emissivity test. Additionally, the EDS spectrum (Figure 88b) showed similar weight percentages of oxygen (4.34% compared to 5.99% at 500°C).

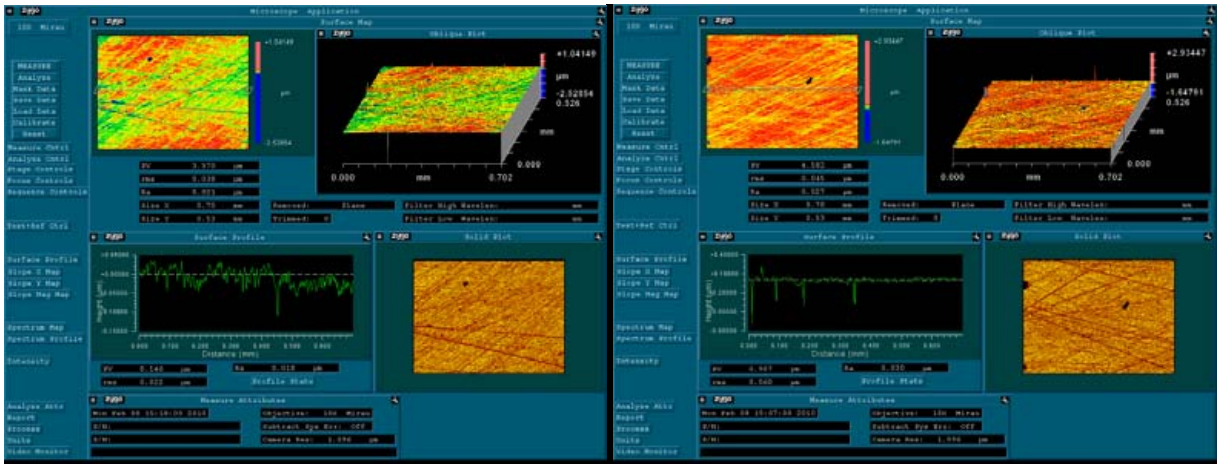

(a) **(b)**

Figure 86. Profilometery of the surface of 400 grit surface finish IN800H samples showing average roughness (a) before and (b) after chromium film deposition.

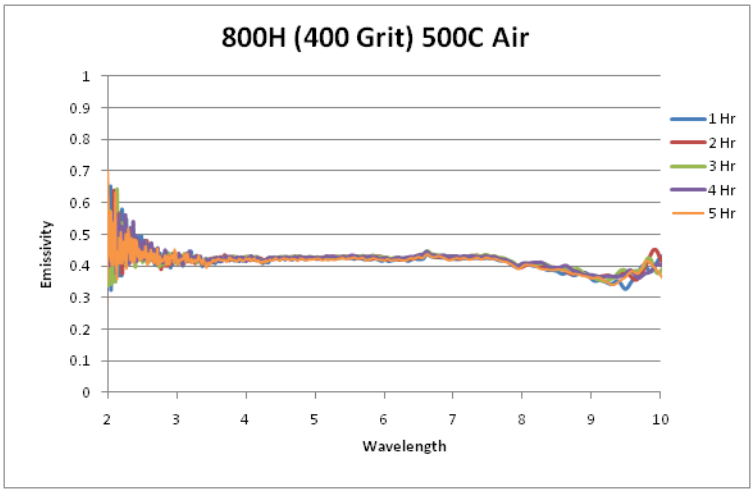

Figure 87. Spectral emissivity of 400 grit surface finish (Ra = 0.021 μm) IN800H at 500°C.

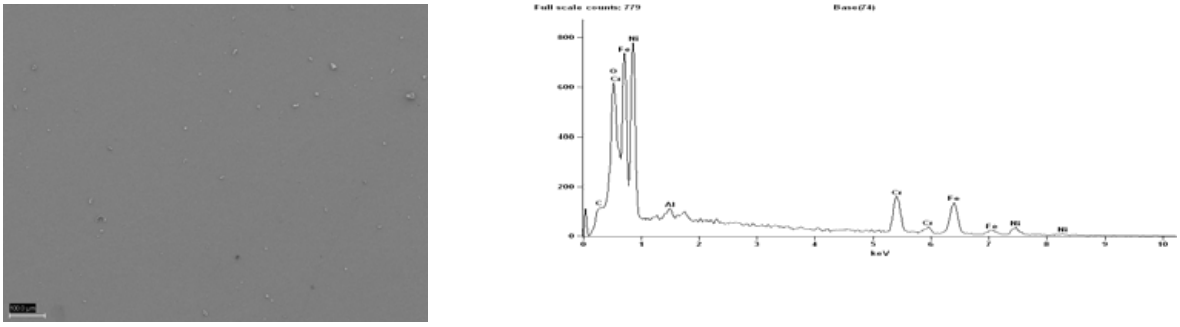

(a) **(b)**

Figure 88. (a) Plan view SEM image of roughened (Ra = 0.021 µm) IN800H after emissivity testing at 500°C and (b) corresponding EDS spectrum.

The chromium coated sample has a significantly different emissivity spectrum (Figure 89) compared to the other IN800H samples tested so far. At low wavelengths the magnitude of the emissivity was higher than any other IN800H samples (~0.7), and it experiences a linear decline to about 0.4 at high wavelengths with the possibility of leveling off at even higher wavelengths. Even though IN800H is high in chromium, it is still a bulk iron alloy, meaning that the oxide that normally forms on the surface is most likely an iron-chromium or Ni-Cr spinel oxide, which has a characteristic spectral emissivity. The emissivity spectrum recorded is a combination of the base alloy emissivity and the spinel layer. The sample coated with a chromium film will most likely form a pure chromium oxide layer (Cr_2O_3) which has a different characteristic emissivity leading to the differences in the spectrum for this sample. The difference between the 2-hour data from the other hours was due to a problem with mirror rotation and is not an actual physical difference.

The spectral emissivity results indicate that a chemical surface treatment such as Cr coating can be used to control a sample's emissivity. SEM images of the samples after chromium coating (Figure 90a) showed good adhesion and a smooth surface, but some minor cracking was observed after emissivity testing at 500°C (Figure 90b). Corresponding EDS scans (Figure 90c) showed slight oxidation of the surface before any testing was initiated, which is expected behavior for pure chromium at room temperature. The EDS spectrum (Figure 90d) showed a higher oxygen level due to the formation of at the surface during emissivity testing at 500°C.

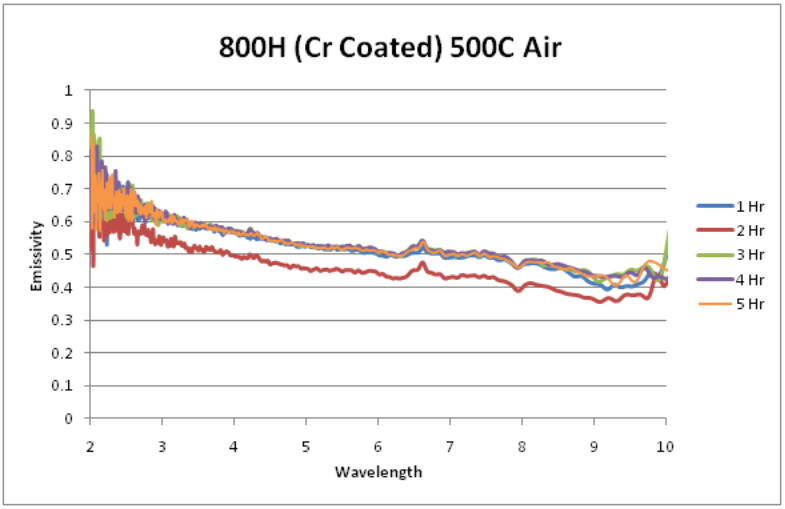

Figure 89. Spectral emissivity of a Cr-coated IN800H after emissivity testing at 500°C.

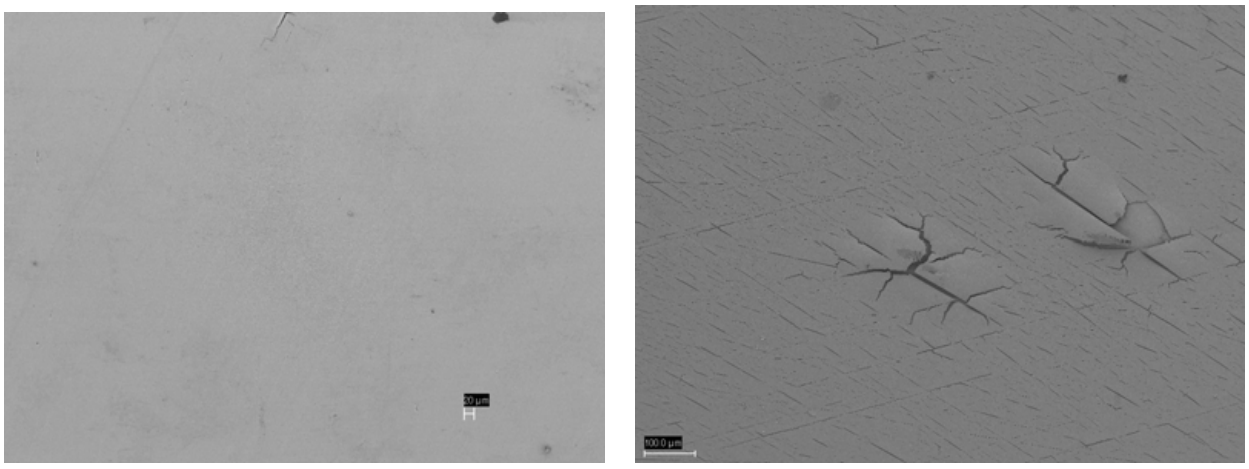

(a) (b)

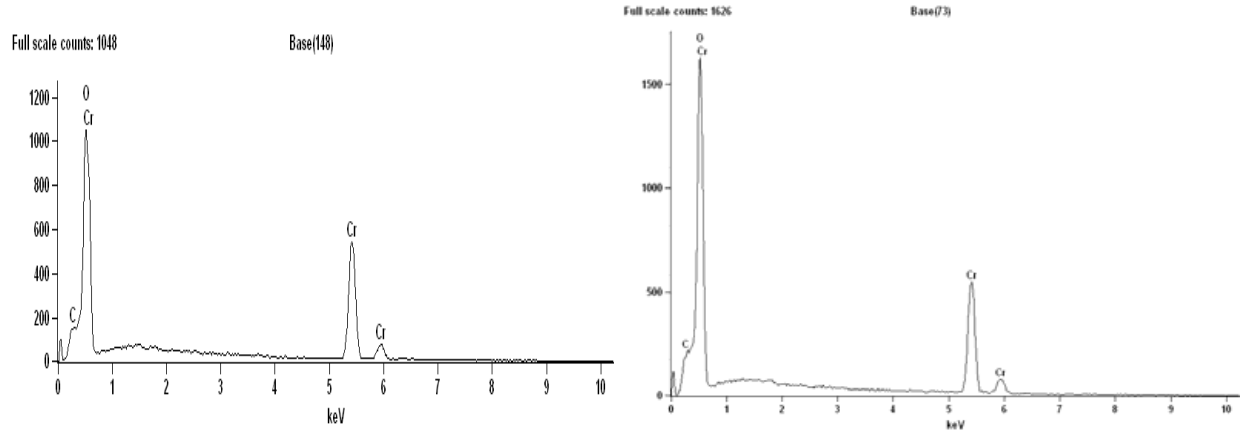

(c) (d)

Figure 90. Plan view SEM images for chromium coated IN800H samples (a) untested and (b) after emissivity testing at 500°C and (c) and (d) corresponding EDS spectra.

5.4. Shot Peening of IN800H:

IN800H samples were ground to a surface finish of 400grit prior to shot peening. The spectral emissivty of shot-peened IN800H at 500°C is shown in Figure 91. Both the shot peened and 400 grit sample have the same basic shape to their spectral emissivities (Figures 91 and 87), being relatively constant over a range of wavelengths, although the shot peened samples have higher value and trend upwards at very high wavelengths similar to the mirror polished samples, while the 400 grit sample trends downwards. The magnitude of the emissivity of shot peened sample is much higher than the mirror polished or 400 grit samples, which is expected due to the much rougher surface as indicated by the results of profiilometry (Figure 92).

SEM images of the shot-peened sample before and after testing (Figure 93a and 93b) showed a definite smoothing of the surface after the emissivity testing at 500°C, characteristic of surface oxidation. EDS scans (Figure 93c) showed a higher level of chromium and oxygen at the surface compared to a mirror polished sample tested at the same temperature. The shot peening of the surface reduces grain size, allowing for greater transport of chromium along grain boundaries which leads to greater oxidation [41]. Table 5 summarizes the surface chemical composition of the all the conditions tested for IN800H.

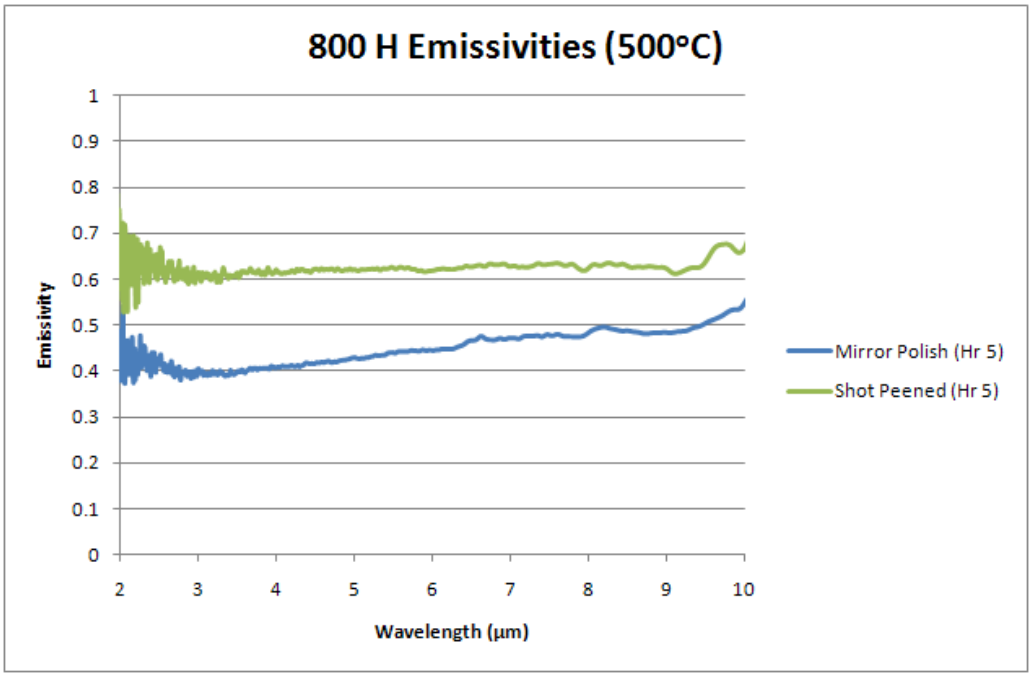

Figure 91. Spectral emissivity of a shot peened IN800H sample at 500°C. For comparison spectral emissivity of mirror-polished IN 800H at 500°C is also shown.

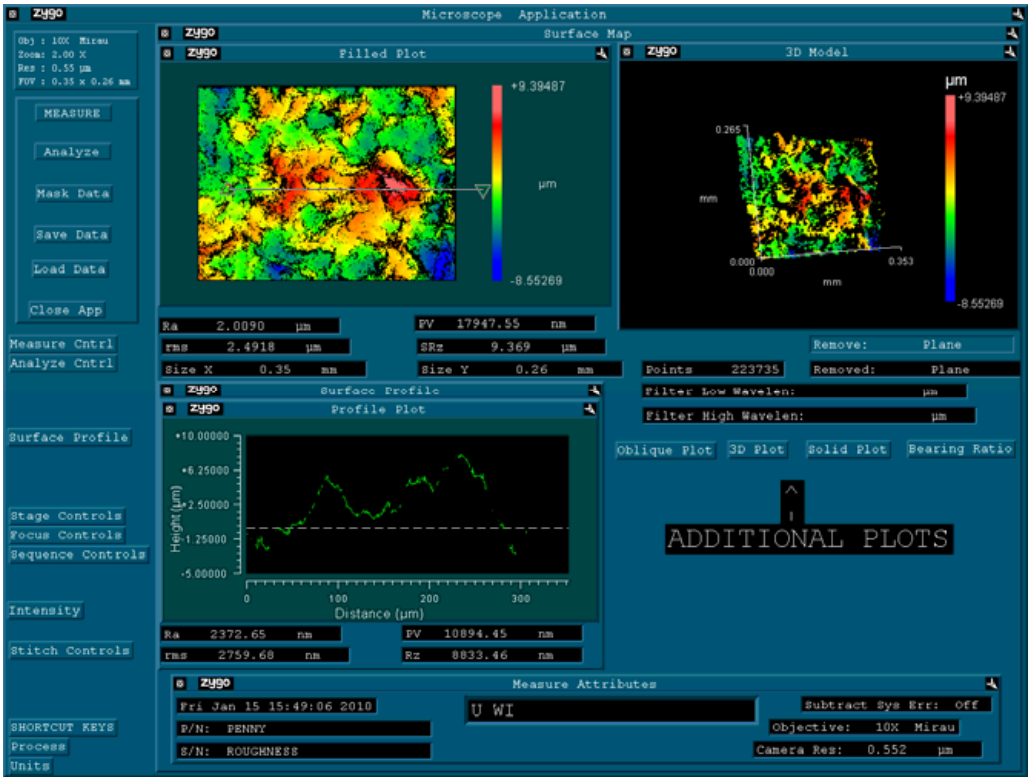

Figure 92. Profilometery of shot peened IN800H sample after emissivity testing at 500°C.

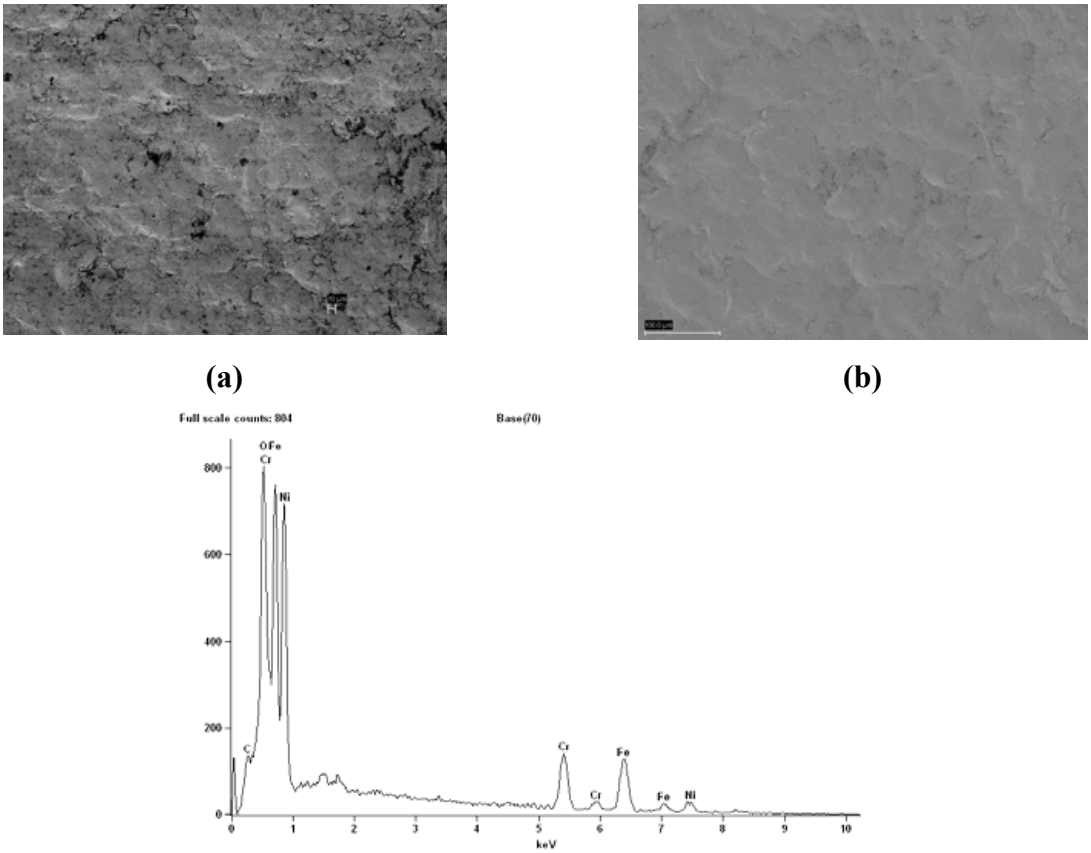

Figure 93. Plan view SEM images for shot peened Incoloy 800H samples (a) untested and (b) after emissivity testing at 500°C, (c) EDS spectrum after emissivity testing at 500°C.

Table 5. Elemental weight percentages for tested and untested Incoloy 800H samples.

Surface Condition	Test – Temp (C)	Fe	Ni	Cr	C	Si	Mn	Al	Ti	O
Mirror	Baseline - 25	45.18	30.29	20.49	1.9	0.25	0.86	0.61	0.43	0
Mirror	49 - 500	45.28	31.3	16.63	0.8	0	0	0	0	5.99
Mirror	50 - 700	25.16	17.26	35.13	1.66	1.15	3.58	0.95	1.36	13.75
Shot Peened	53 - 500	42.55	27.87	22.11	0.84	0	0	0	0	6.63
Cr Coated	Baseline - 25	0	0	94.84	1.24	0	0	0	0	3.92
Cr Coated	61 - 500	0	0	88.91	1.41	0	0	0	0	9.68
400 Grit	61 - 500	41.03	29.87	23.38	0.8	0	0	0.58	0	4.34

5.5. Hafnium Thin Film Deposition of IN617:

Thin films of hafnium (~1μm in thickness) were deposited on IN617 samples ground to a 400grit surface finish. First, emissivity measurements were made of the 400 grit ground IN617 at 500°C. (Figure 94). The 400 grit surface finished IN617 exhibited the same spectral emissivity behavior as their mirror-polished counterparts, although there was less decrease in emissivity at higher wavelengths. This could be attributed to the greater roughness of the sample or to measurement uncertainty. Figure 95a, the SEM plan view image of the IN617 sample after emissivity measurements at 500°C, shows a smooth surface with very little evidence of oxidation. The EDS spectra of this surface (Figure 95b) confirmed the presence of some oxygen on the surface (2.3 wt.%). Table 5 compiles the elemental weight percentages from EDS surface scans for all Inconel 617 samples tested, except the mirror polished sample at 500°C.

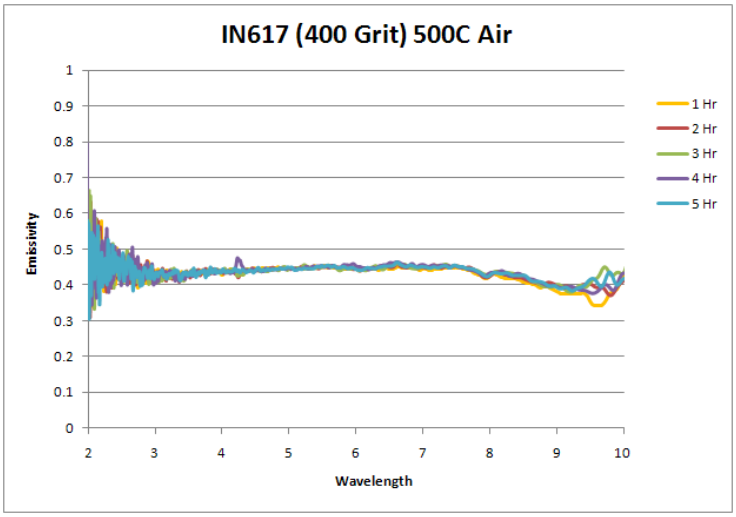

Figure 94. Spectral emissivity of a 400 grit surface finish IN617 sample at 500°C.

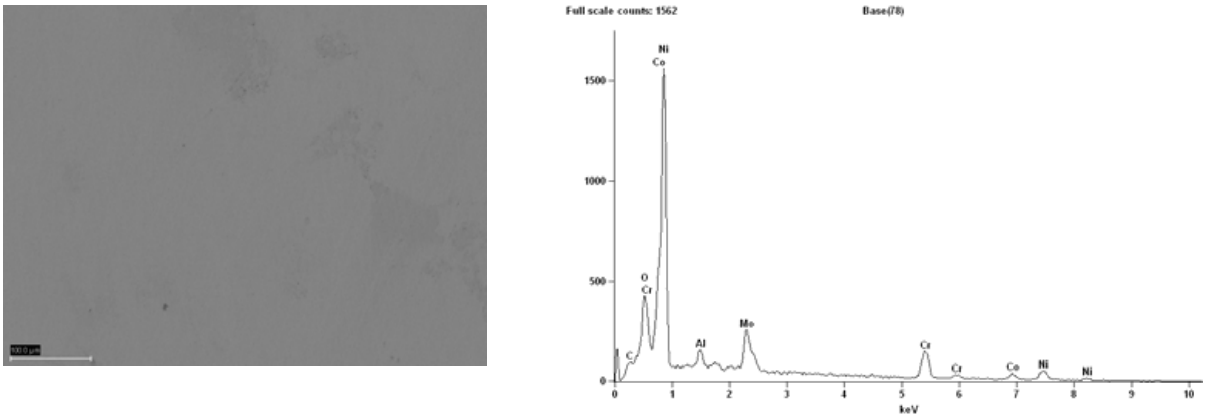

(a) **(b)**

Figure 95. (a) Plan view SEM image for 400 grit surface finish IN617 after emissivity testing at 500°C and (b) corresponding EDS spectrum.

Hafnium coated IN 617 showed highest emissivity at low wavelengths and a linear decrease with higher wavelengths (Figure 96) indicating that Hf thin film surface treatment changes emissivity. The emissivity value is higher than the uncoated IN617 due the formation of higher hafnium-oxide during the 500°C emissivity test. SEM images of an untested Hf coated sample before and after emissivity testing are shown in Figures 97a and 97b, respectively. EDS scans for the two samples (Figures 97c. 97d, and Table 6) show there was negligible oxygen on the surface before testing (1.58%), but after testing the oxygen content increases to 9.57%.

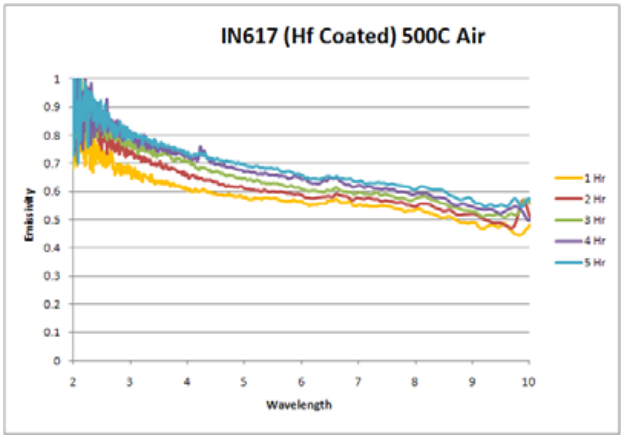

Figure 96. Spectral emissivity of a hafnium coated IN617 at 500°C.

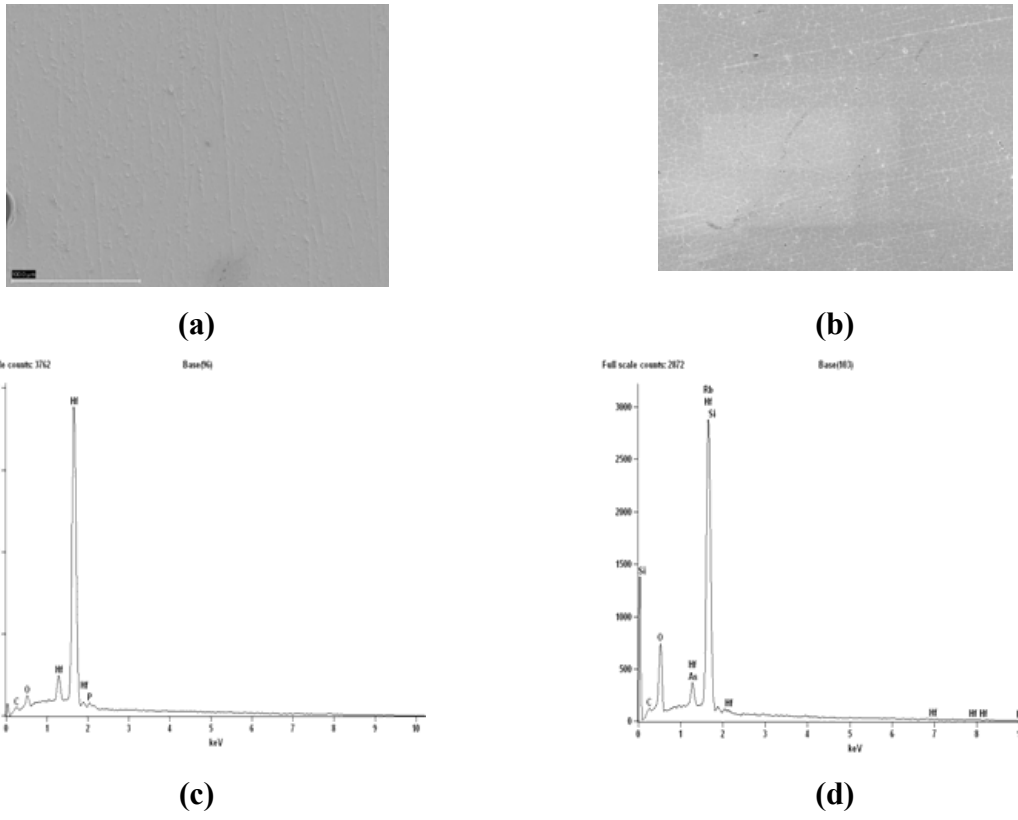

Figure 97. Plan view SEM at the same magnification for Hf coated Inconel 617 sample both (a) untested and (b) after emissivity testing 500°C and (c) and (d) corresponding EDS spectra.

Table 6. Elemental weight percentages for tested and untested Inconel 617 samples.

Surface Condition	Test – Temp (C)	Fe	Ni	Cr	C	Si	Mo	Al	Ti	Co	O	Hf
Mirror	Baseline - 25	1.06	52.93	21.95	1.47	0.2	8.52	1.07	0.46	12.35	0	0
Mirror	52 - 700	1.11	46.54	20.47	2.16	0.81	7.81	1.13	0.47	11.52	7.99	0
400 Grit	66 - 500	0	48.83	22.64	0.9	0	9.99	1.29	0	14.01	2.33	0
Hf Coated	Baseline - 25	0	0	0	0.44	0	0	0	0	0	1.58	97.9
Hf Coated	66 - 500	0	0	0	1.34	0	0	0	0	0	9.57	89.08

5.6. Silicon Carbide Coating Deposition on Haynes 230:

Monolithic silicon carbide coatings, ~1μm in thickness, were deposited on mirror-polished Haynes 230 samples. Silicon carbide depositions were performed at the company LGA Thin Films located in Santa Clara, CA. SEM examination showed of coatings (Figure 98a) showed the coatings were reasonably uniform. The corresponding EDS spectrum of SiC coated samples (Figure 98b) showed that the coating was pre-dominantly silicon-carbide but small amounts of nickel, chromium, aluminum, silver and oxygen were also present in the coating. Some signal of nickel and chromium could be expected to emanate from the underlying Haynes 230 substrate, however trace amounts of aluminum, silver, and oxygen appear to have got incorporated in the coating during the deposition process.

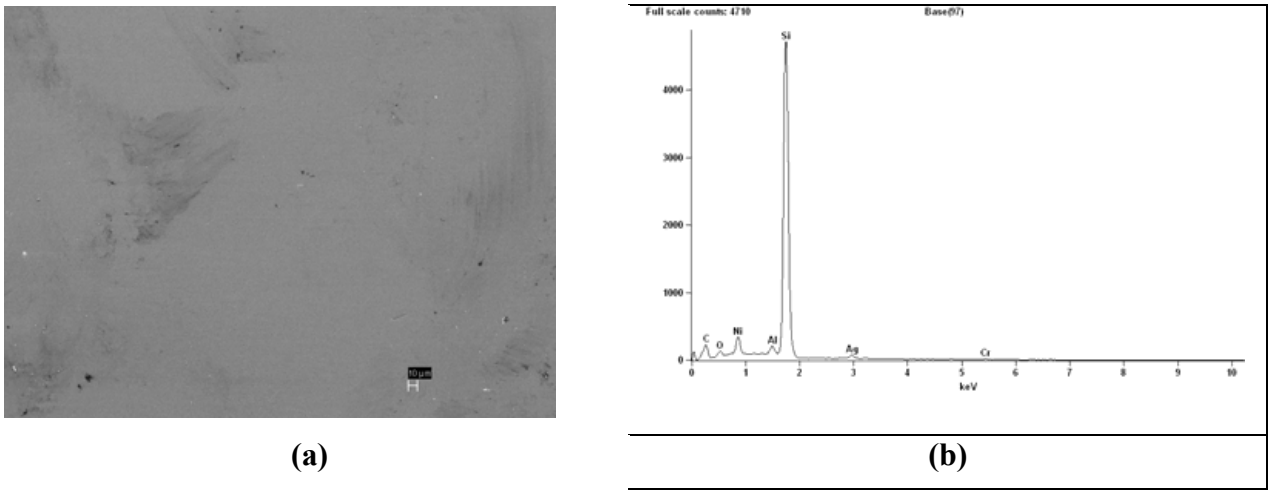

(a) **(b)**

Figure 98. (a) plan view SEM image of as-received SiC coating and (b) corresponding EDS spectrum.

Figure 99 shows the spectral emissivity of the SiC coated Haynes 230 at 500°C. For comparison, Figure 100 shows the spectral emissivity of bare Haynes 230 at 500°C. For the SiC coated samples (Figure 99), the spectral emissivity exhibits a first maximum (~0.8) just above 2

microns, quickly decreases to a minimum (~0.4) at 3 microns, increases at a slow rate to a second maximum (~0.8) at about 6.5 microns, and finally decreases slightly until it levels out at about 0.65 at high wavelengths. The lack of variation with changes in exposure time is because the SiC coating remains chemically inert and also prevents oxidation of the substrate alloy.

The differences in the spectral emissivity for the SiC coated Haynes 230 sample versus the bulk SiC control (or bare Haynes 230) is expected from thin film theory. As the coating is quite thin (one micron), the total surface emissivity comes partially from the SiC coating and partially from the substrate material. This explains why the spectral emissivity is shaped neither like the bare Haynes 230 or the bulk SiC control. The maxima and minimum in the spectrum suggest the sort of constructive and destructive interference produced by growing oxide layers. It would be interesting to see if these peaks would shift to higher wavelengths if the thickness of the SiC coating were increased.

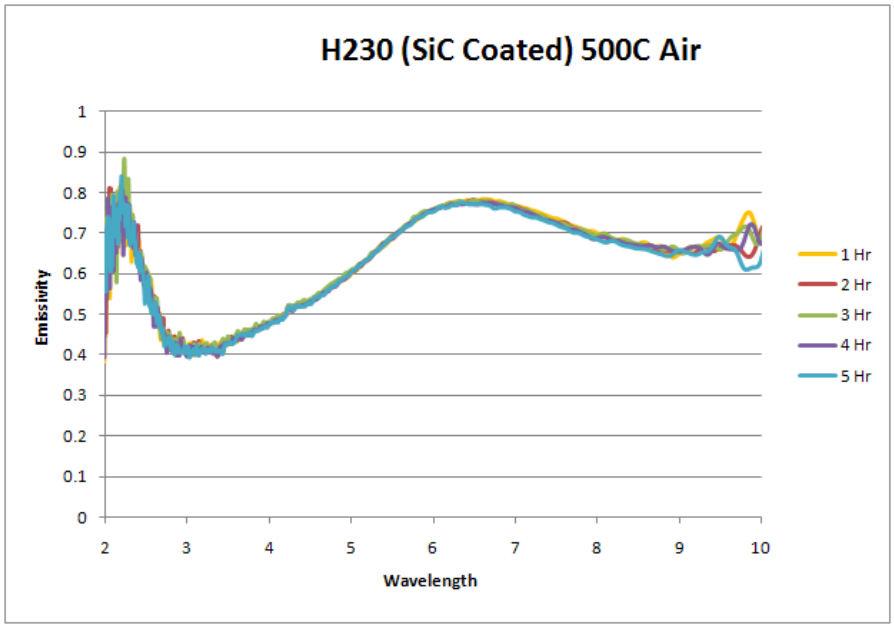

Figure 99. Spectral emissivity of SiC coated Haynes 230 at 500°C.

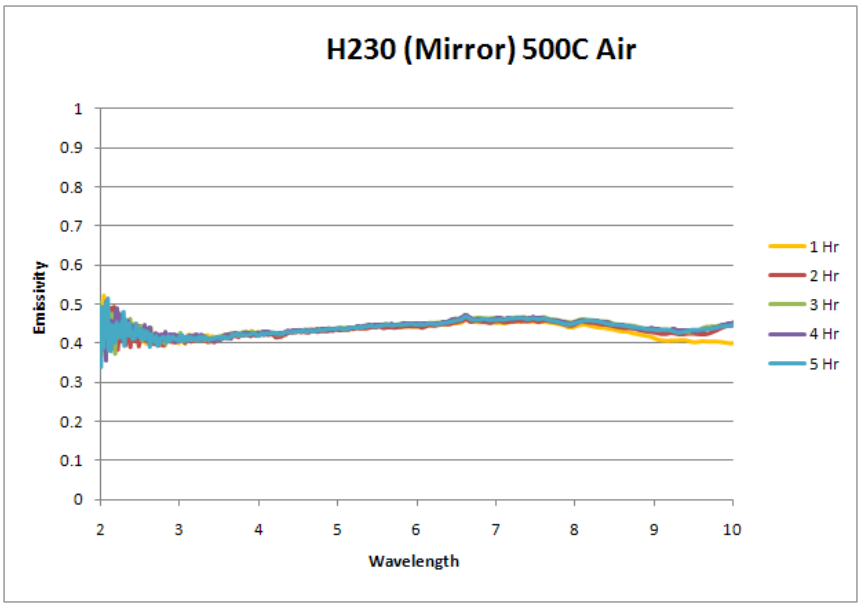

Figure 100. Spectral emissivity of a Haynes 230 alloy at 500°C.

The SEM imaging of the sample tested for emissivity at 500°C (Figure 101a) was visually similar to the untested sample,. The post-testing EDS spectrum (Figure 18b) shows most of the impurities seen in the untested sample, although silver and chromium are no longer present, so silicon is correspondingly higher. The amount of surface oxygen does not change 9at least within EDS resolution limits) after testing at 500°C so a lack of surface oxidation is confirmed.

Table 7 compiles the elemental weight percentages from EDS surface scans for all Haynes 230 samples tested. It would appear that oxidation of the surface of a Haynes 230 sample does not begin until some temperature between 350°C and 500°C, while there is a marked increase in growth rate at 700°C.

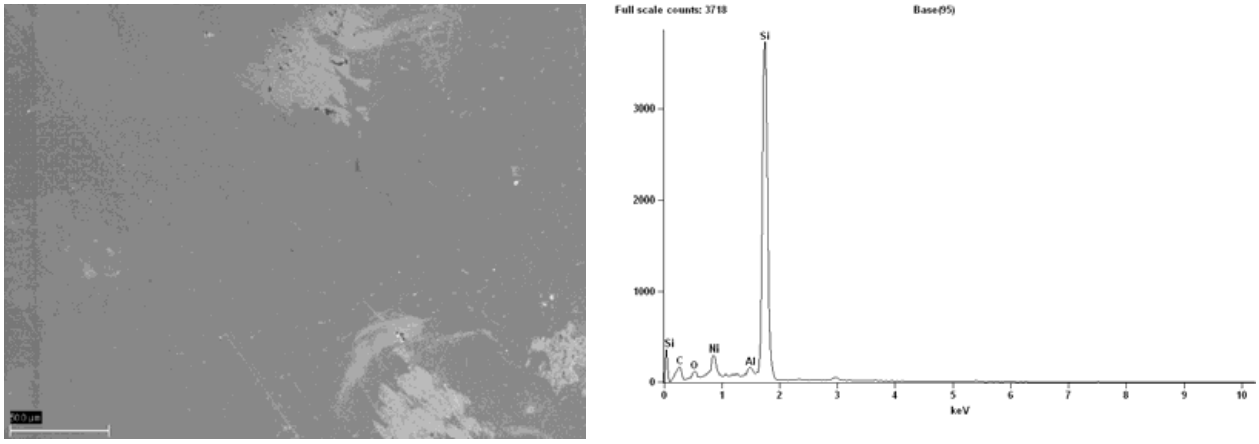

(a) **(b)**

Figure 101. (a) plan view SEM image of as-received SiC coated Haynes 230 after emissivity testing at 500°C and (b) corresponding EDS spectrum.

Table 7. Elemental weight percentages for tested and untested Haynes 230 samples.

Surface Condition	Test – Temp (C)	Fe	Ni	Cr	C	Mn	W	Si	Al	Ag	O
Mirror	Baseline - 25	1.63	56.8	22.16	1.16	0.56	17.15	0	0	0	0
Mirror	81 - 350	0	56.57	27.18	0	0	15.66	0.59	0	0	0
Mirror	49 - 500	0	52.73	24.35	0.67	2.32	17.92	0	0	0	2.01
Mirror	50 - 700	0	49.67	24.89	0.83	0	18.91	0	0	0	5.69
SiC Coated	Baseline - 25	0	7.44	3.48	8.74	0	0	71.12	1.35	6.25	1.63
SiC Coated	53 - 500	0	8.88	0	6.62	0	0	81.07	1.59	0	1.84

5.7. Diamond-like Carbon (DLC) Film Deposition on 508 Ferritic Steel and 304 Stainless Steel:

Diamond-like carbon (DLC) is a carbon-based material with hydrogen incorporated it. It is typically synthesized using plasmas of hydrocarbon gases. It is an optically translucent material. For this project DLC films (~1μm) were deposited on SA508 ferritic steel and 304 austenitic steel. Figure 102 and 103 show spectral emissivity spectra for uncoated and DLC coated SA508 and 304 stainless steel, respectively, at 350°C. In both cases a very intriguing increase in emissivity is observed at low wavelengths caused by optical interference effects from the DLC film which is optically translucent. As observed by SEM EDS analyses (Figure 104), the DLC film was generally stable at 350°C and the oxidation of the underlying substrate is still low to mechanically disrupt the DLC film (some DLC spallation was observed for 304 stainless steel).

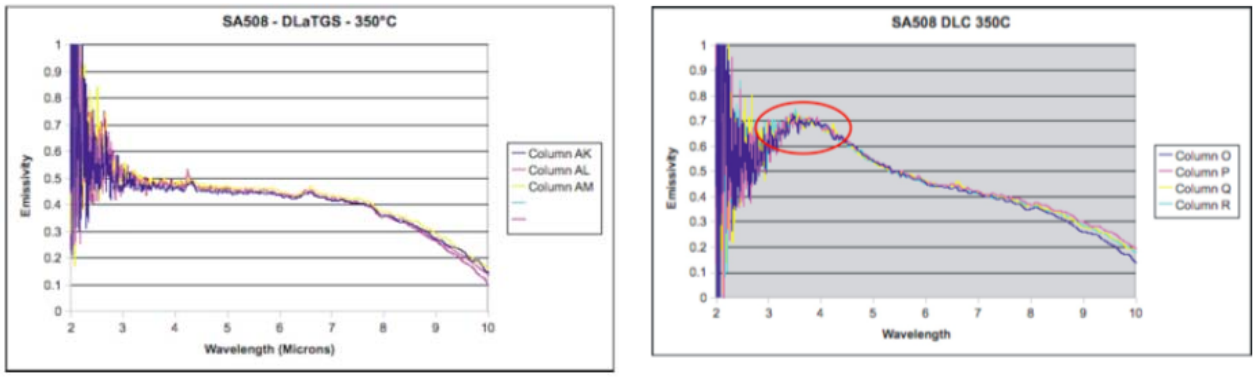

(a) **(b)**

Figure 102. Spectral emissivity of SA508 ferritic steel at 350°C (a) uncoated and DLC coated.

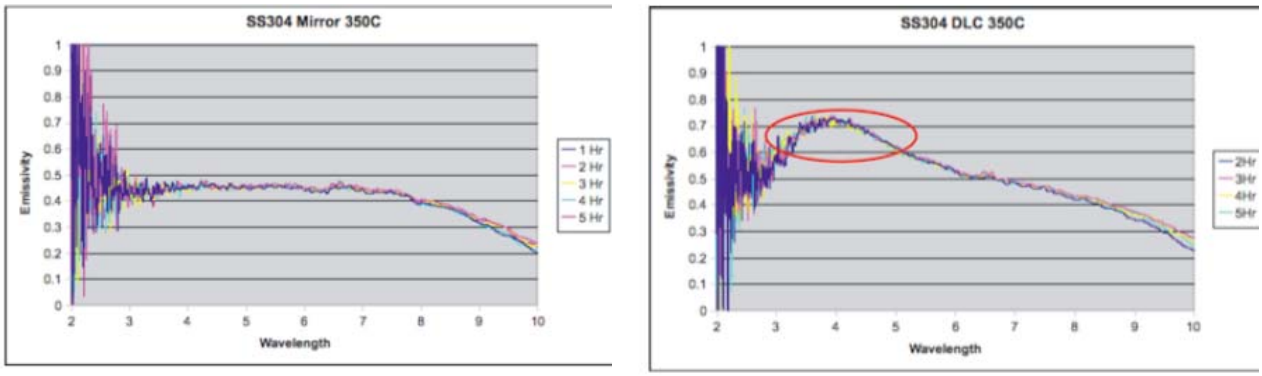

(a) **(b)**

Figure103. Spectral emissivity of 304 stainless steel at 350°C (a) uncoated and (b) DLC coated.

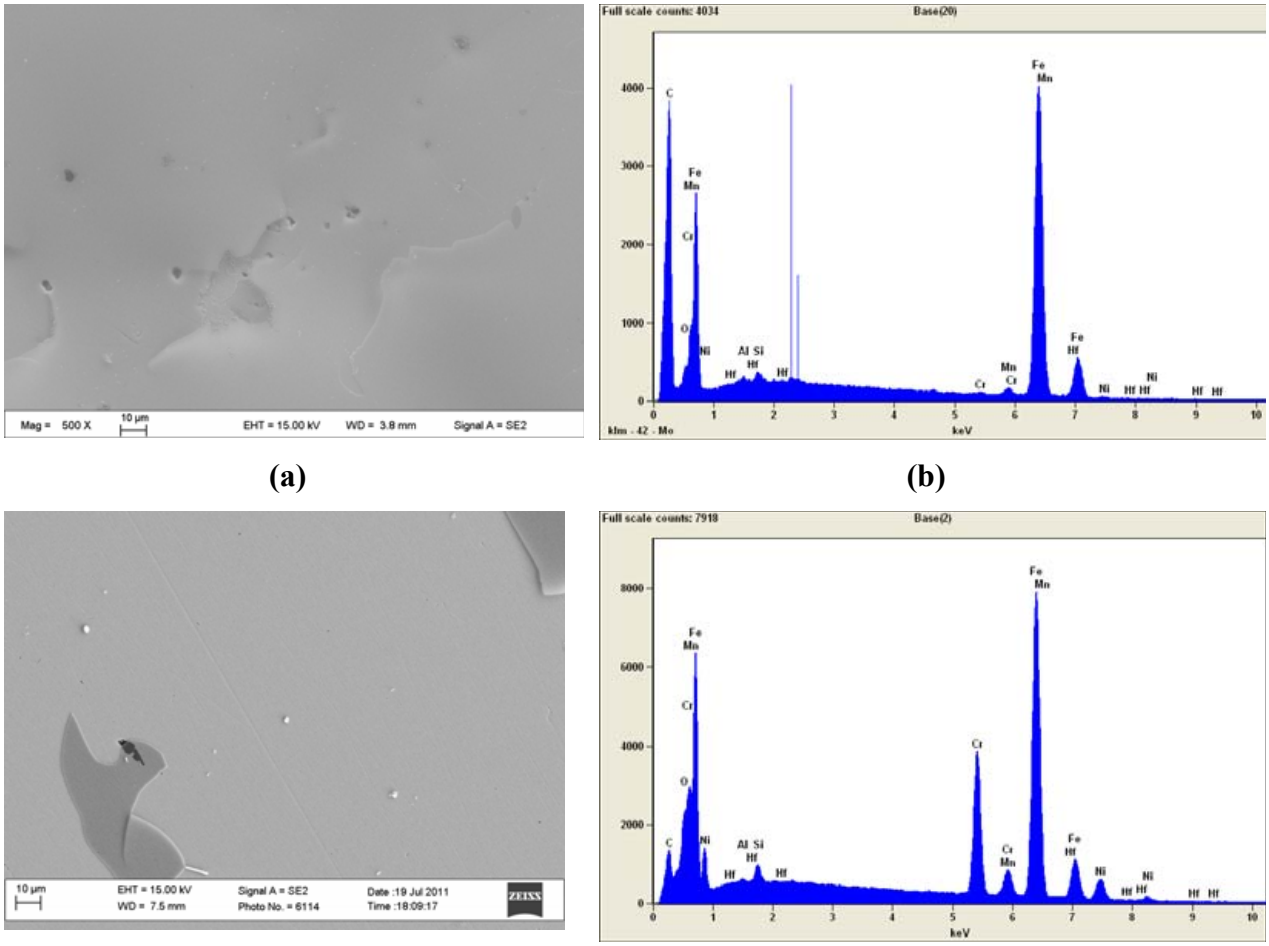

(c) **(d)**

Figure 104. SEM images and EDS spectra for DLC coated steels after emissivity testing at 350oC (a) surface image of SA508 steel, (b) EDS spectrum for SA508 steel, (c) surface image of 304 stainless steel, and (d) EDS spectrum for 304 stainless steel.

Figure 105 shows the spectral emissivity of DLC coated SA508 ferritic steel and 304 austenitic stainless steel at 500°C. The spectral emissivity of DLC coated SA508 is high and comparable to its uncoated counterpart. SEM examination (Figure 106b) shows that the profuse oxidation of the underlying SA508 steel and dominated the emissivity signal. For 304 stainless steel oxidation is much less pronounced. (Figure 106d), however EDS analyses showed very little or no carbon at the surface. It is speculated that 500°C the DLC film reacted with air and sublimates from the surface as carbon-dioxide.

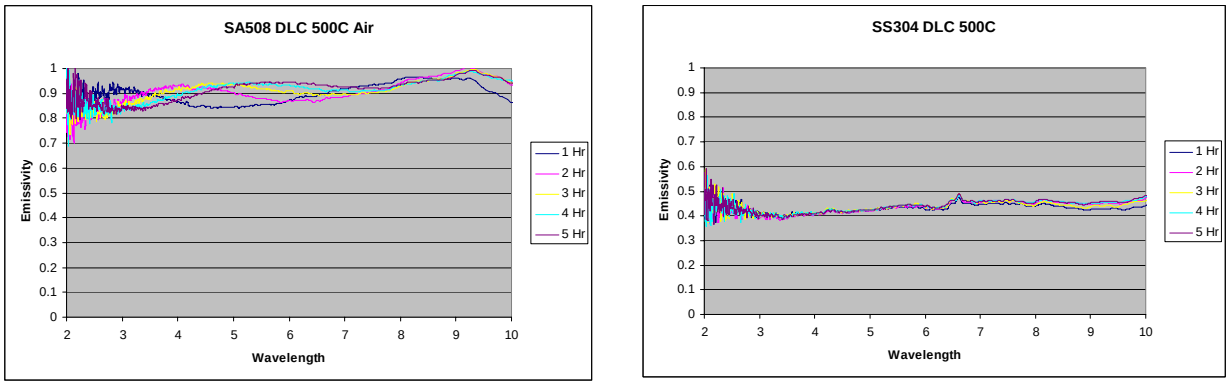

(a) **(b)**

Figure 105. Spectral emissivity of DLC coated materials at 500°C (a) SA508 and (b) 304 stainless steel.

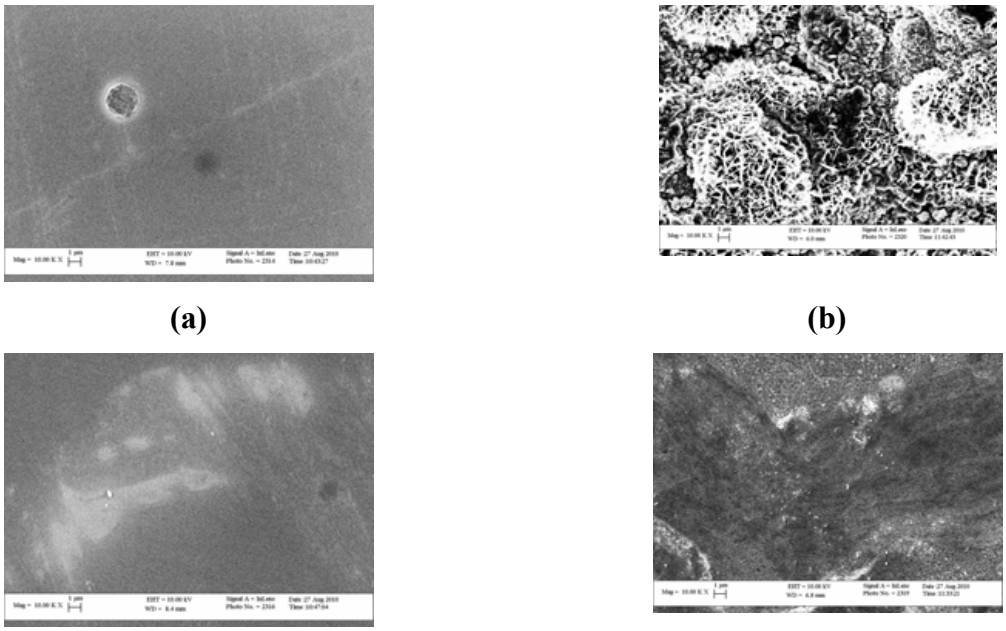

(a) **(b)**

(c) **(d)**

Figure 106. SEM images of DLC coated materials before and after emissivity testing at 500°C, (a) SA508 before testing, (b) surface of DLC coated SA508 after testing, (c) DLC film on 304 stainless steel before testing, and (d) surface of DLC coated 304 stainless steel after testing.

5.7. Xe^+ Bombardment of T22 Ferritic Steel:

Energetic Xe^+ ion bombardment (20KV) was performed on mirror-polished T22 ferritic steel. The goal was to induce topographical and compositional changes on the material's surface on a nanometer dimensional scale. The expectation was that such a surface treatment would alter the nature of the oxide that develops on the surface of T22 steel at high temperatures. At 350°C there is no significant difference between the spectral emissivities of untreated and Xe^+ ion bombarded T22 ferritic steel, except that at lower wavelengths, the emissivity of the Xe^+ ion bombarded samples is slightly higher (Figure 107).

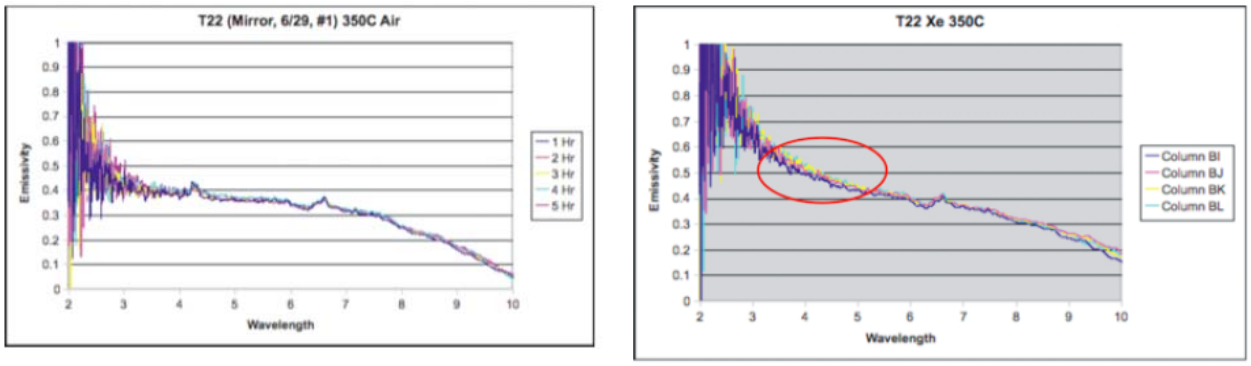

(a) **(b)**

Figure 107. Spectral emissivity of T22 ferritic steel at 350°C, (a) mirror-polished, (b) Xe^+ ion bombarded.

At 500°C the trends in spectral emissivities are substantially different for the untreated and Xe^+ ion bombarded samples of the T22 steel (Figure 108). The waviness in the spectral emissivity is substantially attenuated as a result of Xe^+ ion bombardment. It is speculated that Xe^+ ion bombardment changes the morphology and mechanical stability of the oxide which results in the changes in trends in spectral emissivities. Figure 109 show high magnification SEM images of untreated and Xe^+ ion bombarded T22 steel samples after emissivity tests at 500°C. As may be noted in this figure, Xe^+ ion bombardment significantly alters the size scale of the morphology of the oxide layer that forms on the surface of the T22 steel at 500°C. This observation warrants further investigation.

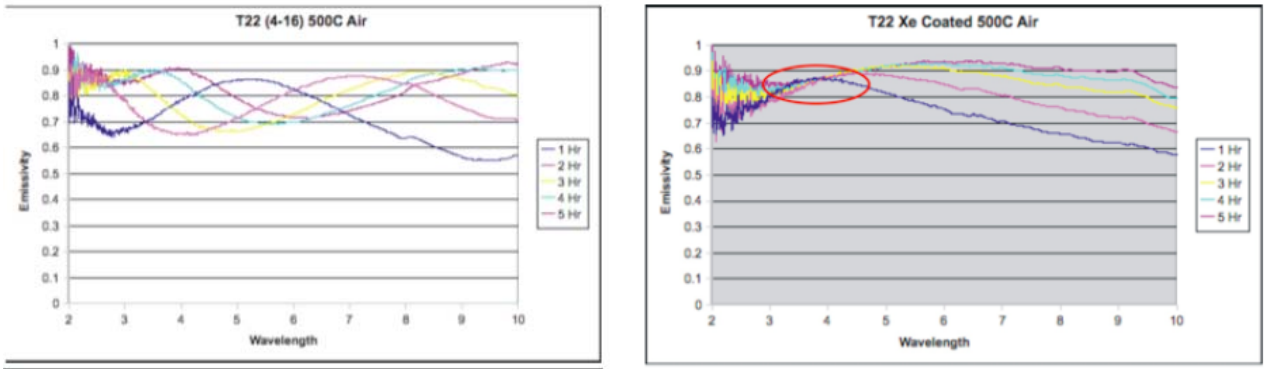

(a) **(b)**

Figure 108. Spectral emissivity of T22 ferritic steel at 500°C, (a) mirror-polished, (b) Xe^+ ion bombarded.

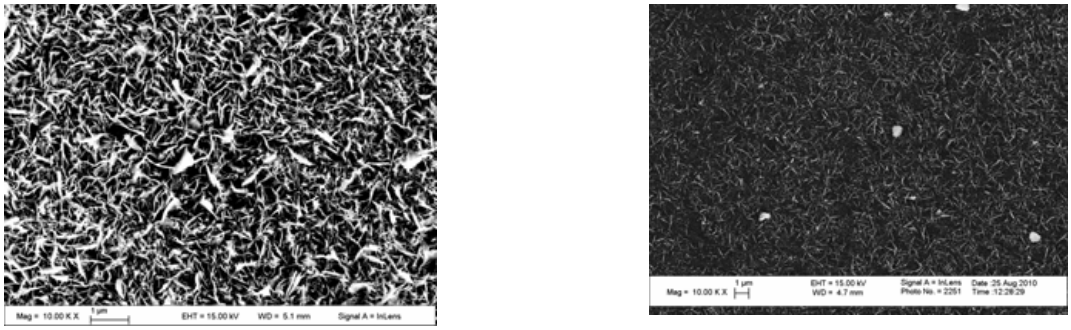

(a) **(b)**

Figure 109. SEM plan view images of after emissivity testing at 500°C of T22 ferrtic steel (a) untreated, mirror-polished, and (b) mirror-polished and Xe^+ ion bombarded.

5.8. Summary of Spectral Emissivity Tests of Surface Treated Materials

A summary of integrated spectral emissivities (over 4μm to 10μm wavelength) at 350°C, 500°C, and 700°C is shown in Figure 110. A comparison with Figure 71 (in conjunction with the earlier discussions in this section) shows that depending on the alloy and test temperature, surface treatments can be used to control spectral emissivity of alloys.

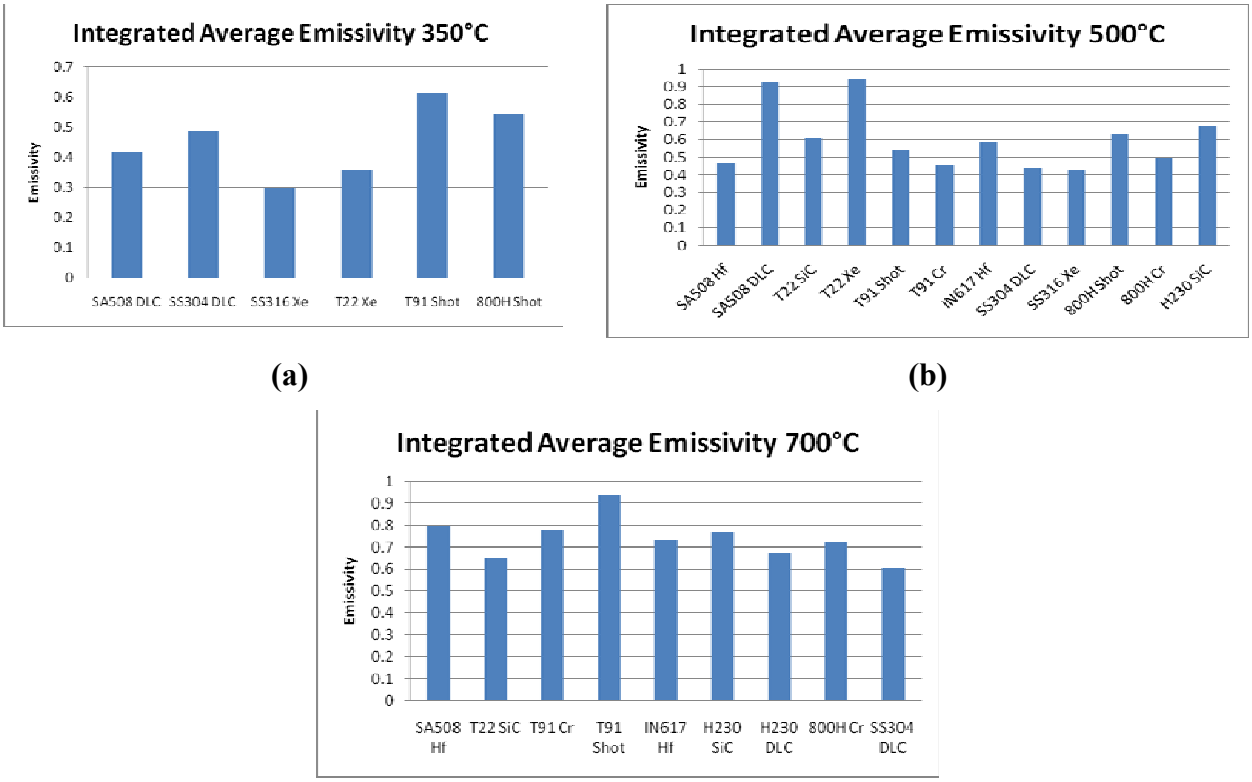

(a) **(b)**

(c)

Figure 110. Summary of integrated spectral emissivity (from 4 μm to 10μm wavelengths) of surface treated alloys at (a) 350°C, (b), 500°C and (c) 700°C.

6. Long Term (250 Hours) Spectral Emissivity Measurements at 500°C

6.1. Introduction

Test samples of candidate alloys and surface treated alloys were exposed in air for 250 hours at 500°C in a furnace. Following this the spectral emissivity of these materials was measured at 500°C in our spectral emissivity measurement system. Once in the spectral emissivity measurement system five measurements were typically taken at intervals of 1 hour. For all practical purposes, these five measurements may be considered as replicate measurements because the samples had already been exposed for 250 hours at 500°C prior to these emissivity measurements. Nevertheless, in each of the spectral emissivity plots in this section we have indicated the data taken for each of the five hours.

6.2. As-Received Alloys

The spectral emissivity of SA508 ferritic steel after exposure for 250 hours at 500°C is shown in Figure 111. The spectral emissivity acquires a value of close unity over the entire range of the wavelengths tested. SEM-EDS analyses (Figure 112 and 113) shows that a uniform Fe-oxide layer about 30μm thick develops on the surface of the steel resulting in high emissivity values.

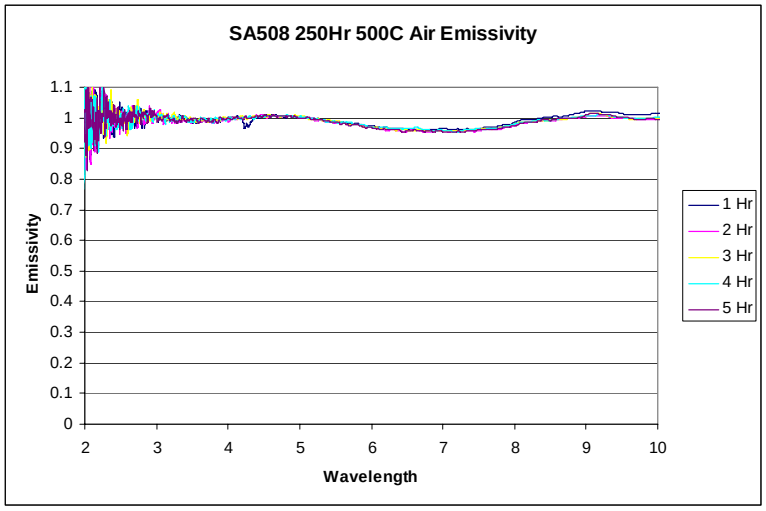

Figure 111. Spectral emissivity for SA508 steel after exposure in air for 250 hours at 500°C

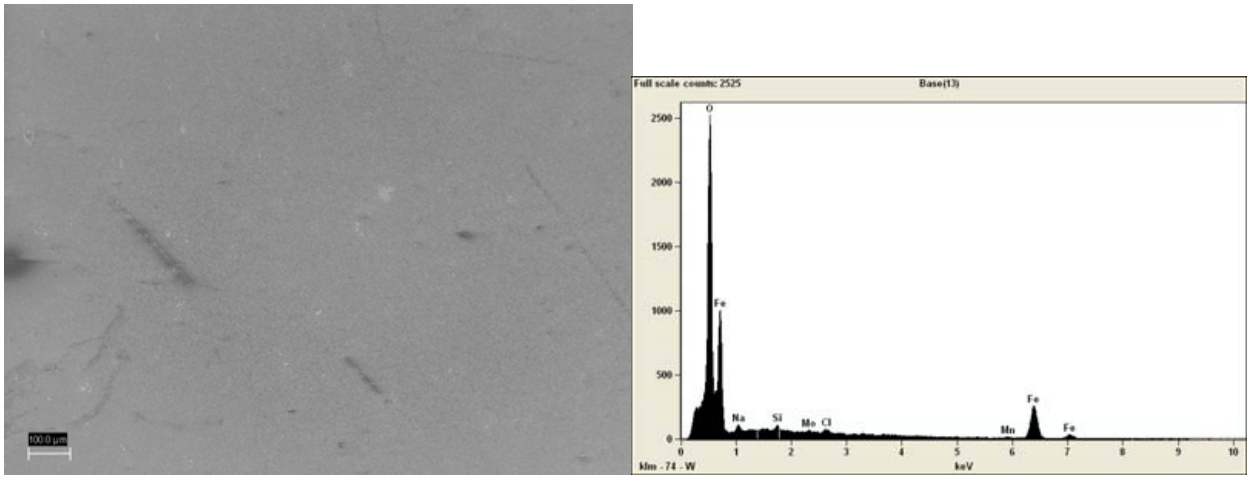

(a) **(b)**

Figure 112. (a) plan view SEM image of SA508 steel after 500°C/250 hours spectral emissivity tests and (b) corresponding elemental EDS spectrum.

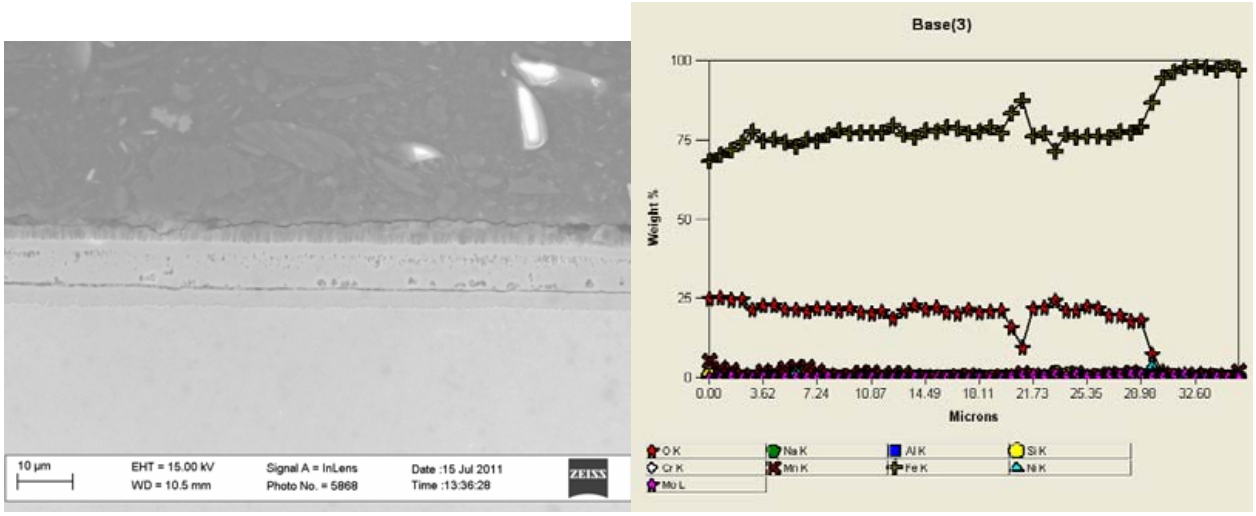

(a) **(b)**

Figure 113. (a) cross-sectional SEM image of SA508 steel after 500°C/250 hours spectral emissivity tests and (b) corresponding EDS line scan across the surface oxide layer.

The spectral emissivity of T22 ferritic steel after exposure for 250 hours at 500^{o}C is shown in Figure 114. The spectral emissivity acquires a value of close unity up to a wavelength of about 6µm, but decreases slightly at higher wavelengths. The undulating trend in emissivity at these higher wavelengths observed at lower exposure times (discussed earlier) is still faintly present. SEM-EDS analyses (Figure 115 and 116) shows the formation of a uniform Fe-oxide layer about 18µm thick and an underlying Fe-Cr spinel oxide layer about 3µm in thickness. The overall oxide layer is thick enough to preclude any contributions of the substrate steel to the overall emissivity.

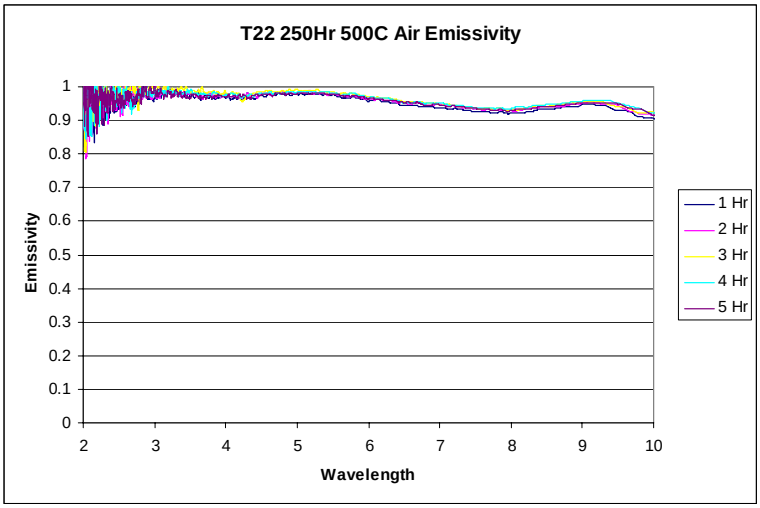

Figure 114. Spectral emissivity for T22 steel after exposure in air for 250 hours at 500°C.

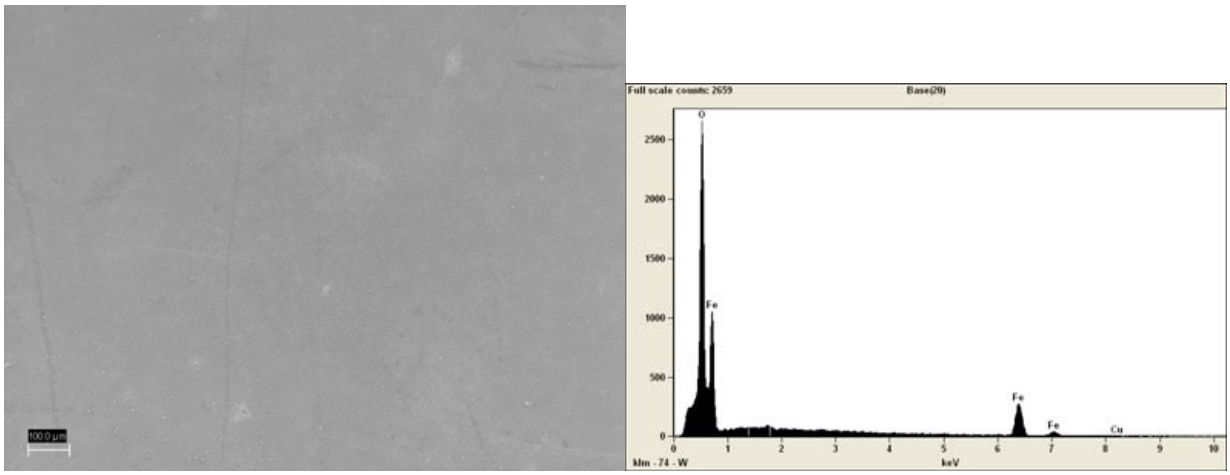

(a) **(b)**

Figure 115. (a) plan view SEM image of T22 steel after 500°C/250 hours spectral emissivity tests and (b) corresponding elemental EDS spectrum.

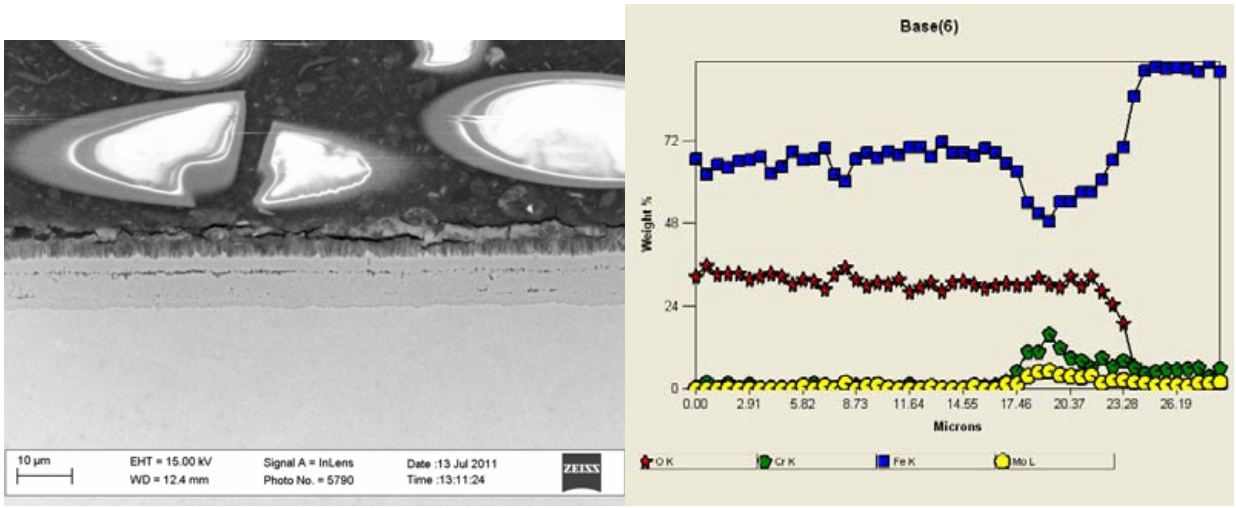

(a) **(b)**

Figure 116. (a) cross-sectional SEM image of T22 steel after 500°C/250 hours spectral emissivity tests and (b) corresponding EDS line scan across the surface oxide layer.

The spectral emissivity of T91 ferritic steel after exposure for 250 hours at 500°C is shown in Figure 117. The emissivity of this steel still maintains a relatively low value of about 0.5. SEM-EDS analyses (Figure 118 and 119) shows the oxide layer to be substantially thinner than those of the two steels discussed earlier predominantly due to the higher Cr content (~9Cr). This high Cr content results in an outer Fe-oxide layer of only 0.3µm in thickness and an underlying Fe-Cr spinel oxide layer about 0.8µm in thickness for a total oxide thickness of about 1.1µm. The thin oxide layer results in a substantial contribution from the underlying steel.

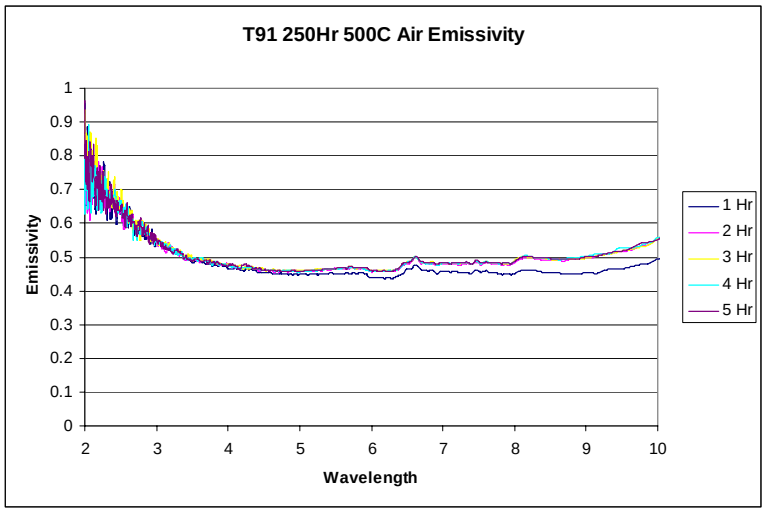

Figure 117. Spectral emissivity for T91 Steel after exposure in air for 250 hours at 500°C.

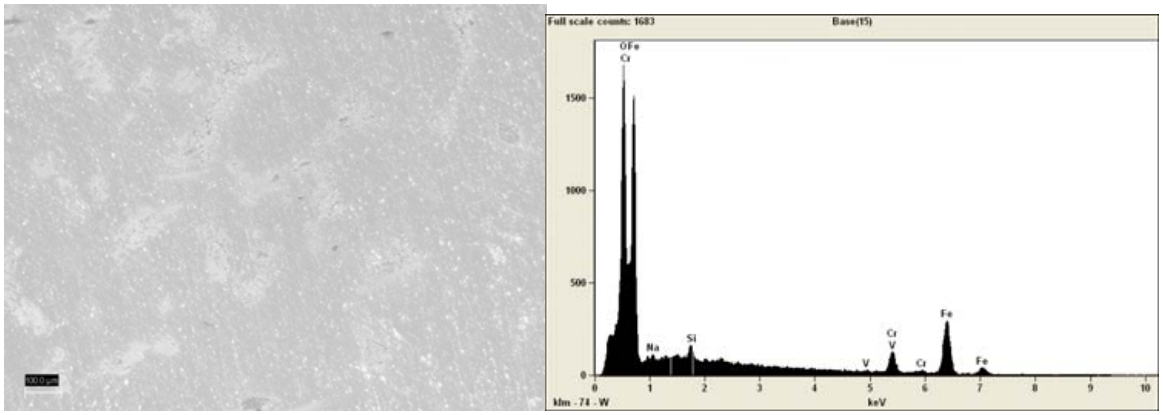

(a) **(b)**

Figure 118. (a) plan view SEM image of T91 steel after 500°C/250 hours spectral emissivity tests and (b) corresponding elemental EDS spectrum.

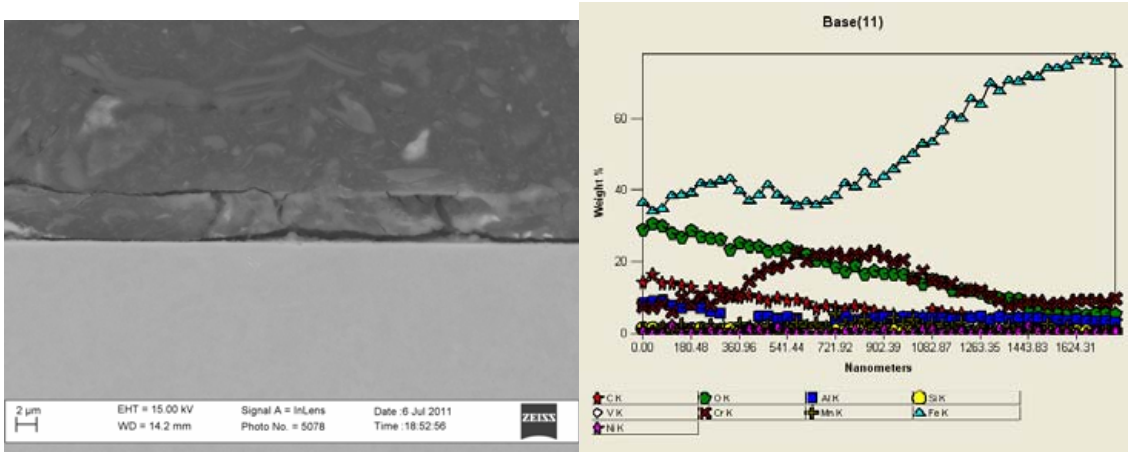

(a) **(b)**

Figure 119. (a) cross-sectional SEM image of T91 steel after 500°C/250 hours spectral emissivity tests and (b) corresponding EDS line scan across the surface oxide layer.

The spectral emissivity of 316 stainless steel after exposure for 250 hours at 500°C is shown in Figure 120. The emissivity of this steel maintains a relatively low value of about 0.5 up to a wavelength of about 5µm, but there is a slight upsurge in emissivity at wavelengths above this value to about 0.6. SEM-EDS analysis (Figure 121 and 122) shows the oxide layer to be thinner than for T91 steel with an outer Fe-oxide layer of only 0.2µm in thickness and an underlying Fe-Cr spinel oxide layer about 0.8µm in thickness for a total oxide thickness of about 1µm. The spinel oxide layer is substantially thicker in this case than for the T91 steel, which is speculated to be the cause for the slightly higher emissivity for this stainless steel at higher wavelengths .

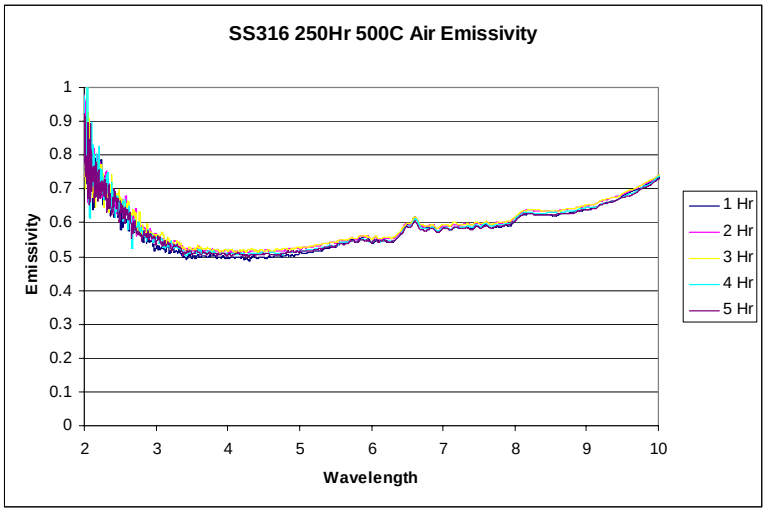

Figure 120. Spectral emissivity for 316 stainless steel after exposure in air for 250 hours at 500°C.

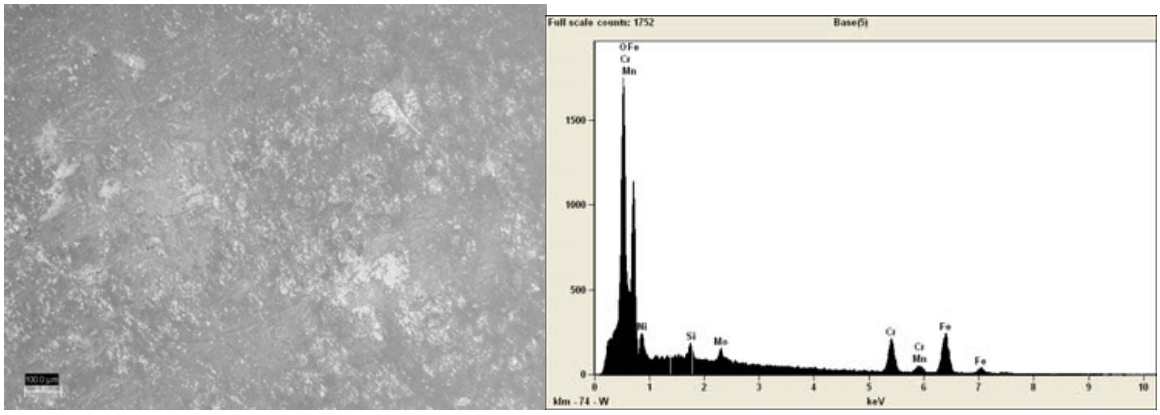

(a) **(b)**

Figure 121. (a) plan view SEM image of 316 stainless steel after 500°C/250 hours spectral emissivity tests and (b) corresponding elemental EDS spectrum.

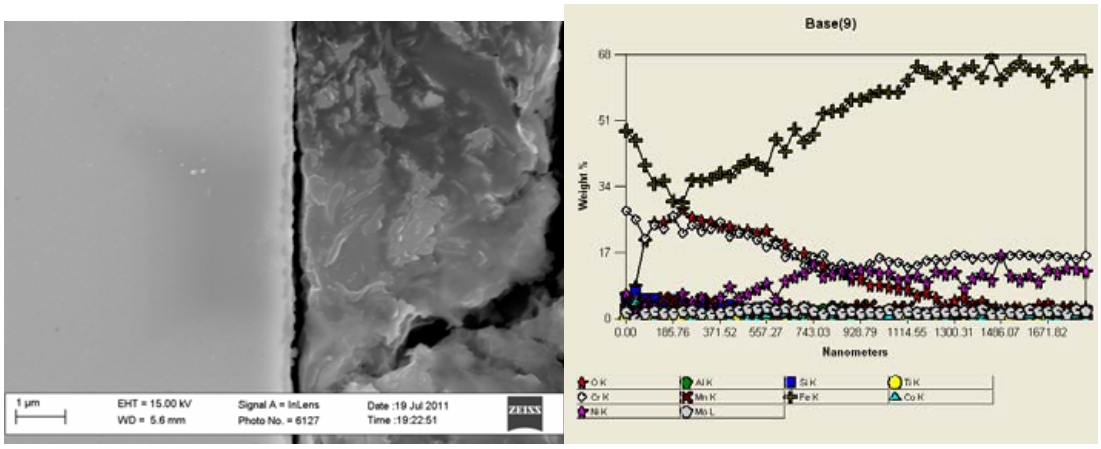

(a) **(b)**

Figure 122. (a) cross-sectional SEM image of 316 stainless steel after 500°C/250 hours spectral emissivity tests and (b) corresponding EDS line scan across the surface oxide layer.

The spectral emissivity of 304 stainless steel after exposure for 250 hours at 500°C is shown in Figure 123. The trends in emissivity are very similar to the 316 stainless steel with lower emissivity values up to about 5µm, and a slight upsurge at higher wavelengths. SEM-EDS analysis (Figure 124 and 125) shows the oxide layer to be 0.8µm in thickness which is thinner than the one observed for 316 stainless steel. The outer layer is about 0.2µm and made up of Fe-rich oxide containing Cr and a small amount of Ni and the underlying oxide layer is a Fe-Cr oxide spinel layer about 0.6µm.

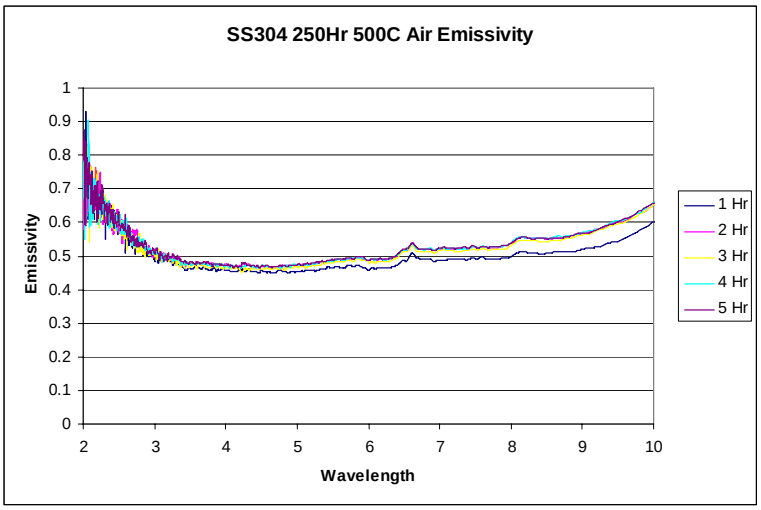

Figure 123. Spectral emissivity for 304 stainless steel after exposure in air for 250 hours at 500°C.

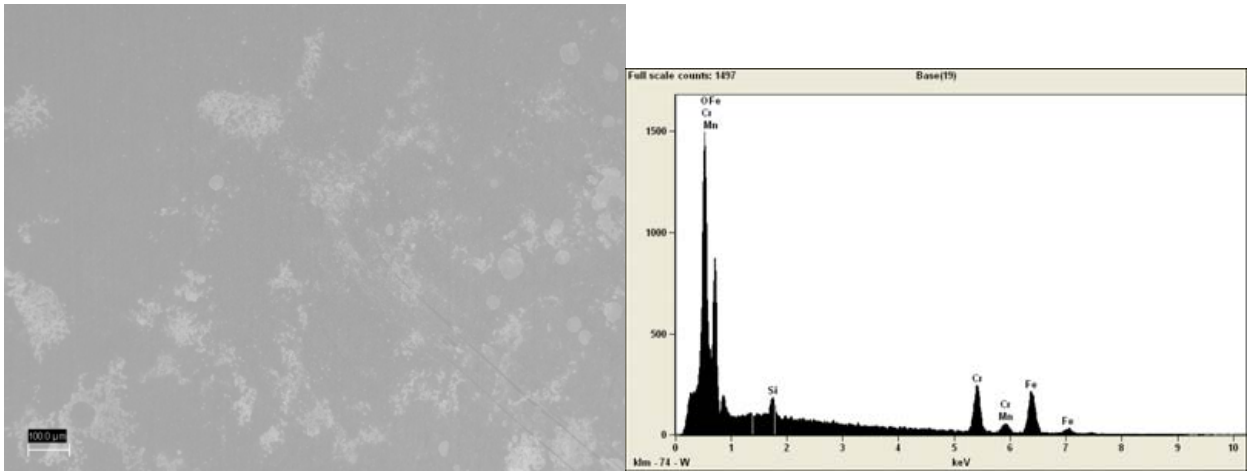

(a) **(b)**

Figure 124. (a) plan view SEM image of 304 stainless steel after 500°C/250 hours spectral emissivity tests and (b) corresponding elemental EDS spectrum.

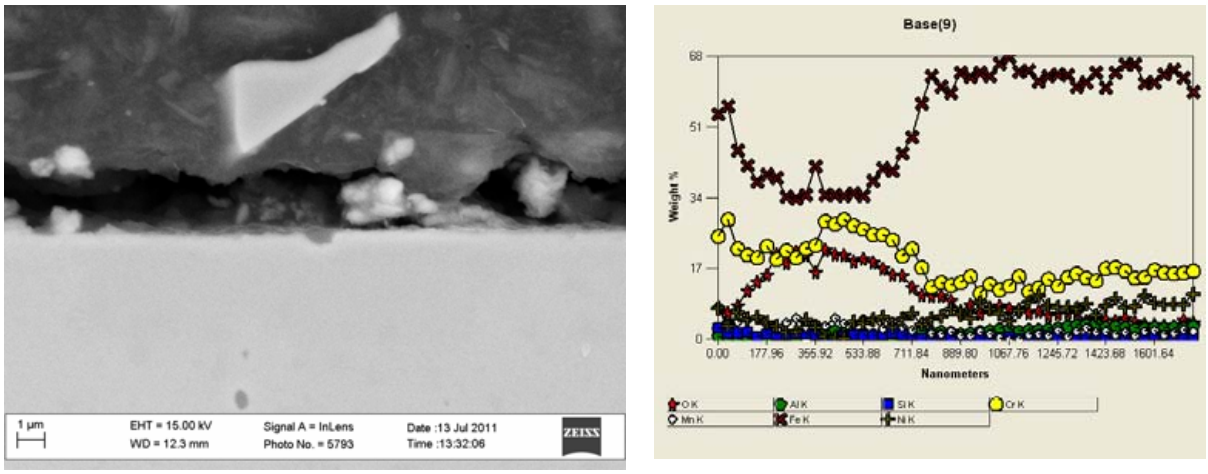

(a) **(b)**

Figure 125. (a) cross-sectional SEM image of 304 stainless steel after 500°C/250 hours spectral emissivity tests and (b) corresponding EDS line scan across the surface oxide layer.

The spectral emissivity of IN800H after exposure for 250 hours at 500°C is shown in Figure 126. The trends in emissivity are similar to 316 and 304 stainless steel with lower emissivity values up to about 5µm, and a slight upsurge at higher wavelengths. SEM-EDS analysis (Figure 127 and 128) shows the oxide layer is about 1.1µm in thickness, and is predominantly Fe-Cr-Ni oxide.

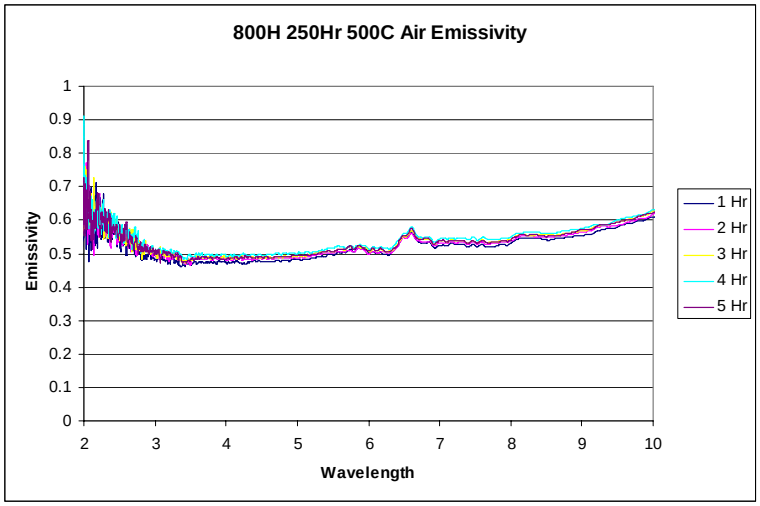

Figure 126. Spectral emissivity for alloy IN800H after exposure in air for 250 hours at 500°C.

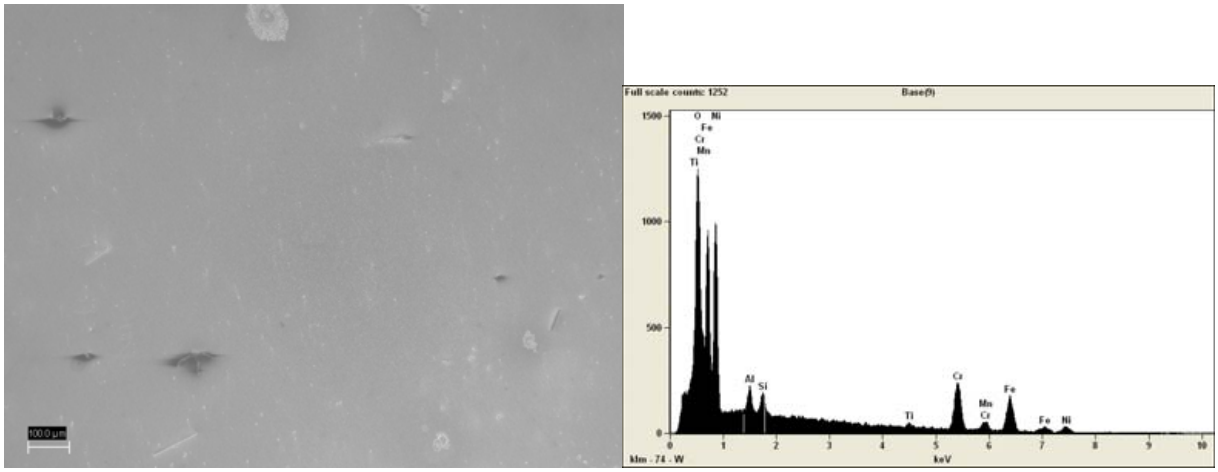

(a) **(b)**

Figure 127. (a) plan view SEM image of alloy IN800H after 500°C/250 hours spectral emissivity tests and (b) corresponding elemental EDS spectrum.

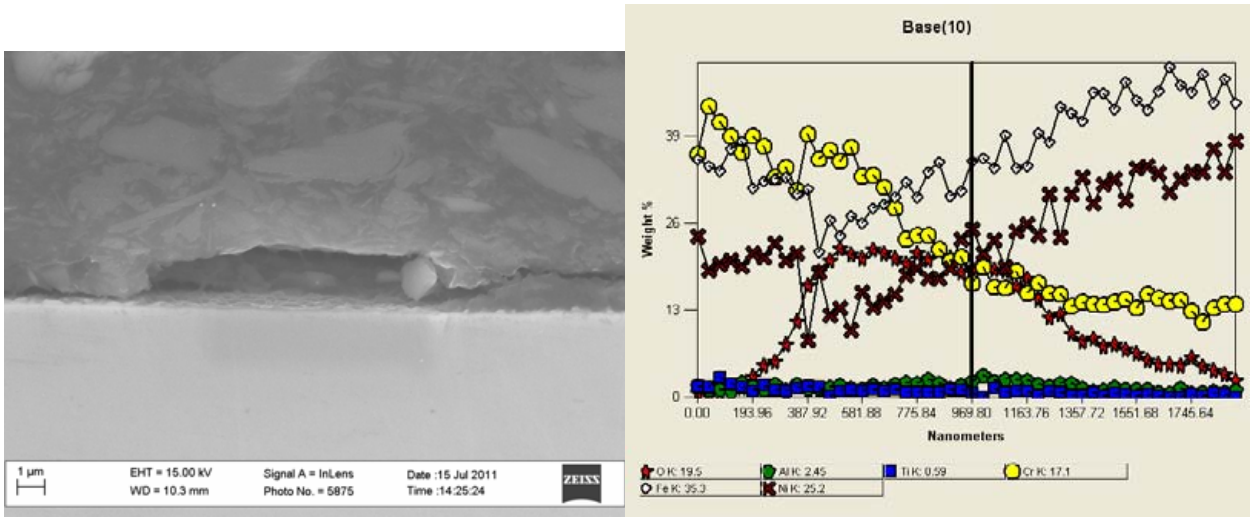

(a) **(b)**

Figure 128. (a) cross-sectional SEM image of alloy IN800H after 500°C/250 hours spectral emissivity tests and (b) corresponding EDS line scan across the surface oxide layer.

The spectral emissivity of Haynes 230 after exposure for 250 hours at 500°C is shown in Figure 129. The spectral emissivity of this alloy is generally lower than IN800H with values below 0.4 up to about 5µm and increasing gradually to about 0.5 at about 9 µm. SEM-EDS analysis (Figure 130 and 131) shows the oxide layer to be only about 0.6µm in thickness, and consisting of Cr-Ni oxide with W. Since the oxide layer is so thin, the overall observed emissivity includes significant contributions from both the base alloy and the oxide.

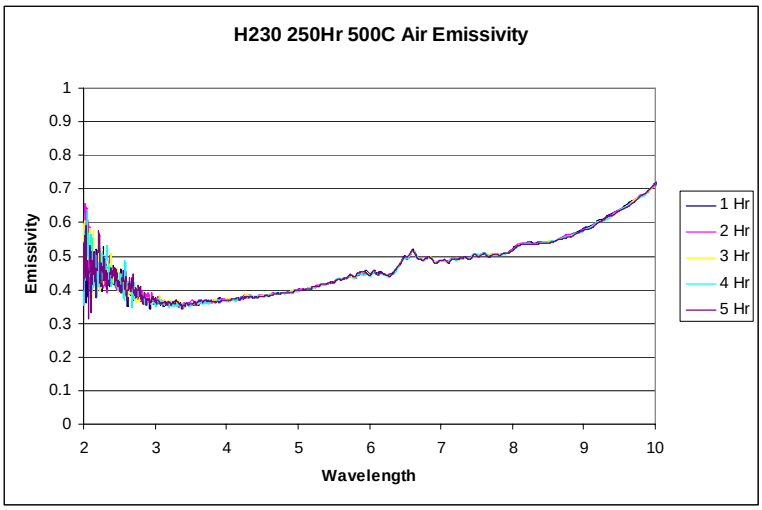

Figure 129. Spectral emissivity for Haynes 230 alloy after exposure in air for 250 hours at 500°C.

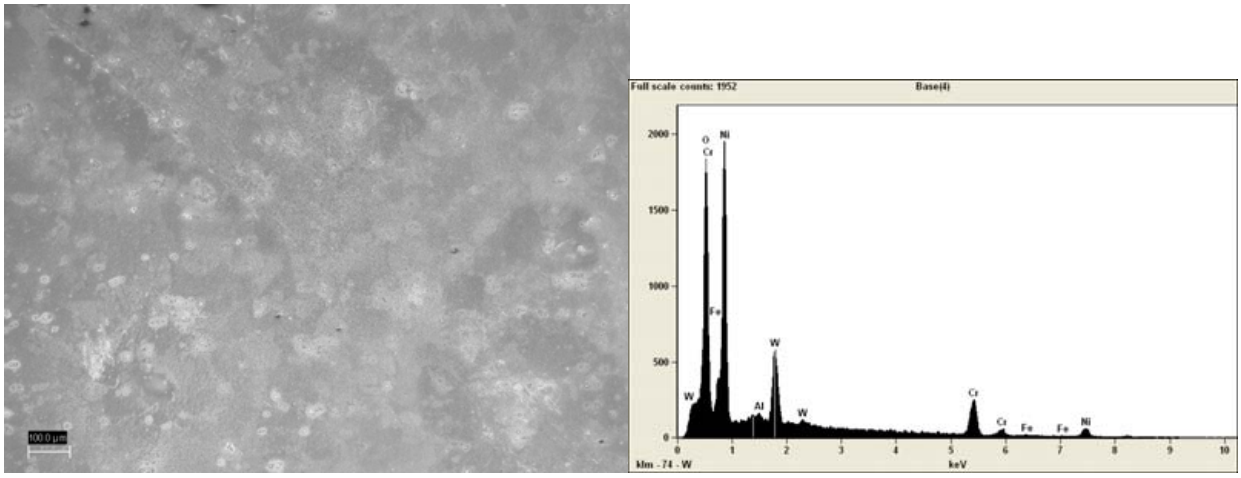

(a) **(b)**

Figure 130. (a) plan view SEM image of Haynes 230 alloy after 500°C/250 hours spectral emissivity tests and (b) corresponding elemental EDS spectrum.

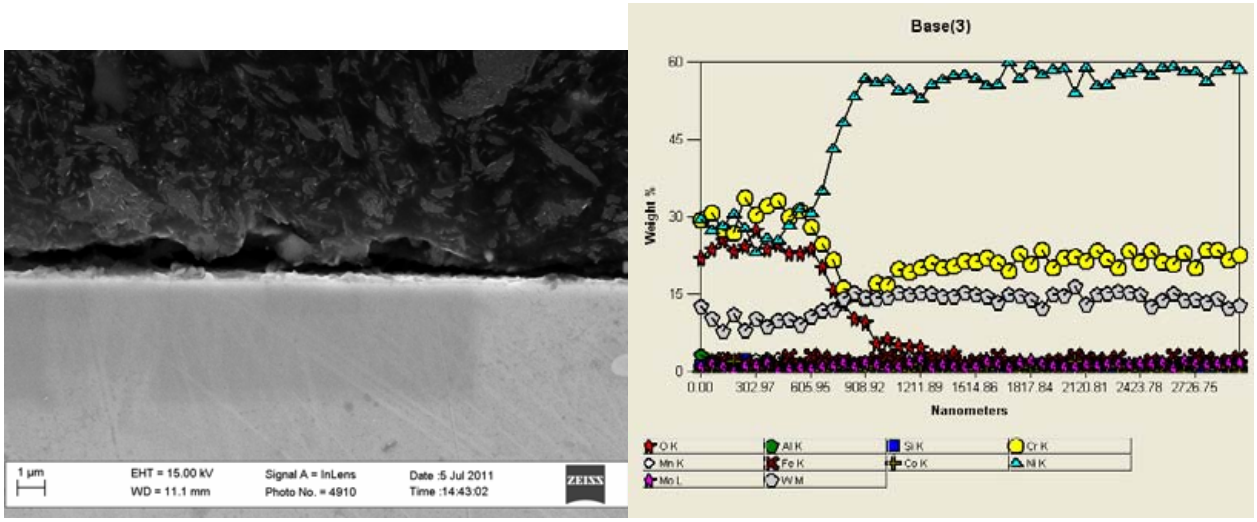

(a) **(b)**

Figure 131. (a) cross-sectional SEM image of Haynes 230 alloy after 500°C/250 hours spectral emissivity tests and (b) corresponding EDS line scan across the surface oxide layer.

6.3. Surface Treated Alloys

The spectral emissivity of DLC coated SA508 ferritic steel after exposure for 250 hours at 500°C is shown in Figure 132. The spectral emissivity attains a high value of near unity and very similar to the uncoated SA508 steel tested for 250 hours at 500°C. SEM-EDS analysis (Figure 133 and 134) shows the oxide layer to be about 32μm in thickness, and consists of Fe-oxide magnetite. The oxide layer is slightly thicker than the 30μm develops that on uncoated SA508. As noted earlier in this report at these temperatures, it is likely that the DLC film sublimated as a result of reaction with air.

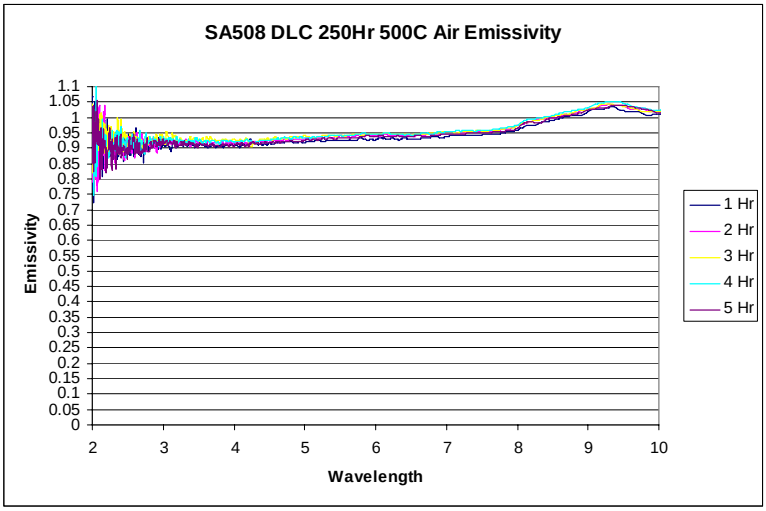

Figure 132. Spectral emissivity for DLC-surface treated SA508 steel after exposure in air for 250 hours at 500°C.

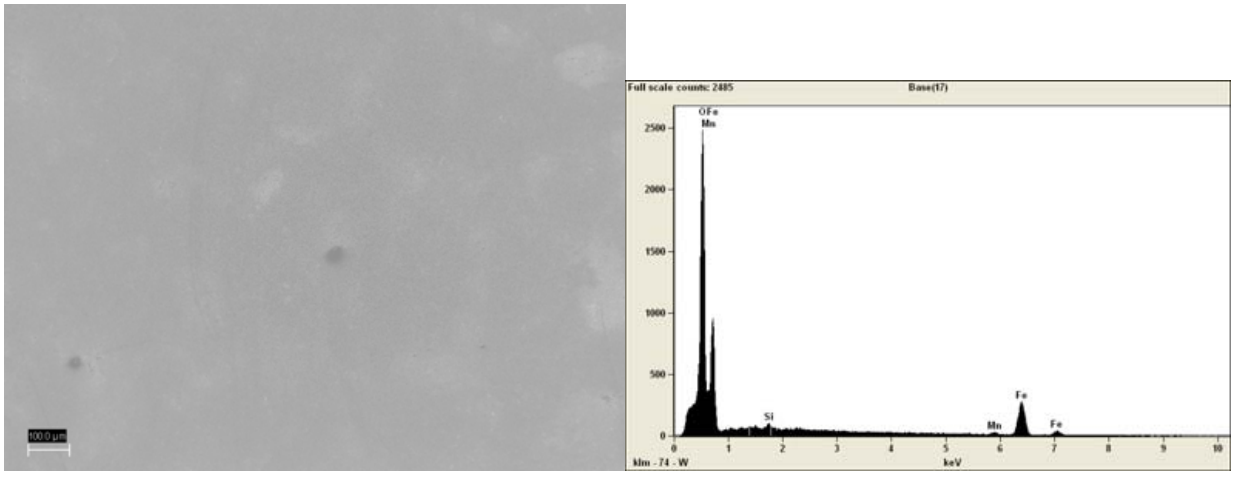

(a) **(b)**

Figure 133. (a) plan view SEM image of DLC-surface treated SA508 steel after 500°C/250 hours spectral emissivity tests and (b) corresponding elemental EDS spectrum.

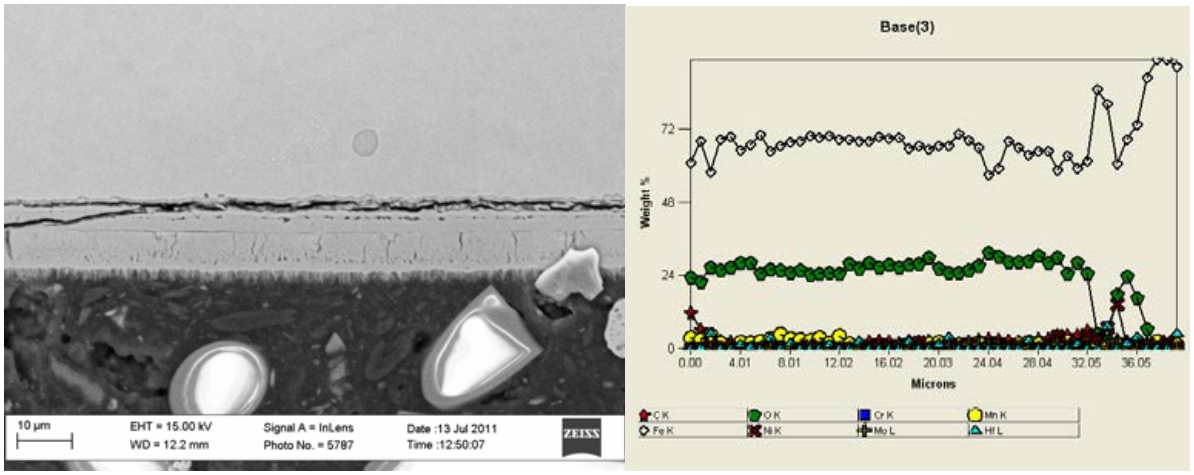

(a) **(b)**

Figure 134. (a) cross-sectional SEM image of DLC-surface treated SA508 after 500°C/250 hours spectral emissivity tests and (b) corresponding EDS line scan across the surface oxide layer.

The spectral emissivity of SiC coated Haynes 230 after exposure for 250 hours at 500°C is shown in Figure 135. The spectral emissivity of this alloy shows trends very similar to those obtained with SiC coated Haynes 230 after exposure to elevated temperature just for 5 hours, indicating that the SiC coating is very protective. SEM-EDS analysis (Figure 136 and 137) shows penetration of oxygen to a depth of about 0.4µm in thickness, and some diffusion of Ni and Cr from the base alloy into the SiC. Nevertheless this coating still maintains the same spectral emissivity trends as the original SiC coating.

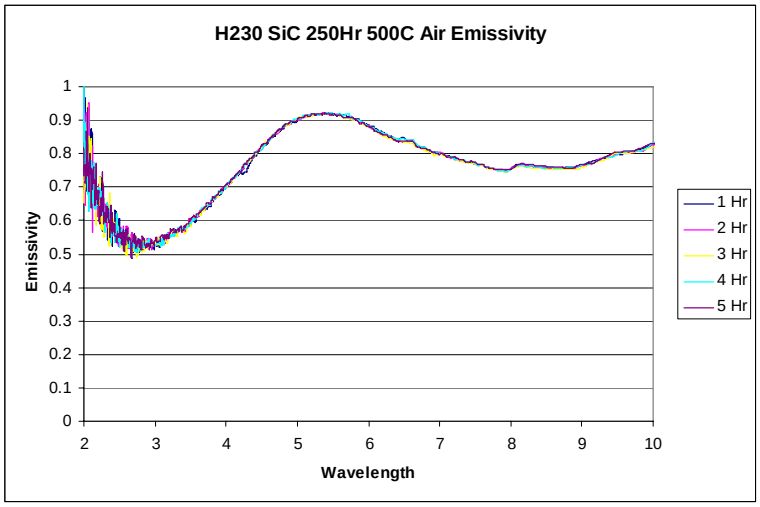

Figure 135. Spectral emissivity for SiC-surface treated Haynes 230 alloy after exposure in air for 250 hours at 500°C.

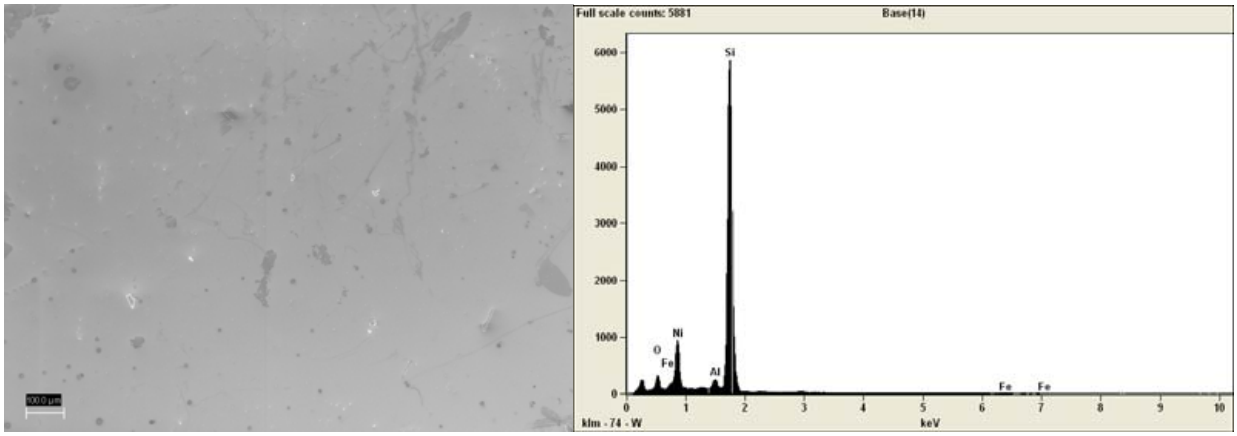

(a) **(b)**

Figure 136. (a) plan view SEM image of SiC-surface treated Haynes 230 alloy after 500°C/250 hours spectral emissivity tests and (b) corresponding elemental EDS spectrum.

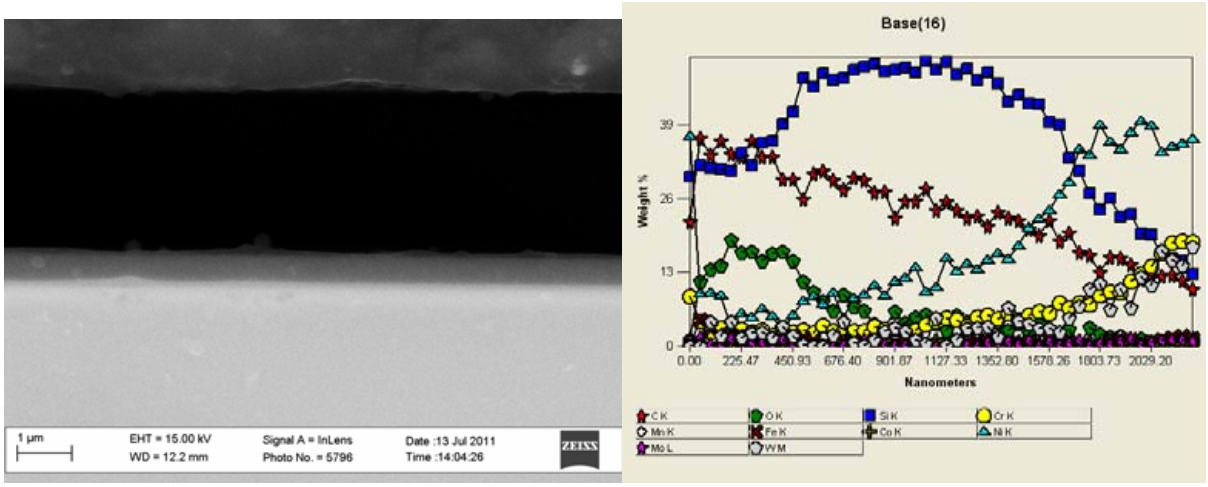

(a) **(b)**

Figure 137. (a) cross-sectional SEM image of SiC-surface treated Haynes 230 alloy after 500°C/250 hours spectral emissivity tests and (b) corresponding EDS line scan across the surface oxide layer.

The spectral emissivity of Xe ion bombarded T22 ferrtic steel after exposure for 250 hours at 500^{o}C is shown in Figure 138. The spectral emissivity of this alloy shows trends very similar to those obtained with the untreated T22 steel in that the emissivity values attain a high value close to unity. SEM-EDS analysis (Figure 139 and 140) shows penetration of oxygen to a depth of about 26µm in thickness, which is slightly thicker than that observed for untreated T22 ferritic steel. Thus the Xe ion bombardment does not appear to have any significant effect on the long-term emissivity of T22 ferritic steel.

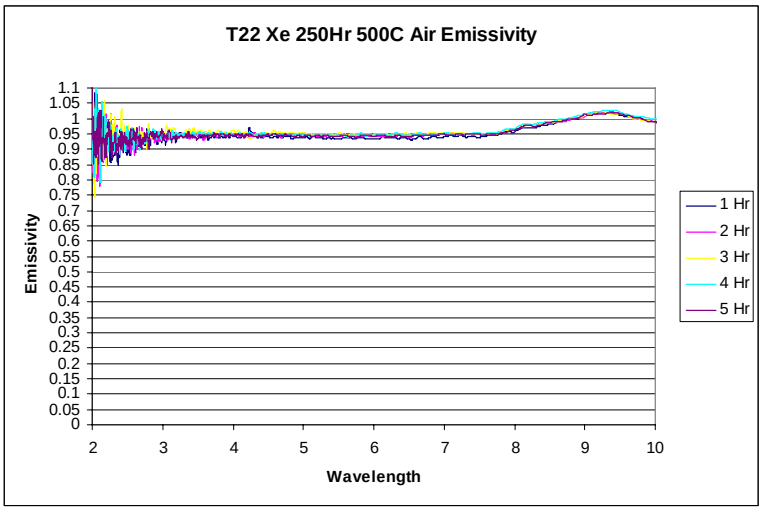

Figure 138. Spectral emissivity for Xe+ bombarded surface treated T22 steel after exposure in air for 250 hours at 500°C.

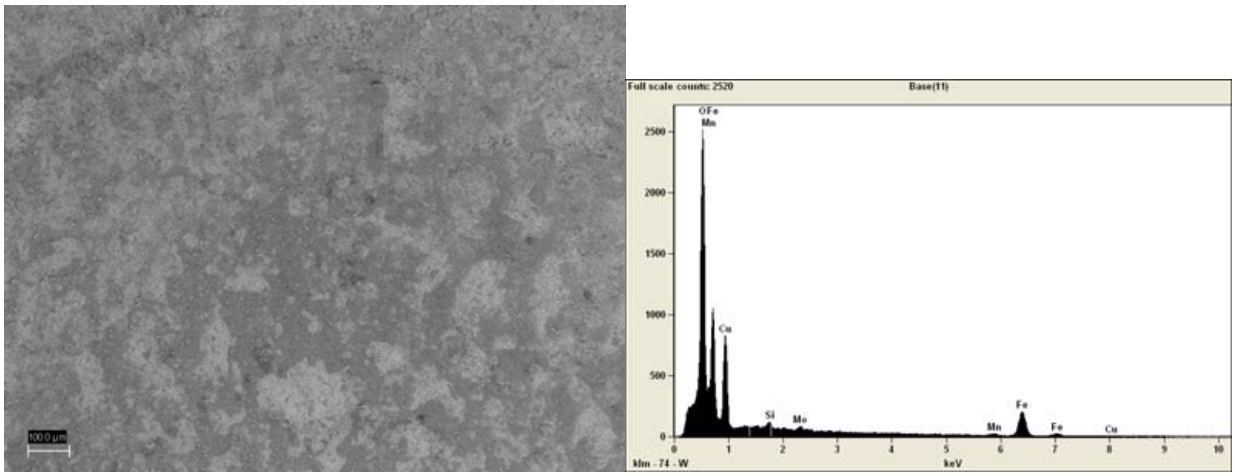

(a) **(b)**

Figure 139. (a) plan view SEM image of Xe+ bombarded surface treated T22 steel after 500°C/250 hours spectral emissivity tests and (b) corresponding elemental EDS spectrum.

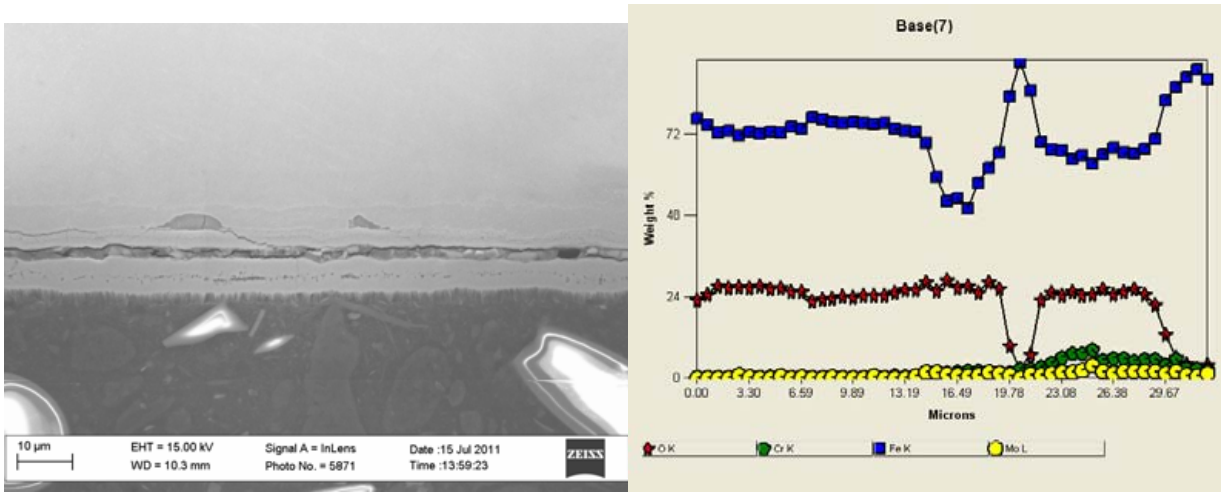

(a) (b)

Figure 140. (a) cross-sectional SEM image of Xe+ bombarded surface treated T22 steel after 500°C/250 hours spectral emissivity tests and (b) corresponding EDS line scan across the surface oxide layer.

The spectral emissivity of Cr film deposited T91 ferritic steel after exposure for 250 hours at 500°C is shown in Figure 141. At a value of about 0.6, the emissivity of this Cr-coated T91 steel is slightly higher than uncoated T91 steel which has a value of about 0.5. SEM-EDS analyses (Figure 142 and 143) shows the Cr layer to be largely intact at the surface. The Cr film has as oxidized and the higher emissivity is attributed to the formation of Cr-oxide at the surface. There is no evidence of Fe diffusion from the underlying steel through the Cr film. We were surprised to note that the Cr film as observed and measured by SEM-EDS analysis is thicker than we had originally intended to deposit, but nevertheless this experiment shows that the sputter deposited Cr layer provides remarkable oxidation protection and hence the ability to control emissivity of the surface of T91 steel.

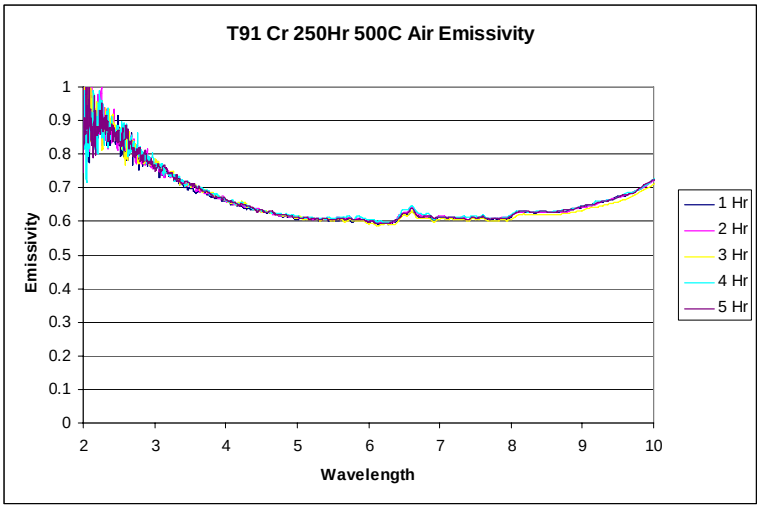

Figure 141. Spectral emissivity for Cr-surface treated T91 steel after exposure in air for 250 hours at 500°C.

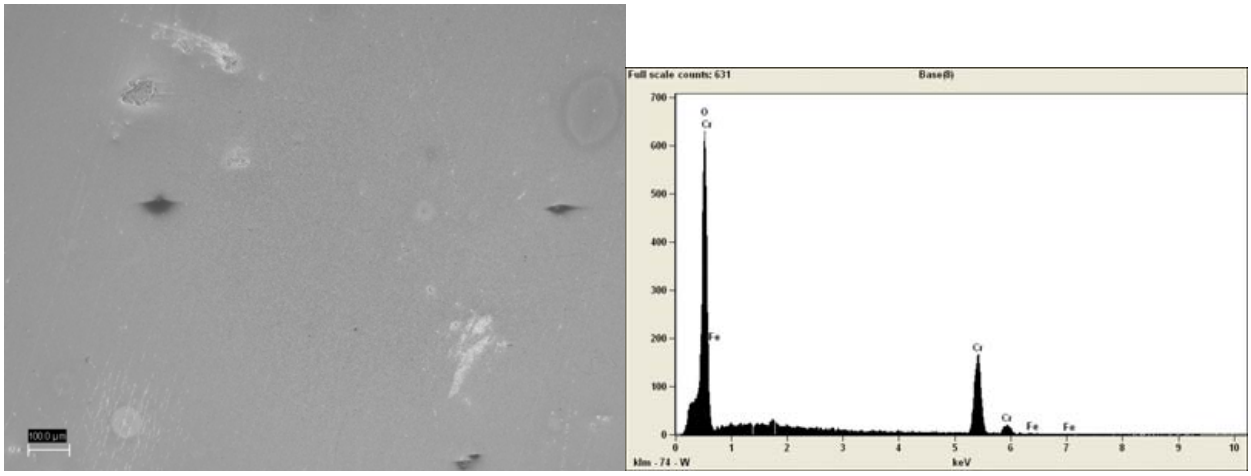

(a) **(b)**

Figure 142. (a) plan view SEM image of Cr-surface treated T91 steel after 500°C/250 hours spectral emissivity tests and (b) corresponding elemental EDS spectrum.

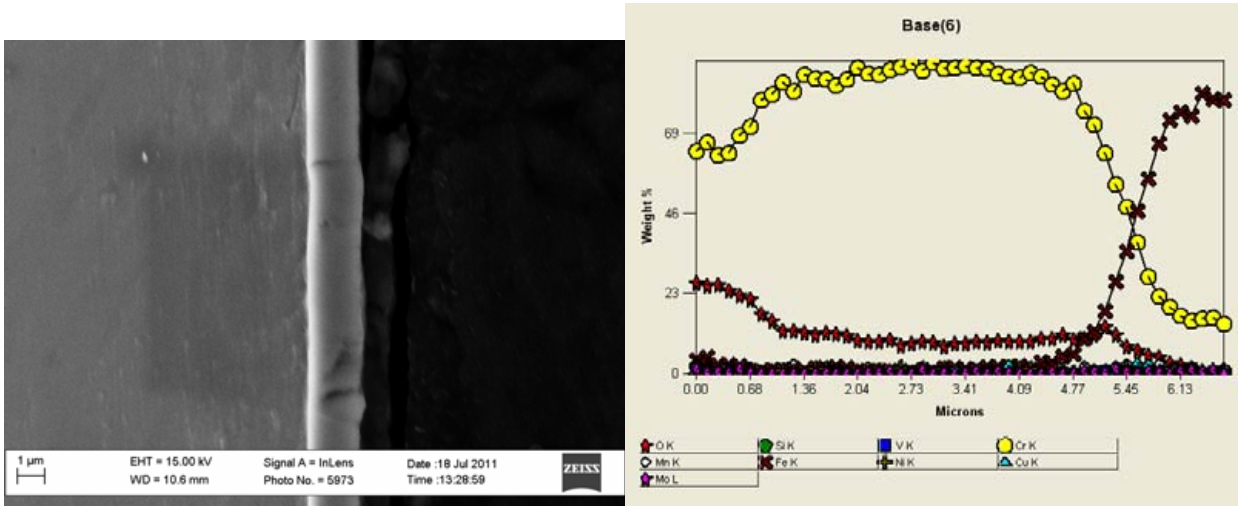

(a) **(b)**

Figure 143. (a) cross-sectional SEM image of Cr-surface treated T91 steel after 500°C/250 hours spectral emissivity tests and (b) corresponding EDS line scan across the surface oxide layer.

The spectral emissivity of Hf thin film deposited SA508 ferritic steel after exposure for 250 hours at 500^{o}C is shown in Figure 144. The spectral emissivity approaches a value of about 0.85, but it is still lower than observed for the uncoated SA508 where the values were close to unity. SEM-EDS analyses (Figure 145 and 146) shows that the Hf film provides remarkable protection against oxidation. Oxygen diffusion has occurred in the near surface region of the Hf film and there is no diffusion of Fe into the Hf film. The emissivity measured is a combination of the thin hafnium-oxide layer and the underlying unreacted Hf.

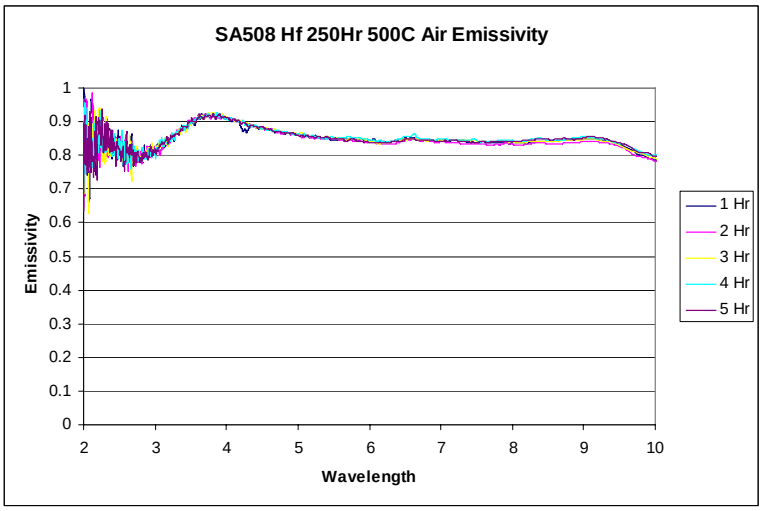

Figure 144. Spectral emissivity for Hf-surface treated SA508 steel after exposure in air for 250 hours at 500°C.

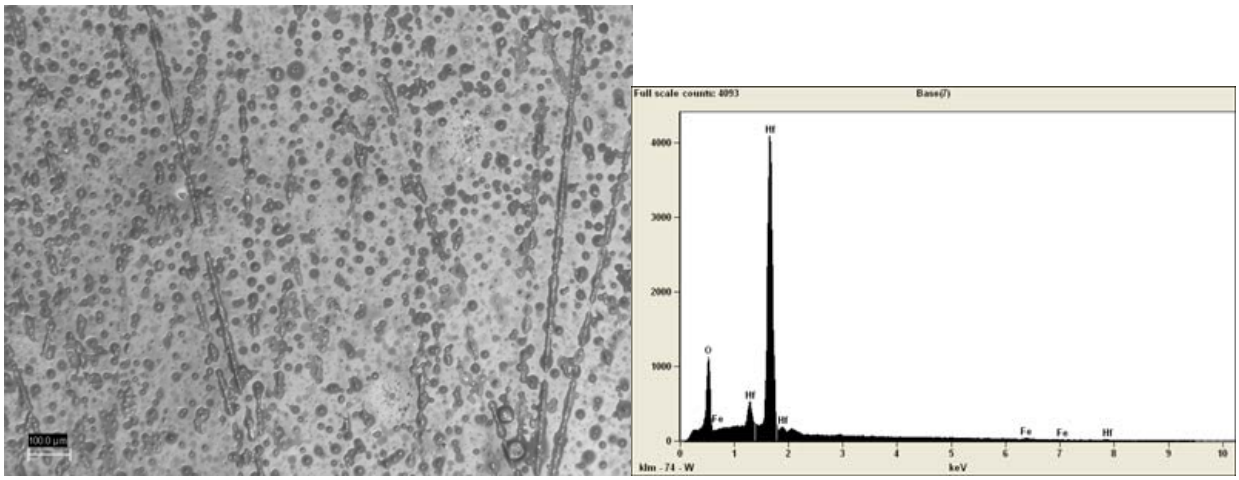

(a) **(b)**

Figure 145. (a) plan view SEM image of Hf-surface treated SA508 steel after 500°C/250 hours spectral emissivity tests and (b) corresponding elemental EDS spectrum.

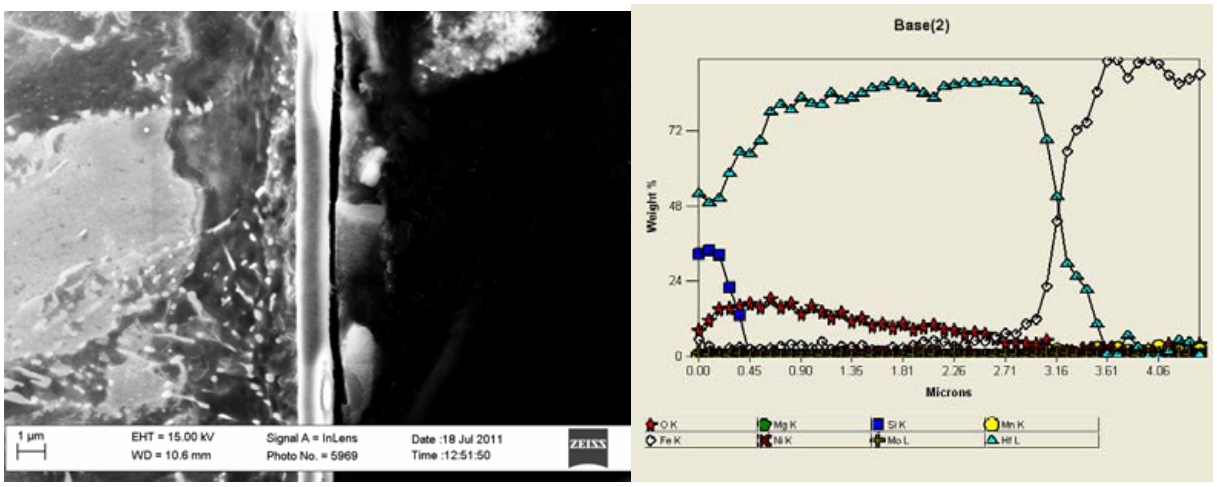

(a) **(b)**

Figure 146. (a) cross-sectional SEM image of Hf-surface treated SA508 steel after 500°C/250 hours spectral emissivity tests and (b) corresponding EDS line scan across the surface oxide layer.

6.3. Summary of 500°C/250 hour Emissivity Tests

Figure 147 and 148 show the data for spectral emissivity measurements of many of the as-received alloys after the 500°C/250hour tests. The values indicated in each of these plots include: (a) the integrated emissivity over 6µm to 10µm wavelengths, (b) the peak emissivity value, and (c) wavelength at which the peak emissivity occurs. Based on the discussions in the earlier part of this section, it is appears that certain surface treatments such as SiC coating, and Cr and Hf sputter deposition can be used to control the long-term emissivity of steels. For example, SiC caooting can be used to enhance the spectral emissivity of austenitic high temperature alloys whereas treatments such as Cr and Hf surface treatments can be used mitigate the precipitous increases in emissivity due to the development of thick oxide layers.

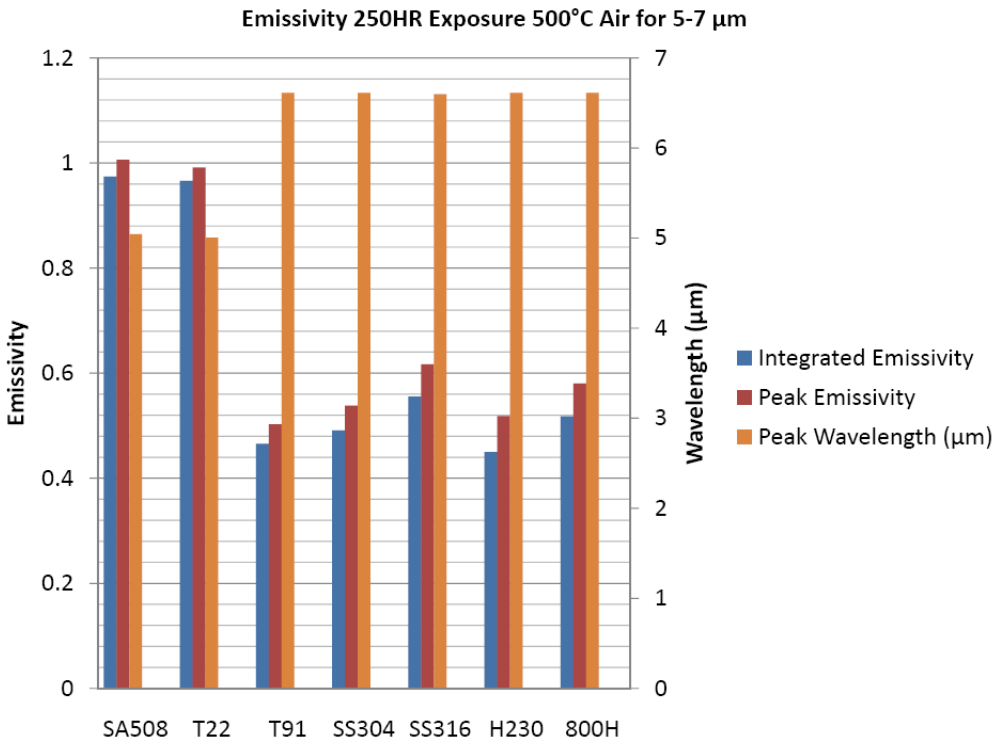

Figure 147. Summary of spectral emissivity data from various alloys after the 500°C/250 hour tests.

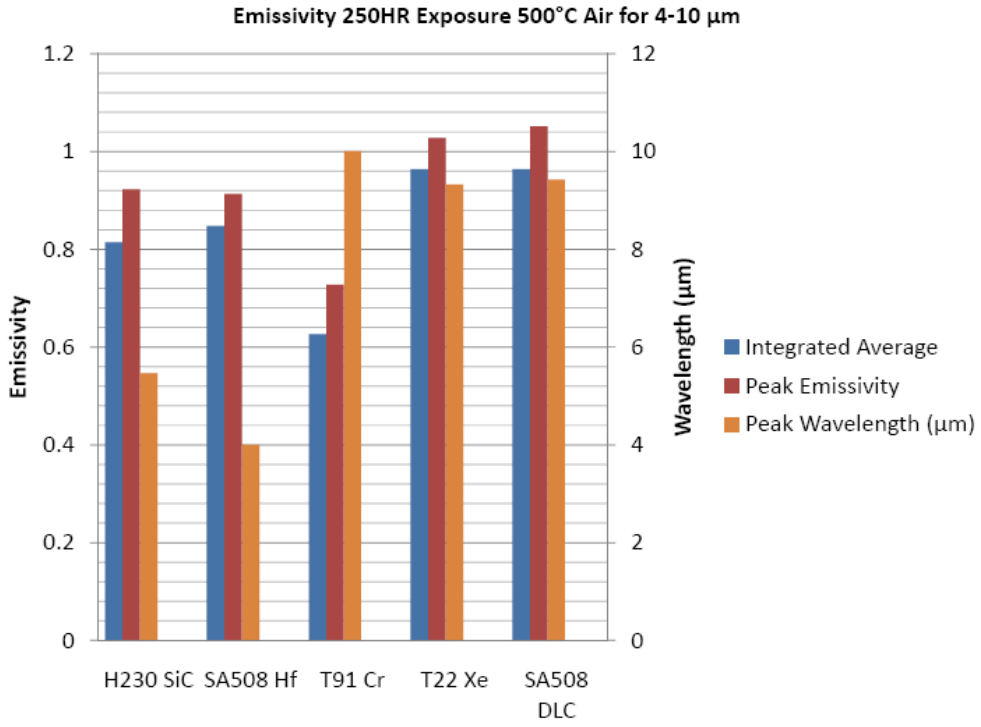

Figure 148. Summary of spectral emissivity data from various surface treated alloys after the 500°C/250 hour tests.

7. Numerical Simulation of Emissivity – A Preliminary Approach

7.1. Background of Concepts:

Although not the primary goal of this project, some numerical modeling of spectral emissivity has been initiated in this project which we would be beneficial to future researchers.

The numerical computer modeling efforts use Monte Carlo sampling of emission angle and position for a sample and a blackbody to determine spectral sample emissivity from the optics constant and extinction coefficient of the sample and oxide layers. Of particular interest are the cutoff at which further oxide thickness does not affect emissivity. Surface topology is taken as flat. The oxide is assumed to be composed of a thin layer of Cr_2O_3 and Fe_2O_3 below a thicker layer of Fe_3O_4, as many of the steels of interest contain some chromium. The code could be modified to calculate angular emissivity instead, but the goal here was also to determine effects due to the ratio of sample size and mirror size, allowing for a greater understanding of some of the parameters in the experimental determination of emissivity.

The assumptions required for this model include that none of the materials are conducting (allows the permeability of each material to be assumed to be μ_o) and that all surfaces are perfectly flat. The non-conduction assumption is clearly not perfect because the metallic substrate does conduct, but the oxide layers do not conduct and are the most important for this calculation. Furthermore, it is standard procedure to assume non-conducting materials [43-51]. Assuming that all surfaces are perfectly flat allows the use of relatively simple Maxwell equations for photon transport instead of requiring an atomistic simulation to take into account the contributions of the surface atoms.

For thin layers of oxides, the emissivity is primarily a function of diffraction in the oxide film. Oxides are typically transparent in the infrared region, so the photons emitted from the substrate metal are partially transmitted through the oxide layer. At the interfaces, the light is diffracted, allowing only some wavelengths through. For larger oxide thicknesses, the photons emitted by the substrate metal are completely absorbed and the emission is dependent entirely on the oxide emissivity.

Because positive z is generally assumed to point down in literature of electromagnetic wave refraction and diffraction, the coordinate system follows this convention for initial calculations. The final equations only require heights and therefore the more normal convention of positive z going up is assumed elsewhere in the computer model.

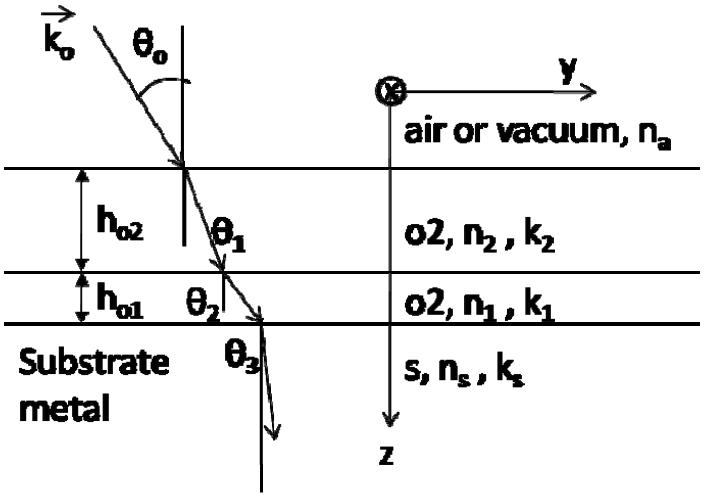

Figure 149. Schematic of refractions that determine emission angle.

Using Maxwell's electromagnetic equations the reflection from each layer is calculated, as illustrated in Figure 150. The resulting reflection coefficients (R) are then used to calculate the total reflectivity of the surface. From the total reflectivity, the emissivity is calculated using $\varepsilon = 1 - R^2$ for both the electric and magnetic wave vectors composing the photon. The total emissivity is then obtained by averaging the electric and magnetic emissivities.

For simplicity, the source term is constant across all wavelengths. The emission intensity should drop off at both high and low wavelengths, in accordance with a blackbody emission curve. Keeping the source constant across wavelengths is not physical, but does give all wavelengths the same statistical variance.

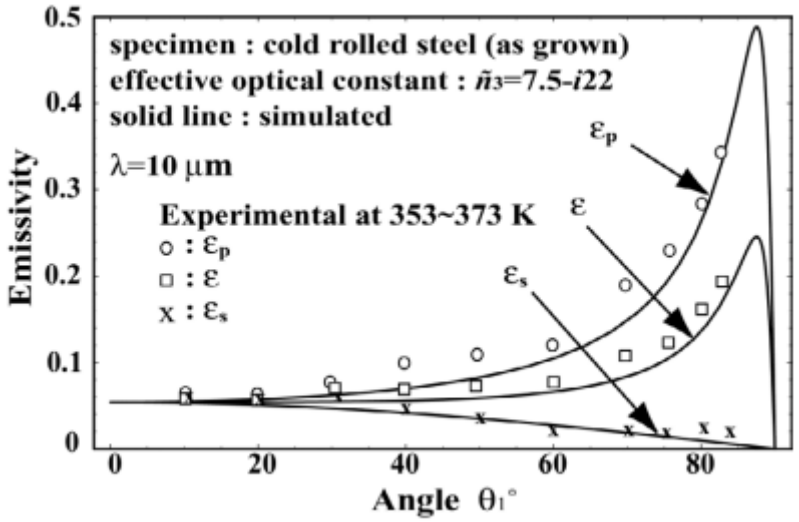

Figure 150. The angular emission curve for 5.8nm thick oxide layer.

The emission angle for the sample needs to be sampled from a function that acts as a PDF, similar to that shown in Figure 151. The sampling function is not a PDF because it does not integrate to one; however, this non-integration to one is a desired characteristic. The definition of emissivity requires that any real material emit less radiation at every wavelength than a blackbody. The blackbody is uniformly sampled from 0 to $\pi/2$, so in order to ensure that the

sample has fewer emissions, some possible emissions must be thrown out. First, the location of emission is sampled. The sample is assumed to be homogeneous and therefore the sample area should be uniformly sampled.

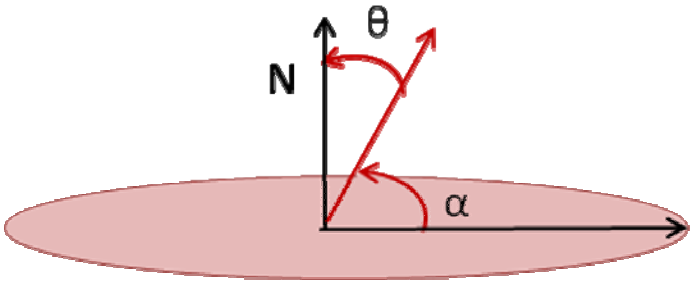

Figure 151. The emission angles, theta is the primary angle and alpha is the azmuthial angle.

The most complex part of the calculation is sampling the emission angle of the sample. A primary emission angle is selected from a uniform random distribution on 0 to π/2, with a second angle describing the azmuthial emission direction selected from a uniform random distribution on 0 to π/2 (see Figure 152). The emission vector is traced back to the surface metal. This calculation is relatively simple because Snell's Law, $n_1 \cdot \sin\theta_1 = n_2 \cdot \sin\theta_2$, directly calculates each of the refraction angles.

Finally, the emissivity of that particular location and that particular emission angle is calculated. The sample emits less than a blackbody and the emission angle PDF is similar to that of Figure 150, so not all angles are accepted. Another random number, ξ is selected. If the calculated emissivity is less than that of ξ, the angle θ is accepted. If the emissivity is less than ξ, then θ is rejected. This rejection represents a situation when the sample does not emit even though a blackbody would have. The emission vector is then used to calculate whether the emission would reach a target a set distance above the sample, as shown in Figure 152. The location and dimension of the target was selected to match the experimental geometry as closely as possible.

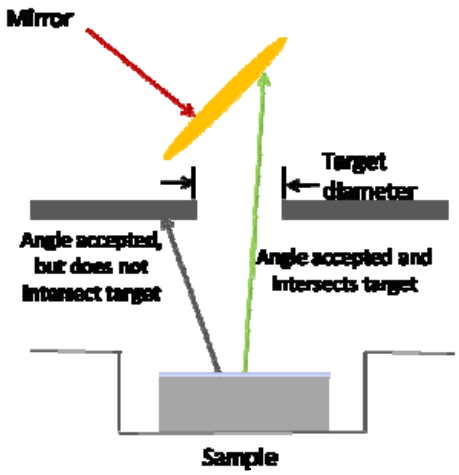

Figure 152. The emission gets counted if it would hit the mirror.

A similar procedure is followed for the blackbody except the emission angle is sampled uniformly on 0 to π/2, as a perfect blackbody would emit isotropically [52]. The blackbody does

not have oxide layers and has an emissivity of one, so all sampled angles are accepted. Then it is determined whether the blackbody emission would intercept a target of the same size and location as the sample target. Calculation of the total emissivity of the sample is determined by dividing the number of hits from the sample by the number of hits from the blackbody. Using this ratio method instead of simply calculating the emissivity based on theta allows modeling of more complex surface topology and gives a better idea of how the sample and blackbody geometry affect the flux incident the target. All calculation steps are repeated for each wavelength of interest.

7.2. Preliminary Spectral Emissivity Modeling

Initial modeling results are shown in Figure 153. The oxide is a 100 nm layer of Fe_2O_3 below a 100 nm layer of Fe_3O_4; the experimental data is of mirror-polished T91 at 700°C. The optics constants used in this model are at room temperature, so deviation of the modeled results from the experimental emissivity between 3 μm and 9 μm is likely partially due to temperature dependence in the values of the optics constants. Additionally, the oxide on T91 is likely to contain significant amounts of chromium, which would raise the emissivity in the intermediate wavelength region because the index of refraction of chromia is lower than that of hematite (2.08 versus 2.5) between 3 μm and 9 μm. These differences will need to be incorporated into more advanced models.

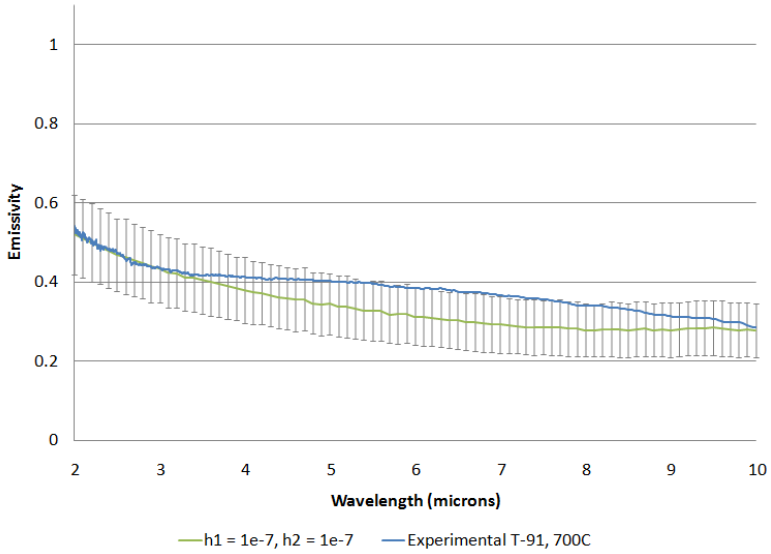

Figure 153. Modeled spectral emissivity for thin oxide layers (green with grey error bars) compared to experimental spectral emissivity of T91 at 700°C (blue). h1 and h2 are the assumed thicknesses of the Fe_2O_3 and Fe_3O_4 layers in meters (the films are assumed to be 100nm each in thickness)

Another example of our modeling efforts is shown in Figure 154. Here, we have assumed that a 0.1μm-thick hematite (Fe_2O_3) oxide layer forms on the surface of the steel and then an outer magnetite (Fe_3O_4) layer is 'numerically' grown to thicknesses of 0.1, 0.5, 1, and 2 μm thickness and the spectral emissivity is modeled. In reality, this scenario is quite typical of ferritic steels, where the outer oxide layer consists of a fast growing magnetite layer and a thin inner hematite oxide layer maintains a relatively low thickness. As expected, the spectral emissivity increases as the magnetite oxide layer grows to greater thicknesses.

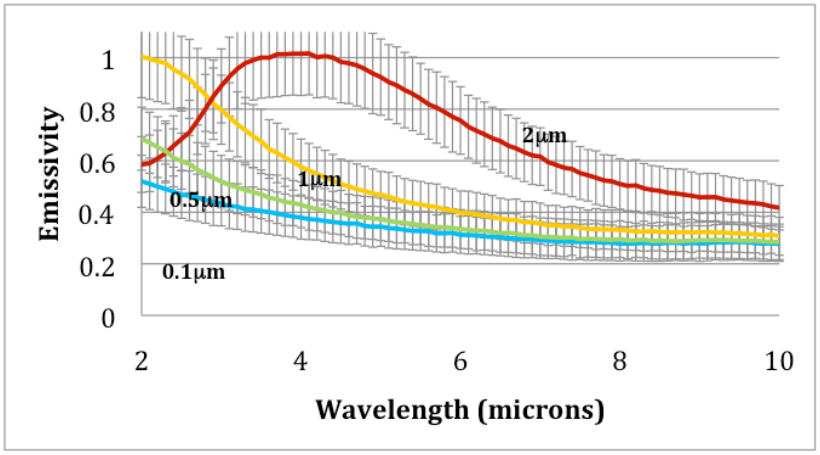

Figure 154. Numerical modeling of emissivity using Monte Carlo code and Maxwell's electromagnetic equations. The model assumes a thin inner hematite layer of a fixed thickness (0.1 μm) and outer magnetite layer of the thicknesses of 0.1, 0.5, 1, and 2 μm are 'numerically' grown on this hematite layer. The data above shows the spectral emissivities modeled for various magnetite layer thicknesses.

8. Programmatic Accomplishments

8.1. Publications/Presentations

- "System for High Temperature Spectral Emissivity Measurement of Materials for VHTR Applications "; S.R. Slattery, T.L. Malaney, S.J. Weber, M.H. Anderson, K. Sridharan, and T.R. Allen, *proc. ASME 4th International Topical Meeting on High Temperature Reactor Technology***,** Washington D.C, September 2008.
- "Emissivity of Candidate Materials for VHTR", K. Sridharan, *Research and Development FY-09 Technical review Meeting*, DoE VHTR Technology Development Office & Idaho National Laboratory (also monitored by an NRC team), Las Vegas, NV, May 2009 (invited).
- "Emissivity of Candidate Materials for VHTR Applications: Role of Oxidation and Surface Modification Treatments", K. Sridharan, *DoE Panel Review Presentation*, Salt Lake City, UT, August 2009.
- "Spectral Emissivity Measurements of Candidate Alloys for Very High Temperature Reactors in High Temperature Air Environments"; G. Cao, S.J. Weber, S.O. Martin, M.H. Anderson, K. Sridharan,and T.R. Allen, *Trans. American Nuclear Society Annual Conference, Nuclear Fuels and Structural Materials Meeting***,** San Diego, CA, June 2010.
- "Emissivity of Candidate Materials for VHTR Applications", M.H. Anderson, K. Sridharan, T.R. Allen, G. Cao, S.O. Martin, S.J. Weber, *INL/DoE sponsored Workshop on NGNP*, Denver, CO, April 2010 (invited).
- "Spectral Emissivity Measurements of Candidate Materials for Very High Temperature Reactors"**,** S.J. Weber, S.O. Martin, G. Cao, M.H. Anderson, K. Sridharan, and T.R. Allen, *proc. High Temperature Reactors Conference***,** Prague, Czech Republic, October 2010.
- "A Facility for *in situ* Measurements of High Temperature Spectral Emissivity of Materials for Very High Temperature Reactor Applications"; G. Cao, S. J. Weber, S. O. Martin, T. L. Malaney, S. R. Slattery, M. H. Anderson, K. Sridharan and T. R. Allen, *Nuclear Technology*, accepted (in press).
- "Spectral Emissivity Measurements of Candidate Materials for Very High Temperature Reactors", G. Cao, S.J. Weber, S.O. Martin, M.H. Anderson, K. Sridharan, and T.R. Allen, submitted to *Nuclear Engineering and Design*, 2011.
- Spectral Emissivity of Candidate Alloys for Very High Temperature Reactors in High Temperature Air Environment, G. Cao, S.J. Weber, S.O. Martin, K. Sridharan, M.H. Anderson, and T. R. Allen, submitted to *Journal of Nuclear Materials*, 2011.

We anticipate submitting <u>at least two more articles</u> on the findings of this project to relevant journals over the course of the next six months.

8.2. Involvement of Students and Post-Doctoral Associates

Masters Thesis

Ms. Tamara L. Malaney (presently employed at Exelon, MN): "Spectral Emissivity and Measurements and Modeling of High Temperature Reactor Materials", *M.S. Thesis*, Department of Nuclear Engineering and Engineering Physics, University of Wisconsin Madison, July 2009.

Mr. Scott J. Weber (presently employed at Sandia National Laboratories, NM): "Spectral Emissivity Studies for VHTR Candidate Materials", *M.S. Thesis*, Department of Nuclear Engineering and Engineering Physics, University of Wisconsin Madison, August 2010.

Undergraduate Students Actively Involved in the Project

Scott Weber (Nuclear Engineering major)

Tamara Malaney (Nuclear Engineering major)

Stuart Slattery (Nuclear Engineering major)

Sean Martin (Nuclear Engineering major)

David Adam (Nuclear Engineering major)

Michael Adashek (Materials Science and Engineering major)

Jessica Rybicki (Engineering Mechanics major)

High School Student

Nicholas Cupery (selected by Madison School District Science Program to work during Summer 2010).

Post-Doctoral Associates

Dr. Guoping Cao

9. REFERENCES CITED

[1] G. HAYNER, R. BRATTON, and R. MIZIA, Next Generation Nuclear Plant Materials Research and Development Program Plan, *Technical Report INL/EXT-06-11701*, INL, 2006.

[2] K. PERRY, Next Generation Nuclear Plant Project 2009 Status Report, Technical Report INL/EXT-09-17505 Revision 0, INL, 2009.

[3] G. HAYNER, NGNP Conceptual Design Study: Composites R&D Technical Issues, *Technical Report INL/EXT-09-16542*, Westinghouse Electric Company, LLC, 2008.

[4] G. ATOMICS, Engineering Services For The Next Generation Nuclear Plant (NGNP) With Hydrogen Production, NGNP Composites R&D Technical Issues Study, *Technical Report 911125*, General Atomics, 2008.

[5] AREVA, NGNP Composites R&D Technical Issues Study, *Technical Report TDR-3000807 Revision 1*, Areva, 2008.

[6] R. YOUNG, G. KERR, *Reassessment of the Atomic Bomb Radiation Dosimetry for Hiroshima and Nagasaki*, Ch. 8: Activation Measurements for Thermal Neutrons, pg. 456-470, Radiation Effects Research Foundation, 2005.

[7] H.J. CHRIST, U. KUNECKE, K. MEYER, and H.G. SOCKEL, High Temperature Corrosion of the Nickel-based Alloy Inconel 617 in Helium Containing Small Amounts of Impurities, *Material Science and Engineering*, 87 (161-168), 1987.

[8] H.M. YUN, P.J. ENNIS, H. NICKEL, and H. SCHUSTER, The Effect of High Temperature Reactor Primary Circuit Helium on the Formation and Propagation of Surface Cracks in Alloy 800 H and Inconel 617, *Journal of Nuclear Materials*, 125 (258-272), 1984.

[9] A.M. IGLESIAS and M.A. CALDERON, Thermal Resistance Contributions of Oxides Growth on Incoloy 800 Steam Generator Tubes, *Nuclear Engineering and Design*, 219 (1-10), 2003.

[10] W.H. CHRISTIE, R.E. EBY, Et. Al, SIMS Analysis of Oxide Films Grown on Incoloy 800 Heat Exchanger Material, *Applications of Surface Science*, 13 (414-428), 1982.

[11] K. SRIDHARAN, Emissivity of Candidate Materials for VHTR Applications: Role of Oxidation and Surface Modification Treatments*, Presentation at DOE Panel Review Meeting*, Salt Lake City, UT, 2009.

[12] M. MODEST, *Radiative Heat Transfer*, Elsevier Science, 2003.

[13] J.J.P. ELICH and J.A. WIERINGA, Temperature Effects Influencing the Spectral and Total Emissivity of Refractories, *Experimental Thermal and Fluid Science*, 10 (318-326), 1995.

[14] C. WEN, Investigation of Steel Emissivity Behaviors: Examination of Multispectral Radiation Thermometry (MRT) Emissivity Models, *International Journal of Heat and Mass Transfer*, 53 (2035-2043), 2009.

[15] Z. WAN, D. NG, and J. DOZIER, Spectral Emissivity Measurements of Land-Surface Materials and Related Radiative Transfer Simulations, *Adv. Space Res.*, Vol. 14, No.3 (91-94), 1994.

[16] M. KRISHNA, M. RAJENDRAN, D. PYKE, A. BHATTACHARYA, Spectral Emissivity of Ytterbium Oxide-Based Materials for Application as Selective Emitters in Thermophotovoltaic Devices, *Solar Energy Materials & Solar Cells*, 59 (337-348), 1999.

[17] L. DEL CAMPO, Et. Al, New Experimental Device for Infrared Spectral Directional Emissivity Measurements in a Controlled Environment, *Review of Scientific Instruments*, 77, 113111, 2006.

[18] W. SMETANA and R. REICHER, A New Measuring Method to Determine Spectral Emissivity, *Meas. Sci. Technol.*, 9 (797-802), 1998.

[19] G.A. GREENE, C.C. FINFROCK, T.F. IRVINE Jr., "Total Hemispherical Emissivity of Oxidized Inconel 718 in the Temperature Range 300-1000^{o}C", *Experimental Thermal and Fluid Science*, 22 (145-153), 2000.

[20] G. TANDA and M. MISALE, "Measurement of Total Hemispherical Emittance and Specific Heat of Aluminum and Inconel 718 by a Calorimetric Technique", *Transactions of the ASME*, 128 (302-306), 2006.

[21] G. NEUER, and F. GUNTERT, "In-situ Measurements of Layer Thickness During Oxidation of Titanium", *Thermochimica Acta,* 133 (299-304), 1988.

[22] T. MAKINO and H. WAKABAYASHI, "Thermal Radiation Spectroscopy Diagnosis for Temperature and Microstructure of Surfaces", *JSME International Journal*, 46 (500-509), 2003.

[23] A. OTSUKA, Et. Al, A Survey of Hemispherical Total Emissivity of the Refractory Metals in Practical Use, *Energy*, 30 (535-543), 2005.

[24] T. IUCHI, T. FURUKAWA, and S. WADA, "Emissivity Modeling of Metals During the Growth of Oxide Film and Comparison of the Model with Experimental Results", *Applied Optics*, 42 (2317-2326), 2003.

[25] B. ZHANG, J. REDGROVE, and J. CLARK, New Apparatus for Measurement of the Spectral, Angular, and Total Emissivity of Solids, *High Temperatures – High Pressures*, Vol. 35/36, pg. 289-302, 2004.

[26] C. HU, Et. Al, The Epoxy-Siloxane/Al Composite Coatings with Low Infrared Emissivity for High Temperature Applications, *Applied Surface Science*, 256 (3459-3463), 2009.

[27] J. DAI, X. WANG, and G. YUAN, Fourier Transform Spectrometer for Spectral Emissivity Measurement in the Temperature Range between 60 and 1500^{o}C, *Journal of Physics: Conference Series*, 13 (63-66), 2005.

[28] J.R. MARKHAM, K. KINSELLA, R.M. CARANGELO, Et. Al, Bench Top Fourier Transform Infrared Based Instrument for Simultaneously Measuring Surface Spectral Emittance and Temperature, *Rev. Sci. Instruments*, 64 (2515-2523), 1993.

[29] A. SIEVERS, Temperature Dependence of the Emissivity of Transition Metals, *Solar Energy Materials*, 1 (431-439), 1979.

[30] L. DEL CAMPO, Et. Al, Emissivity Measurements on Aeronautical Alloys, *Journal of Alloys and Compounds*, 489 (482-487), 2009.

[31] R. SIEGEL and J. HOWELL, *Thermal Radiation Heat Transfer*, 4th Edition, Taylor &Francis, 2002.

[32] G. TEODORESCU, P.D. JONES, R.A. OVERFELT, and B. GUO, Normal Emissivity of High-Purity Nickel at Temperatures Between 1440 and 1605 K, *Journal of Physics and Chemistry of Solids,* 69 (133-138), 2008.

[33] AMERICAN METEOROLOGICAL SOCIETY, Glossary of Meteorology, 2nd Edition, http://amsglossary.allenpress.com/glossary

[34] X. HE, Et. Al, High Emissivity Coatings for High Temperature Application: Progress and Prospect, *Thin Solid Films*, 517 (5120-5129), 2009.

[35] M. ROSENBERG, R.D. SMIRNOV, and A.Y. PIGAROV, On Thermal Radiation from Fusion Related Metals, *Fusion Engineering and Design,* 84 (38-42), 2009.

[36] L. DEL CAMPO, R. PEREZ-SAEZ, M. TELLO, Iron Oxidation Kinetics Study by using Infrared Spectral Emissivity Measurements below 570oC, *Corrosion Science*, 50 (194-199), 2008.

[37] C. WEN and I. MUDAWAR, Emissivity Characteristics of Polished Aluminum Alloy Surfaces and Assessment of Multispectral Radiation Thermometry (MRT) Emissivity Models, *International Journal of Heat and Mass Transfer*, 48 (1316-1329), 2005.

[38] K. IRANI, Theory and Construction of Blackbody Calibration Sources, *Thermosense XXIII Proceedings*, SPIE, pp. 347-363, 2001.

[39] M. G. Inc., http://www.mellesgriot.com/products/optics/images/fig4_7.gif, 2002.

[40] Y. TOULOUKIAN and D. DEWITT, *Thermophysical Properties of Matter,* Vol. 7 & 8, IFI/Plenum, 1970-1972.

[41] L. TAN, X. REN, K. SRIDHARAN, and T.R. ALLEN, Effect of Shot Peening on the Oxidation of Alloy 800H Exposed to Supercritical Water and Cyclic Oxidation, *Corrosion Science*, 50 (2040), 2008.

[42] I.A. EL-SHANSHOURY, A.V. CHIRKIN, and A. EL-YAZGI, On the Oxidation of Zirconium by Heat Tinting, *Journal of Nuclear Materials*, 149 (74-79), 1987.

[43] M. Born and E. Wolf, *Principles of Optics: Electromagnetic Theory of Propagation, Interference and Diffraction of Light*, Cambridge University Press, 1997.

[44] M. MODEST, *Radiative Heat Transfer*, McGraw-Hill, Inc., 1993.

[45] K. FU and P. HSU, *Journal of Heat Transfer*, 129 (2007).

[46] D. DEMANGE, M. BEJET, and B. DUFOUR, New Methods for Measuring the Thermal Emissivity of Semi-transparent and Opaque Materials, in Eurotherm, 2006.

[47] A. KRIBUS, I. VISHNEVETSKY, E. ROTENBERY, and D. YAKIR, *Applied Optics*, 42 (2003).

[48] T. IUCHI, T. FURUKAWA, and S. WADA, *Applied Optics*, 42 (2003).

[49] C. ISETTIand E. NANNEI, "Total normal emittance of stainless steel at high temperatures: influence of oxide layer growth" *High Temperatures–High Pressures*, 12 (1980).

[50] I. PETROVA et al, *International journal of Thermophysics*, 24 (2003).

[51] T. IUCHI, Temperature 7 (2003).

[52] R. G. DEIGGERS, *Encyclopedia of Optical Engineering*, CRC Press, 2003.